TITULO

The Northern Current and its interaction with the Blanes submarine canyon (NW Mediterranean Sea)

AUTOR

Miguel Angel Ahumada Sempoal

DIRECTOR

Dr. Antonio Cruzado Alorda

FECHA

22 de Octubre de 2014

UNIVERSITAT POLITÈCNICA DE CATALUNYA
BARCELONATECH
Escola de Doctorat

Curs acadèmic: 2014-2015

Acta de qualificació de tesi doctoral

Nom i cognoms
Miguel Angel Ahumada Sempoal

Programa de doctorat
Ciències del Mar

Unitat estructural responsable del programa
Departament d'Enginyeria Hidràulica, Marítima i Ambiental

Resolució del Tribunal

Reunit el Tribunal designat a l'efecte, el doctorand / la doctoranda exposa el tema de la seva tesi doctoral titulada

_____

_____.

Acabada la lectura i després de donar resposta a les qüestions formulades pels membres titulars del tribunal, aquest atorga la qualificació:

☐ NO APTE ☐ APROVAT ☐ NOTABLE ☐ EXCEL·LENT

(Nom, cognoms i signatura) President/a	(Nom, cognoms i signatura) Secretari/ària

(Nom, cognoms i signatura) Vocal	(Nom, cognoms i signatura) Vocal	(Nom, cognoms i signatura) Vocal

_____, _____ d'/de _____ de _____

El resultat de l'escrutini dels vots emesos pels membres titulars del tribunal, efectuat per l'Escola de Doctorat, a instància de la Comissió de Doctorat de la UPC, atorga la MENCIÓ CUM LAUDE:

☐ SÍ ☐ NO

(Nom, cognoms i signatura) President de la Comissió Permanent de l'Escola de Doctorat	(Nom, cognoms i signatura) Secretària de la Comissió Permanent de l'Escola de Doctorat

Barcelona, _____ d'/de _____ de _____

Universitat Politècnica de Catalunya

Consejo Superior de Investigaciones Científicas

Universitat de Barcelona

The Northern Current and its interaction with the Blanes submarine canyon (NW Mediterranean Sea)

Miguel Angel Ahumada Sempoal

A thesis submitted for the degree of
Doctor in Marine Sciences

Supervised by Dr. Antonio Cruzado Alorda

Barcelona, October 22, 2014

To Miranda, my daughter
To Gabriela, my wife
To my family

Contents

Acknowledgements

The author gratefully acknowledges the facilities and support from the Universidad del Mar, UMAR (México). The author was also supported by PROMEP-SEP (México) in the framework of a PhD. grant. The author also acknowledges the facilities from the Centre d'Estudis Avançats de Blanes, CEAB-CSIC (Spain) and from the research project OAMMS (CTM2008-03983) funded by the Spanish Ministry of Science and Innovation (Spain).

I would like to express my deepest gratitude to my thesis advisor Dr. Antonio Cruzado Alorda. This work would not have been possible without his guidance and patience.

I would like to extend my thanks to the external reviewers, Dr. Gabriel Jordà Sánchez and Dr. Andres Sepulveda Allende.

I would also like to extend my deepest gratitude to Mar Flexas, Raffaele Bernardello, Nixon Bahamon, Cristobal Reyes and Héctor García Nava... Your help has been absolutely invaluable to me during this long... long journey. Thanks a lot!

I would like to thanks to the ROMS_AGRIF/ROMSTOOLS's team: G. Cambon, L. Debreu, P. Marchesiello and P. Penven, ROMS_AGRIF/ROMSTOOLS Forum and ROMS Forum. I would also like to thanks to A. Jordi, M. Dinniman and T. Connolly, as well as the ARAINE's team: B. Blanke and N. Grima.

Finally, I would like to express my sincere gratitude to Zoila Velasquez.

Happy modeling!
ROMS Forum

Abstract

A high-resolution (~1.2km) 3D circulation model nested in one-way to a coarse-resolution (~4km) 3D regional model was used to examine the interaction between the Northern Current and the Blanes submarine canyon (~41°00'-41°46'N; ~02°24'-03°24'E); paying particular attention to upwelling/downwelling events and cross-shelf break water exchange. A Lagrangian particle-tracking algorithm coupled to the high-resolution 3D circulation model was also used to examine the role of the Northern Current (NC) and its seasonal variability on the dispersion of passive particles and residence time within Blanes Canyon (BC). Although it refers to a climatological simulation (i.e. no interannual variability), at this resolution, the Rossby radius of deformation for the Mediterranean Sea (5-12 km) is resolved. Therefore the numerical modeling system properly suites our purpose, since it adequately reproduces the NC mesoscale variability and its seasonality. Satisfactory validation of model results with remote sensing and in-situ observations supports the present findings.

The simulated NC tends to be fast and deep in winter, and slow and shallow in summer. NC meanders and eddies are recurrent in the BC area and produce highly fluctuating three-dimensional circulation patterns within the canyon. NC meanders and anticyclonic eddies propagating along the current pathway tend to be deep and, consequently, their effects extend down to the deeper part of BC. The meandering of the NC plays a key role in enhancing vertical motions within the canyon. NC meanders produce an oscillation of the vertical flow characterized by net upwelling when the meander is located over the upstream side of the canyon followed by net downwelling as the meander moves downstream. Associated with NC meanders passing over BC, upwelling and downwelling events occur on timescales of 4 to 20 days and they are more frequent in winter. These findings provide further evidence that continuous downwelling favourable (right-bounded) flows can produce net upwelling inside submarine canyons.

Concerning cross-shelf break water exchange, one significant finding from this study is that the amount of water moved across the shelf break at the upstream upper canyon wall is approximately two times larger than the amount of water moved downstream. This preferential zone for cross-shelf break exchange is related to the asymmetry of the shelf break geometry that is characterized by a sharp curvature upstream. Results also show that cross-shelf break water exchange is higher (~30%) in winter than in summer. On the other hand, particle-tracking experiments show that passive particles released from the mid-shelf to the upper-slope drift

along the shelf edge with a net downward movement within the upper canyon. They also show that particle dispersion is higher in winter than in summer and that particles travelling below the canyon rim (i.e. below 100 m depth) have longer residence times within the canyon.

Resumen

Un modelo de circulación 3D con resolución de ~1.2km anidado en una vía a un modelo regional 3D con resolución de ~4km, fue empleado para estudiar la interacción entre la Corriente del Norte y el cañón submarino Blanes (~41°00'-41°46'N; ~02°24'-03°24'E). Se hace especial énfasis en los eventos de elevación y hundimiento de agua, así como en el intercambio de agua a través del borde de la plataforma continental. También se uso un algoritmo Lagrangiano alimentado con los campos de velocidad del modelo de alta resolución para estudiar el papel de la Corriente del Norte (NC, por sus siglas en inglés) y su estacionalidad en la dispersión de partículas pasivas y tiempos de residencia dentro del Cañón Blanes (BC, por sus siglas en inglés). Aunque se trata de una simulación climatológica (i.e. sin variabilidad interanual), el radio de deformación de Rossby para el Mar Mediterráneo (5-12km) es resuelto. Por lo tanto, el sistema de modelado es de una resolución apropiada para nuestros objetivos ya que reproduce adecuadamente la NC y su estacionalidad. Los resultados comparan satisfactoriamente con información de imágenes de satélite y observaciones in-situ.

Los resultados indican que la NC tiende a ser rápida y profunda en invierno, y lenta y somera en verano. El paso de meandros en la NC y remolinos es un rasgo frecuente en el cañón Blanes. En particular, meandros y remolinos anticiclónicos que se propagan siguiendo la trayectoria de la NC tienden a ser profundos y, consecuentemente, sus efectos se extienden hacia la parte profunda del cañón. Nuestros resultados también indican que los meandros en la NC juegan un papel importante en el aumento del movimiento vertical dentro del cañón. Estos meandros producen una oscilación del flujo vertical caracterizado por una elevación neta de agua conforme el meandro pasa sobre el lado Este del cañón seguido por un hundimiento neto conforme el meandro se mueve hacia el lado Oeste. Eventos de elevación y hundimiento de agua en escalas temporales de 4 a 20 días están asociados al paso de meandros, siendo estos eventos más frecuentes en invierno. Estos resultados aportan más evidencia de que flujos continuos con la costa a la derecha (i.e. favorables para el hundimiento de agua) pueden producir elevación neta de agua dentro de cañones submarinos.

Con relación al intercambio de agua a través del borde de la plataforma continental, un resultado importante del presente estudio es que la cantidad de agua que pasa a través del borde de la pared Este del cañón es aproximadamente el doble de la cantidad de agua que pasa a través del borde de la pared Oeste. Esta zona preferencial para el intercambio de agua está relacionada con la curvatura del borde de la plataforma continental, la cual es más pronunciada sobre la pared Este

del cañón. Los resultados también indican que el intercambio de agua es mayor (~30%) en invierno que en verano. Por otro lado, partículas pasivas liberadas sobre la plataforma y la pendiente continental derivan a lo largo del borde de la plataforma con un movimiento neto hacia abajo dentro del cañón. Los resultados también muestran que la dispersión de partículas es mayor en invierno que en verano. Finalmente, los resultados indican que el tiempo de residencia tiende a incrementarse con la profundidad, así las partículas que se mueven por debajo de la profundidad del anillo del cañón (i.e. por debajo de 100 m de profundidad) presentan un tiempo de residencia mayor dentro del cañón.

List of Figures

List of Tables

Chapter 1

Introduction

1.1. Motivation and objectives

Submarine canyons are hotspots of productivity and biodiversity. Up-canyon flows induce nutrient-rich deep-water transport onto the continental shelf contributing to enhanced local biological productivity (e.g. Freeland and Denman, 1982; Skliris and Djenidi, 2006; Kämpf, 2010; Connolly and Hickey, 2014). Down-canyon flows, on the other hand, enhance particle fluxes and upper-slope waters export from the adjacent shelf to the deep basin contributing to the generation of special habitat conditions suitable for the recruitment and maintenance of corals, sponges, demersal fishes, crustaceans and other deep-sea organisms (e.g. Gili et al., 2000; Sardà et al., 2009; De Leo et al., 2010).

The NW Mediterranean Sea is a region where numerous submarine canyons cut the continental margin (between three and four canyons per 100 km along the shelf break; Allen and Durrieu de Madron, 2009). The regional flow is dominated by the Northern Current (NC) which originates in the Ligurian Sea where the Eastern Corsican Current merges with the Western Corsican Current (Fig. 1.1). From the Ligurian Sea the NC flows along the continental shelf as far as the southern Catalan Sea where it splits into two branches: while the first one flows southward crossing the Ibiza Channel, the second one re-circulates north-eastward contributing to the formation of the Balearic Current on the northern side of the Balearic Islands. The NC is an energetic along-slope flow in quasi-geostrophic balance with a shelf/slope density front maintained by the salinity contrast between relatively fresh coastal waters and more saline waters offshore (e.g. Font et al., 1988; Cruzado and Velasquez, 1990; Astraldi et al., 1994; García-Ladona et al., 1996). The NC is a right-bounded flow (i.e. with the coastline on the right, looking downstream) of about 30-50 km wide; its velocity is maximum near the surface (20-30 cm/s) and decreases, nearly linearly with depth, to speeds of a few centimetres per second at 300-400 m depth (Flexas et al., 2002). From mid-autumn to early spring, the NC is narrow, fast and deep (cf. Millot, 1999); displaying mesoscale structures such as meanders and eddies that develop and propagate along the current pathway modifying the local circulation (e.g. Sammari et al., 1995; Flexas et al., 2002; Rubio et al., 2005; Casella et al., 2011).

The interaction of the NC with submarine canyons is relevant because it can cause significant vertical motions. Net upwelling/downwelling in submarine canyons has usually been associated with left/right-bounded flows, however, most studies on the flow over submarine canyons focus on wind-forced flows (see Allen and Durrieu de Madron (2009) and references therein). Although the NC is an example of continuous along-slope density-driven right-bounded flow

(i.e. a downwelling favourable flow), studies based on laboratory experiments and field observations have shown evidence of right-bounded flows causing upwelling near the shelf break of submarine canyons (Boyer et al., 2006; Flexas et al., 2008). The interaction of the NC with submarine canyons is also relevant because it can induce significant water exchange across the shelf break (Jordi et al., 2005). Observations reveal clear differences in the amount of settling particles in canyon and slope environments, for example, particle fluxes within Blanes Canyon are higher (almost one order of magnitude) than the fluxes recorded in the neighbouring open slope at the same depths (Zuñiga et al., 2009; Sanchez-Vidal et al., 2012; Lopez-Fernandez et al., 2013). Although water exchange across the shelf break and particle fluxes are essential to biogeochemical and ecological processes taking place in the continental shelf and the deep sea (Fennel, 2010; Johnson and Chapman, 2011; Canals et al., 2013), they are not easy to quantify from observations alone. Direct measurements in submarine canyons are generally difficult and expensive. Maintenance of instrumentation and fishing activities prevent from keeping safe moored arrays for long periods of time; therefore, numerical modeling is a powerful tool that provides confident oceanographic information at relatively high resolutions for both scientific and operational purposes.

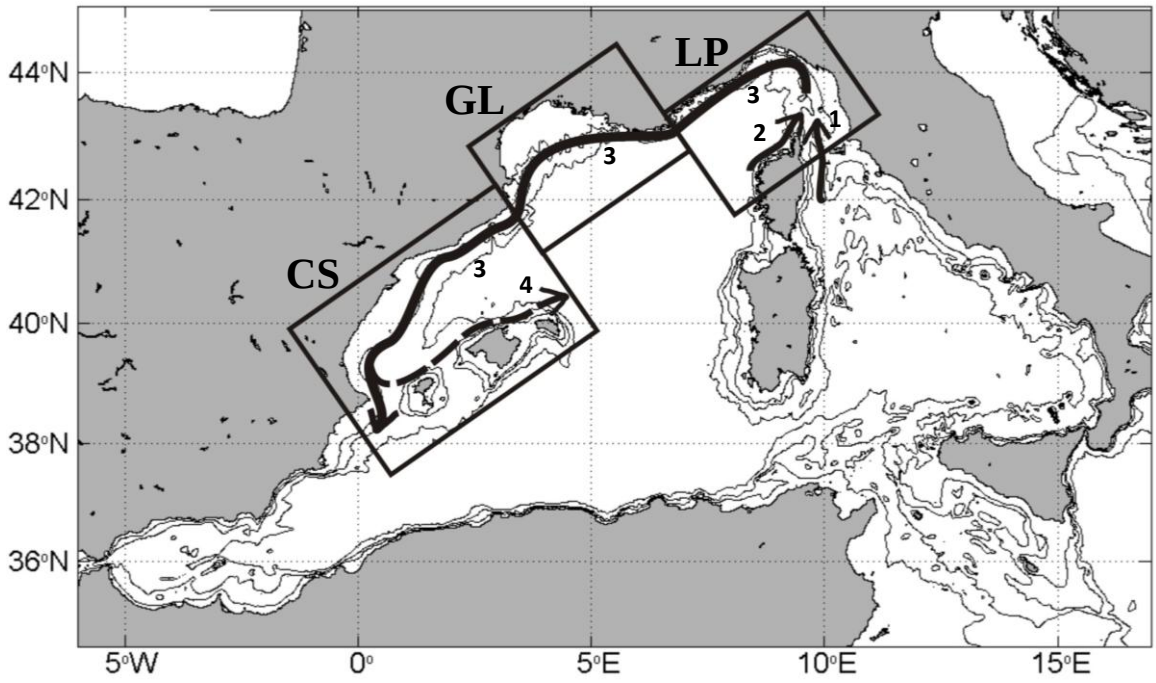

Figure 1.1 The NW Mediterranean Sea subbasins and major currents. *Acronyms stand for*: LP = Liguro-Provençal subbasin, GL = Gulf of Lions and CS = Catalan Sea. 1: Eastern Corsican Current, 2: Western Corsican Current, 3: Northern Current, and 4: Balearic Current. Contours correspond to the 150, 500 and 1500 m isobaths. The bottom topography is based on ETOPO2 (Smith and Sandwell, 1997).

The aim of this thesis is to examine the Northern Current-Blanes Canyon interactions; paying particular attention to upwelling/downwelling events and cross-shelf break water exchange. To this purpose, we used a high-resolution (~1.2km) 3D circulation model nested in one-way mode to a coarse resolution (~4km) 3D regional model. Although it refers to a climatological simulation (i.e. no interannual variability), at this resolution, the Rossby radius of deformation for the Mediterranean Sea (5-12 km; Grilli and Pinardi, 1998) is resolved. Therefore the model properly suites our purpose, since it adequately reproduces the Northern Current mesoscale variability and its seasonality. A Lagrangian particle-tracking model coupled to the high-resolution 3D circulation model is also used to examine the role of the Northern Current and its seasonality on the dispersion of passive particles and residence time within the Blanes Canyon.

1.2. Strategy

We will take advantage of the available computing power as well as of the accurate and efficient numerical algorithms that permit hydrodynamic models efficiently and robustly to simulate the dynamics of ocean circulation at different spatial and temporal scales. As the spatial resolution of a numerical model plays an important role in representing and simulating ocean dynamics, it is useful to concentrate the efforts in the domain of interest. In this context, we will take advantage of the benefits offered by the one-way nesting technique (e.g. Pullen, 2000; Mason et al., 2010) for the implementation of a high-resolution (~1.2km) 3D circulation model nested into a coarse-resolution (~4km) 3D regional model. This numerical modelling system at variable resolution allows us to resolve the shelf/slope dynamics taking into account the influence of the large-scale circulation.

1.3. Overview of the thesis

This thesis is organized into six chapters and one appendix. Chapter 2 describes the numerical modelling system. Chapter 3 presents and validates the NW Mediterranean Sea hydrography and general circulation as simulated by the regional model. Chapter 4 presents, validates, and discusses the high-resolution (~1.2km) 3D circulation model results with emphasis on the variability of the Northern Current and its influence on the Blanes Canyon circulation; paying particular attention to upwelling/downwelling events and their seasonal variability. Chapter 5

analyses the cross-shelf break water exchange in the Blanes Canyon, as well as dispersion of passive particles and residence time. Chapter 6 presents conclusions and recommendations for future research. Finally, Appendix contains the bulk formulas used to specify the sea surface forcing.

Chapter 2

The numerical modeling system

2.1. Introduction

In this thesis, the numerical modeling system is based on ROMS_AGRIF/ROMSTOOLS v3.0. It is a version of the Regional Ocean Modeling System (ROMS) along with a pre- and post-processing toolbox developed at IRD and INRIA (Penven et al., 2006; Penven et al., 2008; Debreu et al., 2012). The purpose of this chapter is to give an outline of the background information regarding the main characteristics of ROMS, and for that reason, the following sections are based on information from the official web sites of ROMS_AGRIF (www.romsagrif.org) and ROMS-Rutgers (www.myroms.org), as well as from user's manuals and other basic references.

2.2. Model description

2.2.1. Governing Equations

ROMS is a split-explicit, free-surface, primitive-equations model, which is discretized in terrain-following vertical and orthogonal curvilinear horizontal coordinates using high-order numerical algorithms (e.g. Shchepetkin and McWilliams, 1998, 2003, 2005). ROMS solves equations for momentum, potential temperature, and salinity, as well as a nonlinear equation of state for seawater density. The sea surface elevation, velocity, potential temperature, and salinity are prognosticated by assuming that (i) seawater is incompressible, (ii) seawater density can be expressed in terms of a mean value and a small fluctuation (Boussinesq's approximation), and (iii) the pressure in anywhere point of the ocean is equal to the weight of the column of water over it (hydrostatic approximation). Consequently, in a system of orthogonal Cartesian coordinates, where *x* is positive eastwards, *y* is positive northwards, and *z* is positive upwards; if $\vec{v}$ is the velocity vector with components (*u*, *v*, *w*) and ∇ the gradient operator equal to $\frac{\partial}{\partial x}+\frac{\partial}{\partial y}+\frac{\partial}{\partial z}$, the governing equations may be written as:

Continuity Equation

$$\nabla\cdot\vec{v}=0 \qquad (2.1)$$

The continuity equation states that in the absence of sources or sinks of matter, density local changes are exclusively determined by divergences and convergences in the flux of mass. In other words, considering an infinitesimal volume element fixed in the space, the change of mass inside this volume will be equal to the mass inflow minus the mass outflow. If the density of a fluid element remains constant, the continuity equation requires that through any closed surface the inward flux be equal to the outward flux (Apel, 1987). That equation (Eq. 2.1) expresses the conservation of mass for an incompressible fluid.

Momentum Equations

$$\frac{\partial u}{\partial t} + \vec{v}\cdot\nabla u = fv - \frac{\partial \phi}{\partial x} - \frac{\partial}{\partial z}\left(\overline{u'w'} - \upsilon\frac{\partial u}{\partial z}\right) + F_x + D_x \qquad (2.2a)$$

$$\frac{\partial v}{\partial t} + \vec{v}\cdot\nabla v = -fu - \frac{\partial \phi}{\partial y} - \frac{\partial}{\partial z}\left(\overline{v'w'} - \upsilon\frac{\partial v}{\partial z}\right) + F_y + D_y \qquad (2.2b)$$

$$\frac{\partial \phi}{\partial z} = -\frac{\rho g}{\rho_0} \qquad (2.2c)$$

The momentum balances in the *x*- and *y*-directions are governed by Equations (2.2a) and (2.2b). Noted that in the Boussinesq's approximation, density changes are neglected in these equations, but their contribution to the buoyancy force is present in Eq. (2.2c). Under the hydrostatic approximation, it is further assumed that the vertical pressure gradient ($\partial\phi/\partial z$) balances the buoyancy force ($-g\rho/\rho_0$). Here $\phi = P/\rho_0$ is the dynamic pressure (where $P = -\rho_0 gz$ is the total pressure, ρ_0 is a reference density taken, in this study, as 1025 kg/m^3 and g is the gravitational acceleration); $\rho + \rho_0$ is the *in-situ* seawater density; υ is the molecular viscosity; and F_x, F_y, D_x and D_y represent the forcing and horizontal dissipation terms, respectively. A latitudinal variation of the Coriolis parameter f is introduced by use of the β-plane approximation (i.e. f varies with the sine of latitude, namely $f = 2\Omega\sin\varphi$, where $\Omega = 7.292 \times 10^{-5}$ rad s^{-1} and φ is the latitude). An overbar represents a time average and a prime represents a fluctuation about the mean. Equations (2.2a) and (2.2b) are closed by parameterizing the Reynolds stresses as $\overline{u'w'} = -K_M \frac{\partial u}{\partial z}$ and $\overline{v'w'} = -K_M \frac{\partial v}{\partial z}$, where K_M is the vertical eddy viscosity for turbulent mixing of momentum (further details in subsection 2.3.6).

Equation for potential temperature

$$\frac{\partial T}{\partial t} + \vec{v}\cdot\nabla T = -\frac{\partial}{\partial z}\left(\overline{T'w'} - \upsilon_T \frac{\partial T}{\partial z}\right) + F_T + D_T \tag{2.3}$$

Equation for salinity

$$\frac{\partial S}{\partial t} + \vec{v}\cdot\nabla S = -\frac{\partial}{\partial z}\left(\overline{S'w'} - \upsilon_S \frac{\partial S}{\partial z}\right) + F_S + D_S \tag{2.4}$$

Equation of state for seawater density

$$\rho = \rho(T, S, P) \tag{2.5}$$

The time evolution of potential temperature and salinity are governed by Equations (2.3) and (2.4), whereas Eq. (2.5) corresponds to the UNESCO equation of state for seawater density as derived by Jackett and McDougall (1995). υ_T and υ_S are the molecular diffusivities for temperature and salt; and F_T, F_S, D_T and D_S represent the forcing and horizontal dissipation terms, respectively. Equations (2.3) and (2.4) are closed by parameterizing the turbulent tracer fluxes as $\overline{T'w'} = -K_T \frac{\partial T}{\partial z}$ and $\overline{S'w'} = -K_S \frac{\partial S}{\partial z}$, where K_T and K_S are the vertical eddy diffusivity for turbulent mixing of heat and salt, respectively (further details in subsection 2.3.6).

The vertical boundary conditions for this set of governing equations are defined as:

At the surface ($z = \zeta$):

$$K_M \frac{\partial(u,v)}{\partial z} = (\tau_s^x, \tau_s^y) \tag{2.6}$$

$$K_T \frac{\partial T}{\partial z} = \frac{Q_T}{\rho_0 C_p} \tag{2.7}$$

$$K_S \frac{\partial S}{\partial z} = \frac{(E-P)S}{\rho_0} \tag{2.8}$$

$$w = \frac{\partial \zeta}{\partial t} \tag{2.9}$$

At the bottom ($z = -h$):

$$K_M \frac{\partial(u,v)}{\partial z} = (\tau_b^x, \tau_b^y) \tag{2.10}$$

$$K_{(T,S)} \frac{\partial(T,S)}{\partial z} = (0,0) \tag{2.11}$$

$$-w + \bar{v} \cdot \nabla h = 0 \tag{2.12}$$

where ζ is the sea surface elevation; τ_s^x, τ_s^y are the wind stress components; Q_T is the surface heat flux; C_p is the heat capacity of the seawater; *E-P* is the evaporation minus precipitation; *h* is the depth of the sea floor below the mean sea level; and τ_b^x, τ_b^y are the bottom stress components. In our configuration, bottom boundary conditions for momentum (*u*, *v*) are computed by assuming a logarithmic velocity profile and using the following formulation:

$$(\tau_b^x, \tau_b^y) = \rho_0 C_{db} \sqrt{u_b^{\,2} + v_b^{\,2}} (u_b, v_b) \tag{2.13}$$

with a coefficient drag (C_{db}) based on a bottom roughness length (Z_{ob}):

$$C_{db} = \left[\kappa \Big/ \ln\left(\frac{z}{Z_{ob}} \right) \right]^2 \tag{2.14}$$

where κ is the von Karman constant (= 0.4) and *z* is the distance from the bottom. We chosen Z_{ob}=1 x10^{-2} m, C_{db}_min=1 x10^{-4} and C_{db}_max=1 x10^{-1}.

2.2.2. The free-surface and vertically integrated momentum equations

ROMS uses a split-explicit time-stepping scheme to resolve the governing equations (Shchepetkin and McWilliams, 2005), so the numerical solution is divided in two parts: the barotropic (or external) mode and the baroclinic (or internal) mode (further details in subsection 2.3.3). This technique permits the calculation of the sea surface elevation with little sacrifice in computational time by solving the vertically integrated momentum equations (external mode) separately from the three-dimensional calculation of the momentum and thermodynamic equations (internal mode). If the total depth of the water column and the depth average of *u* and *v* are given by

$$D \equiv \zeta(x,y,t) + h(x,y)$$

$$\bar{u} \equiv \left(\frac{1}{D}\right)\int_{z=-h}^{\zeta} u dz$$

$$\bar{v} \equiv \left(\frac{1}{D}\right)\int_{z=-h}^{\zeta} v dz$$

then, by integrating Eq. (2.1) and using the vertical boundary condition at the sea surface (Eq. 2.9), an equation for the free-surface may be written as:

$$\frac{\partial \zeta}{\partial t} + \frac{\partial \bar{u} D}{\partial x} + \frac{\partial \bar{v} D}{\partial y} = 0 \tag{2.15}$$

while the momentum equations (2.2a) and (2.2b) become:

$$\frac{\partial \bar{u} D}{\partial t} + \frac{\partial \bar{u}^2 D}{\partial x} + \frac{\partial \bar{u}\bar{v} D}{\partial y} = gD\frac{\partial \zeta}{\partial x} + f\bar{v}D + \frac{\partial\left(K_M \frac{\partial \bar{u} D}{\partial z}\right)}{\partial z} + D\bar{F}_x \tag{2.16a}$$

$$\frac{\partial \bar{v} D}{\partial t} + \frac{\partial \bar{u}\bar{v} D}{\partial x} + \frac{\partial \bar{v}^2 D}{\partial y} = gD\frac{\partial \zeta}{\partial y} - f\bar{u}D + \frac{\partial\left(K_M \frac{\partial \bar{v} D}{\partial z}\right)}{\partial z} + D\bar{F}_y \tag{2.16b}$$

Here $\bar{F}_x$ and $\bar{F}_y$ represent the forcing terms.

2.2.3. Governing Equations in terrain-following vertical coordinate

Terrain (or topography)-following coordinates (or σ-coordinates) in numerical models simplify aspects of the computations by mapping the varying bottom topography into a regular domain (Song, 1998). In ROMS, as an extension to standard (linear) σ-coordinates (Phillips, 1957), a nonlinear stretching of the vertical coordinate (the so-called generalized σ- or *s*-stretched coordinates) can be applied that depends on local water depth (Song and Haidvogel, 1994). This option can be used to generate a more uniform vertical resolution near the sea surface and the bottom, and consequently, a better representation of the boundary layers. The vertical coordinate transformation used in this thesis is (see other options at https://www.myroms.org/wiki/index.php/Vertical_S-coordinate):

$$s(x, y, \sigma) = h_c\sigma + [h(x, y) - h_c]C(\sigma), \tag{2.17}$$

where $s(x, y, \sigma)$ is a nonlinear vertical transformation functional, h_c is a positive thickness controlling the stretching (it is a constant chosen to be the minimum depth of the surface boundary layer and/or the bottom boundary layer in which a higher resolution is required), σ is a fractional vertical stretching coordinate ranging from $-1 \le \sigma \le 0$, $h(x, y)$ is the unperturbed water column thickness, and $C(\sigma)$ is a non-dimensional, monotonic, vertical stretching function ranging from $-1 \le C(\sigma) \le 0$ and given by

$$C(\sigma) = (1-\theta_b)\frac{\sinh(\theta_s \sigma)}{\sinh(\theta_s)} + \theta_b \left[\frac{\tanh\left[\theta_s\left(\sigma + \frac{1}{2}\right)\right]}{2\tanh(\frac{1}{2}\theta_s)} - \frac{1}{2} \right], \tag{2.18}$$

where θ_s and θ_b are the surface and bottom control parameters. Their ranges are ($0<\theta_s \le 20$) and ($0<\theta_b \le 1$), respectively. This function has the following features: (1) it is infinitely differentiable in σ; (2) the larger values of (θ_s), the more resolution is kept above (h_c); (3) for ($\theta_b = 0$), the resolution all goes to the surface as θ_s is increased; and (4) for ($\theta_b = 1$), the resolution goes to both the surface and the bottom equally as (θ_s) is increased. The coordinate transformation is as follows:

$\hat{t} = t$
$\hat{x} = x$
$\hat{y} = y$
$\sigma = \sigma(x, y, z)$
$z = z(x, y, \sigma)$
$s = s(x, y, \sigma)$

$$\left(\frac{\partial}{\partial x}\right)_z = \left(\frac{\partial}{\partial x}\right)_s - \left(\frac{1}{H_z}\right)\left(\frac{\partial z}{\partial x}\right)_s \frac{\partial}{\partial s}$$

$$\left(\frac{\partial}{\partial y}\right)_z = \left(\frac{\partial}{\partial y}\right)_s - \left(\frac{1}{H_z}\right)\left(\frac{\partial z}{\partial y}\right)_s \frac{\partial}{\partial s}$$

$$\frac{\partial}{\partial z} = \left(\frac{\partial s}{\partial z}\right)\frac{\partial}{\partial s} = \frac{1}{H_z}\frac{\partial}{\partial s}$$

$$H_z \equiv \frac{\partial z}{\partial s}$$

After conversion to *s*-stretched coordinate, and deletion of the carats, the governing equations may be written as:

Continuity equation

$$\frac{\partial \zeta}{\partial t} + \frac{\partial (H_z u)}{\partial x} + \frac{\partial (H_z v)}{\partial y} + \frac{\partial (H_z \Omega)}{\partial s} = 0 \tag{2.19}$$

Momentum equations

$$\frac{\partial u}{\partial t} + \vec{v} \cdot \nabla u = fv - \frac{\partial \phi}{\partial x} - \left(\frac{g\rho}{\rho_0} \right) \frac{\partial z}{\partial x} - g \frac{\partial \zeta}{\partial x} + \frac{1}{H_z} \frac{\partial}{\partial s} \left[\frac{(K_M + \upsilon)}{H_z} \frac{\partial u}{\partial s} \right] + F_u + D_u \tag{2.20a}$$

$$\frac{\partial v}{\partial t} + \vec{v} \cdot \nabla v = -fu - \frac{\partial \phi}{\partial y} - \left(\frac{g\rho}{\rho_0} \right) \frac{\partial z}{\partial y} - g \frac{\partial \zeta}{\partial y} + \frac{1}{H_z} \frac{\partial}{\partial s} \left[\frac{(K_M + \upsilon)}{H_z} \frac{\partial v}{\partial s} \right] + F_v + D_v \tag{2.20b}$$

$$\frac{\partial \phi}{\partial s} = -\frac{\rho g H_z}{\rho_0} \tag{2.20c}$$

Equation for potential temperature

$$\frac{\partial T}{\partial t} + \vec{v} \cdot \nabla T = \frac{1}{H_z} \frac{\partial}{\partial s} \left[\frac{(K_T + \upsilon_T)}{H_z} \frac{\partial T}{\partial s} \right] + F_T + D_T \tag{2.21}$$

Equation for salinity

$$\frac{\partial S}{\partial t} + \vec{v} \cdot \nabla S = \frac{1}{H_z} \frac{\partial}{\partial s} \left[\frac{(K_S + \upsilon_S)}{H_z} \frac{\partial S}{\partial s} \right] + F_S + D_S \tag{2.22}$$

Equation of state for seawater density

$$\rho = \rho(T, S, P) \tag{2.23}$$

where $\vec{v} = (u, v, \Omega)$ and $\vec{v} \cdot \nabla = u \frac{\partial}{\partial x} + v \frac{\partial}{\partial y} + \Omega \frac{\partial}{\partial s}$

In this coordinate system, the vertical velocity is defined as:

$$\Omega(x,y,s,t) = \frac{1}{H_z}\left[w - (1-s)\frac{\partial \zeta}{\partial t} - u\frac{\partial z}{\partial x} - v\frac{\partial z}{\partial y} \right] \tag{2.24}$$

where $w = \frac{\partial z}{\partial t} + u\frac{\partial z}{\partial x} + v\frac{\partial z}{\partial y} + \Omega H_z$.

The vertical boundary conditions become:

At the surface (s = 0):

$$\frac{K_M}{H_z}\frac{\partial (u,v)}{\partial s} = (\tau_s^x, \tau_s^y) \tag{2.25}$$

$$\frac{K_T}{H_z}\frac{\partial T}{\partial s} = \frac{Q_T}{\rho_0 C_p} \tag{2.26}$$

$$\frac{K_S}{H_z}\frac{\partial S}{\partial s} = \frac{(E-P)S}{\rho_0} \tag{2.27}$$

$$\Omega = 0 \tag{2.28}$$

At the bottom (s = -1):

$$\frac{K_M}{H_z}\frac{\partial (u,v)}{\partial s} = (\tau_b^x, \tau_b^y) \tag{2.29}$$

$$\frac{K_{(T,S)}}{H_z}\frac{\partial (T,S)}{\partial s} = 0 \tag{2.30}$$

$$\Omega = 0 \tag{2.31}$$

2.2.4. Governing Equations in curvilinear horizontal coordinates

This system can conform to irregular lateral boundaries or allows the placing of more computational resolution in areas of interest such as regions of enhanced structure (e.g. fronts, shelf-slope or boundary currents) or complex bottom topography (e.g. shelfbreak areas, seamounts or submarine canyons) which occupy a relatively small fraction of the model domain

(Ly and Jiang, 1999; Casella, 2009). According to Haidvogel et al. (2000) and Hedström (2009), the horizontal curvilinear coordinates are defined by

$$(ds)_{\xi} = \left(\frac{1}{m}\right) d\xi \tag{2.32a}$$

$$(ds)_{\eta} = \left(\frac{1}{n}\right) d\eta \tag{2.32b}$$

where $m(\xi, \eta)$ and $n(\xi, \eta)$ are the scale factors which relate the differential distance ($\Delta\xi$, $\Delta\eta$) to the physical arc length ΔS (see Fig. 2.1). Note that this general formulation of curvilinear coordinates includes Cartesian coordinates (by setting m = n = constant) as well as spherical coordinates with $m \sim \frac{1}{R\cos\varphi}$ and $n \sim \frac{1}{R}$, where φ is the geographical latitude and R is the mean radius of the Earth (~6371 km).

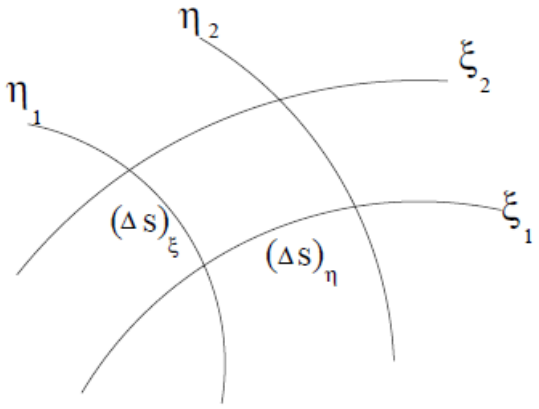

Figure 2.1 Horizontal curvilinear coordinates (After Hedström, 2009).

Under this horizontal transformation the INTERNAL (or baroclinic) MODE equations are written as:

Continuity equation

$$\frac{\partial}{\partial t}\left(\frac{\zeta}{mn}\right) + \frac{\partial}{\partial \xi}\left(\frac{H_z u}{n}\right) + \frac{\partial}{\partial \eta}\left(\frac{H_z v}{m}\right) + \frac{\partial}{\partial s}\left(\frac{H_z \Omega}{mn}\right) = 0 \tag{2.33}$$

Momentum equations

$$\begin{aligned}&\frac{\partial}{\partial t}\left(\frac{H_z u}{mn}\right)+\frac{\partial}{\partial \xi}\left(\frac{H_z u^2}{n}\right)+\frac{\partial}{\partial \eta}\left(\frac{H_z uv}{m}\right)+\frac{\partial}{\partial s}\left(\frac{H_z u\Omega}{mn}\right)=\\&\left\{\left(\frac{f}{mn}\right)+v\frac{\partial}{\partial \xi}\left(\frac{1}{n}\right)-u\frac{\partial}{\partial \eta}\left(\frac{1}{m}\right)\right\}H_z v\\&-\left(\frac{H_z}{n}\right)\left(\frac{\partial \phi}{\partial \xi}+\frac{g\rho}{\rho_0}\frac{\partial z}{\partial \xi}+g\frac{\partial \zeta}{\partial \xi}\right)+\\&\frac{1}{mn}\frac{\partial}{\partial s}\left[\frac{(K_M+\upsilon)}{H_z}\frac{\partial u}{\partial s}\right]+\frac{H_z}{mn}(F_u+D_u)\end{aligned} \tag{2.34a}$$

$$\begin{aligned}&\frac{\partial}{\partial t}\left(\frac{H_z v}{mn}\right)+\frac{\partial}{\partial \xi}\left(\frac{H_z uv}{n}\right)+\frac{\partial}{\partial \eta}\left(\frac{H_z v^2}{m}\right)+\frac{\partial}{\partial s}\left(\frac{H_z v\Omega}{mn}\right)=\\&-\left\{\left(\frac{f}{mn}\right)+v\frac{\partial}{\partial \xi}\left(\frac{1}{n}\right)-u\frac{\partial}{\partial \eta}\left(\frac{1}{m}\right)\right\}H_z u\\&-\left(\frac{H_z}{m}\right)\left(\frac{\partial \phi}{\partial \eta}+\frac{g\rho}{\rho_0}\frac{\partial z}{\partial \eta}+g\frac{\partial \zeta}{\partial \eta}\right)+\\&\frac{1}{mn}\frac{\partial}{\partial s}\left[\frac{(K_M+\upsilon)}{H_z}\frac{\partial v}{\partial s}\right]+\frac{H_z}{mn}(F_v+D_v)\end{aligned} \tag{2.34b}$$

$$\frac{\partial \phi}{\partial s}=-\frac{gH_z\rho}{\rho_0} \tag{2.34c}$$

Equation for potential temperature

$$\begin{aligned}&\frac{\partial}{\partial t}\left(\frac{H_z T}{mn}\right)+\frac{\partial}{\partial \xi}\left(\frac{H_z uT}{n}\right)+\frac{\partial}{\partial \eta}\left(\frac{H_z vT}{m}\right)+\frac{\partial}{\partial s}\left(\frac{H_z \Omega T}{mn}\right)=\\&\frac{1}{mn}\frac{\partial}{\partial s}\left[\frac{(K_T+\upsilon_T)}{H_z}\frac{\partial T}{\partial s}\right]+\frac{H_z}{mn}(F_T+D_T)\end{aligned} \tag{2.35}$$

Equation for salinity

$$\begin{aligned}&\frac{\partial}{\partial t}\left(\frac{H_z S}{mn}\right)+\frac{\partial}{\partial \xi}\left(\frac{H_z uS}{n}\right)+\frac{\partial}{\partial \eta}\left(\frac{H_z vS}{m}\right)+\frac{\partial}{\partial s}\left(\frac{H_z \Omega S}{mn}\right)=\\&\frac{1}{mn}\frac{\partial}{\partial s}\left[\frac{(K_S+\upsilon_S)}{H_z}\frac{\partial S}{\partial s}\right]+\frac{H_z}{mn}(F_S+D_S)\end{aligned} \tag{2.36}$$

Equation of state for the seawater density

$$\rho=\rho(T,S,P) \tag{2.37}$$

The "vertical velocity" in these coordinates,

$$\Omega(\xi,\eta,s,t)=\frac{1}{H_z}\left[w-(1+s)\frac{\partial\zeta}{\partial t}-mu\frac{\partial z}{\partial\xi}-nv\frac{\partial z}{\partial\eta}\right] \tag{2.38}$$

includes both "upwelling" and "up-sloping" components of the vertical movement. Note that all vertical boundary conditions remain unchanged.

The EXTERNAL (or barotropic) MODE equations

If the total depth of the water column and the depth average of *u* and *v* are given by

$$D\equiv\zeta(\xi,\eta,t)+h(\xi,\eta)$$

$$\bar{u}\equiv\left(\frac{1}{D}\right)\int_{-1}^{0}H_z u\,ds$$

$$\bar{v}\equiv\left(\frac{1}{D}\right)\int_{-1}^{0}H_z v\,ds$$

The **free-surface equation** is

$$\frac{\partial}{\partial t}\left(\frac{\zeta}{mn}\right)+\frac{\partial}{\partial\xi}\left(\frac{D\bar{u}}{n}\right)+\frac{\partial}{\partial\eta}\left(\frac{D\bar{v}}{m}\right)=0 \tag{2.39}$$

The **momentum equations vertically integrated** are

$$\begin{aligned}&\frac{\partial}{\partial t}\left(\frac{D\bar{u}}{mn}\right)+\frac{\partial}{\partial\xi}\left(\frac{D\bar{u}\bar{u}}{n}\right)+\frac{\partial}{\partial\eta}\left(\frac{D\bar{u}\bar{v}}{m}\right)=\frac{Df\bar{v}}{mn}+\left[\bar{v}\bar{v}\frac{\partial}{\partial\xi}\left(\frac{1}{n}\right)-\bar{u}\bar{v}\frac{\partial}{\partial\eta}\left(\frac{1}{m}\right)\right]D\\&-\frac{D}{n}\left(\frac{\partial\bar{\phi}_2}{\partial\xi}+g\frac{\partial\zeta}{\partial\xi}\right)+\frac{D}{mn}\left(\bar{F}_u+\bar{D}_{hu}\right)+\frac{1}{mn}\left(\tau_s^{\xi}-\tau_b^{\xi}\right)\end{aligned} \tag{2.40a}$$

$$\begin{aligned}&\frac{\partial}{\partial t}\left(\frac{D\bar{v}}{mn}\right)+\frac{\partial}{\partial\xi}\left(\frac{D\bar{u}\bar{v}}{n}\right)+\frac{\partial}{\partial\eta}\left(\frac{D\bar{v}\bar{v}}{m}\right)=-\frac{Df\bar{u}}{mn}-\left[\bar{u}\bar{v}\frac{\partial}{\partial\xi}\left(\frac{1}{n}\right)-\bar{u}\bar{u}\frac{\partial}{\partial\eta}\left(\frac{1}{m}\right)\right]D\\&-\frac{D}{m}\left(\frac{\partial\bar{\phi}_2}{\partial\eta}+g\frac{\partial\zeta}{\partial\eta}\right)+\frac{D}{mn}\left(\bar{F}_v+\bar{D}_{hv}\right)+\frac{1}{mn}\left(\tau_s^{\eta}-\tau_b^{\eta}\right)\end{aligned} \tag{2.40b}$$

Note that ϕ_2 includes the $\partial z/\partial\xi$ term, $\bar{D}_{hu}$ and $\bar{D}_{hv}$ are the horizontal viscosity, and the vertical viscosity only contributes through the upper and lower boundary conditions.

2.3. Some numerical characteristics

2.3.1. Vertical grid discretization

As in ROMS the governing equations are solved over variable bottom topography using terrain-following coordinates as described in subsection 2.2.3; each grid cell may have different level thickness (H_z) and volume (Hedström, 2009). The model state variables are vertically staggered so that u, v, ρ, T and S are located at the centre of the grid cell, whereas Ω, w, and vertical mixing variables are located at the bottom and top faces of cell (Fig. 2.2). The total thickness of the water column is $\zeta(i,j)+h(i,j)$.

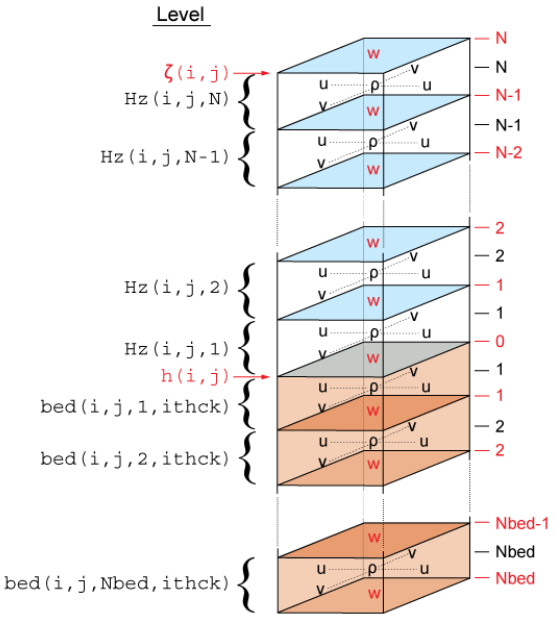

Figure 2.2 Locations of variables on staggered vertical grid (https://www.myroms.org/).

2.3.2. Horizontal grid discretization

In the horizontal, the ROMS governing equations are solved over boundary-fitted, orthogonal curvilinear coordinates (ξ, η) as described in subsection 2.2.4. The horizontal arrangement of variables is equivalent to the Arakawa-C grid (Fig. 2.3).

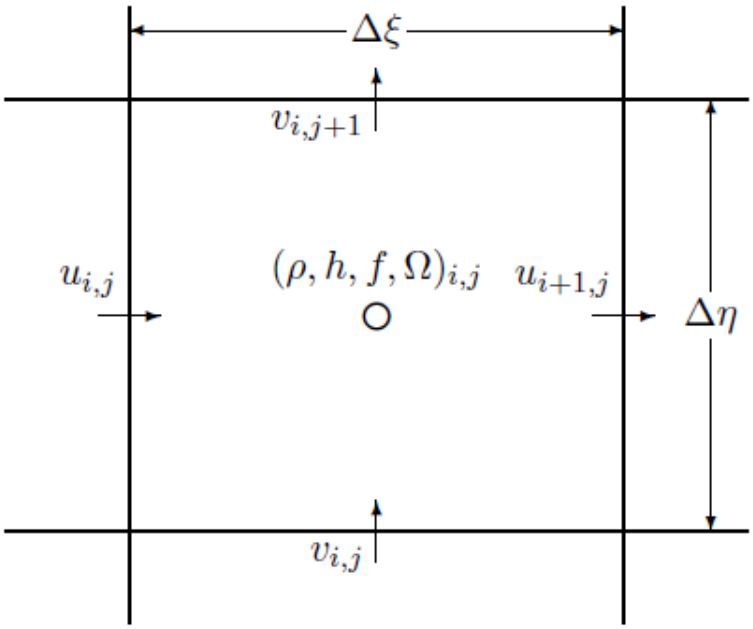

Figure 2.3 Locations of variables on an Arakawa-C grid (After Hedström, 2009).

2.3.3. Mode splitting

For computational efficiency, the governing equations for momentum are solved using a split-explicit time-stepping scheme which requires a special treatment and coupling between the barotropic and baroclinic modes (Shchepetkin and McWilliams, 2005). ROMS runs at two different time-steps, a shorter time step for the barotropic (or external) mode and a longer time step for the baroclinic (or internal) mode. A finite number of barotropic time steps, within each baroclinic step, are carried out to evolve the free-surface and vertically integrated momentum equations. In order to avoid the aliasing of frequencies resolved by the barotropic steps but unresolved by the baroclinic step, the barotropic fields are time averaged before they replace those values obtained with a longer baroclinic time step (Shchepetkin and McWilliams, 2005). A cosine-shape time filter, centred at the new time level, is used for the averaging of the barotropic fields. In addition, the separated time-stepping is constrained to maintain exactly both volume conservation and constancy preservation properties which are needed for the tracer equations (Leapfrog) and corrector (Adams-Moulton) time-stepping algorithm which is very robust and stable (Shchepetkin and McWilliams, 2005).

2.3.4. The pressure gradient scheme

It is well-known that the major advantage of terrain-following coordinate ocean models is the transformation of the surface and bottom layers to σ-surfaces, but this is also the origin of the pressure-gradient error (e.g. Haney, 1991; Mellor et al., 1994; Song, 1998; Song and Wright, 1998; Shchepetkin and McWilliams, 2003). This error arises because in σ-coordinates, the pressure-gradient force in the momentum equations is determined by the sum of two terms:

$$\left(\frac{\partial p}{\partial x}\right)_z = \frac{\partial p}{\partial x} - \frac{\sigma}{h}\frac{\partial p}{\partial \sigma}\frac{\partial h}{\partial x} \tag{2.41a}$$

$$\left(\frac{\partial p}{\partial y}\right)_z = \frac{\partial p}{\partial y} - \frac{\sigma}{h}\frac{\partial p}{\partial \sigma}\frac{\partial h}{\partial y} \tag{2.41b}$$

where $\sigma \equiv z/h$. The first term on the right-side of Eq. (2.41) involves the gradient of pressure along a constant σ-surface and the second is the hydrostatic correction. There are evidence of that near steep topography, these two terms are large, comparable in magnitude and tend to cancel each other; consequently a small error in computing either term can result in a large error in the resulting horizontal pressure-gradient. Another source of error, the hydrostatic inconsistency (cf. Haney, 1991), can occur when using second-order central differences in the discretization of Eq. (2.41). To reduce this error, the scheme implemented in ROMS is the weighted Jacobian formulation proposed by Song (1998). As pointed out by the author, this formulation was designed to minimize truncation errors and to retain integral properties such as mass, energy, and vorticity (see also Song and Wright, 1998). If *s* is the generalized terrain-following (*s*-stretched) coordinate system, then the pressure-gradient force is given by

$$\left(\frac{\partial p}{\partial x}\right)_z = \left(\frac{\partial p}{\partial x}\right)_{z=\zeta} - \frac{g}{\rho_0}\int_s^0 \left(\frac{\partial z}{\partial s'}\frac{\partial \rho}{\partial x} - \frac{\partial z}{\partial x}\frac{\partial \rho}{\partial s'}\right) ds' \tag{2.42a}$$

$$\left(\frac{\partial p}{\partial y}\right)_z = \left(\frac{\partial p}{\partial y}\right)_{z=\zeta} - \frac{g}{\rho_0}\int_s^0 \left(\frac{\partial z}{\partial s'}\frac{\partial \rho}{\partial y} - \frac{\partial z}{\partial y}\frac{\partial \rho}{\partial s'}\right) ds' \tag{2.42b}$$

Here vertical variations in the horizontal pressure gradient are given by an integral of the Jacobian:

$$J(x, z, \rho) = \left(\frac{\partial z}{\partial s}\frac{\partial \rho}{\partial x} - \frac{\partial z}{\partial x}\frac{\partial \rho}{\partial s}\right) \tag{2.43a}$$

$$J(y,z,\rho)=\left(\frac{\partial z}{\partial s}\frac{\partial \rho}{\partial y}-\frac{\partial z}{\partial y}\frac{\partial \rho}{\partial s}\right) \tag{2.43b}$$

Song (1998) point out that the formulation in terms a Jacobian is significant since it is independent of the particular form of the vertical coordinate. Nowadays, the discretization of the horizontal pressure-gradient force in ROMS is based on the numerical algorithm developed by Shchepetkin and McWilliams (2003). This algorithm is based on the reconstruction of the density field and the physical z-coordinate as continuous functions of transformed coordinates with subsequent analytical integration to compute the pressure-gradient force. As pointed by the authors, this approach allows higher order of accuracy at the same time that retains and expands several important symmetries of the original second-order scheme to high orders. In practice, however, smoothing of bottom topography is a common way to reduce pressure-gradient error and numerical instability. Realistic topography is fundamental for a correct representation of ocean dynamics; therefore, in order to reduce the error associated with the calculation of the pressure-gradient in *s*-coordinates, it is highly recommended to use a high horizontal resolution, a higher vertical resolution near the surface and the bottom and to perform some degree of topographical smoothing under the condition that it does not smear out important topographic features.

2.3.5. The advection schemes

The advection scheme for momentum in ROMS consists of a third-order upstream-biased algorithm (cf. Shchepetkin and McWilliams, 1998). Because of the implicit diffusion in this scheme, explicit lateral viscosity is not needed, except in sponge layers near the open boundaries where it increase smoothly close to the lateral open boundaries. Concerning tracers is known that spurious diapycnal mixing (cf. Barnier et al., 1998; Griffies et al., 1999) is produced by using the third-order upstream advection scheme. A new algorithm was implemented in ROMS_AGRIF, which is also a third-order upstream advection scheme but the diffusion part of it is rotated (cf. Beckers et al., 2000) along isopycnal surface to avoid spurious diapycnal mixing and loss of water masses (Marchesiello et al., 2009; Lemarié et al., 2012).

2.3.6. Vertical mixing parameterization

In our configuration, the vertical mixing parameterization was calculated using the so-called Large, McWilliams and Doney K-Profile Parameterization (LMD_KPP) scheme. This matches separate parameterizations for vertical mixing of the surface boundary layer and the ocean interior (Durski et al., 2004). A formulation based on boundary layer similarity theory of turbulence is applied in the water column above a calculated boundary layer depth. This parameterization is then matched at the interior with schemes to account for local shear, internal wave and double diffusion mixing effects. The surface boundary layer depth depends on the surface forcing, the buoyancy and the velocity profile and is determined by equating a bulk Richardson number relative to the surface to a critical value (typically in the range 0.25-0.5; Hedström, 2009). The LMD_KPP scheme has been shown to simulate accurately processes such as convective boundary layer deepening, diurnal cycling, and storm forcing (further details can be found in Large et al., 1994; Durski et al., 2004; Hedström, 2009).

Chapter 3

A regional model for the NW Mediterranean Sea

3.1. Introduction

It is well known that the assessment of the predictive capability of a numerical model is necessary before it is used with any degree of confidence for either scientific or operational purposes (cf. Holt et al., 2005). In that context, the results from a three-dimensional regional circulation model (hereinafter, REGIONAL-model) are presented in this chapter in order to compare the model performance with remotes sensing and in-situ observations, as well as literature. This exercise of validation is useful because it helps to assess the ability of the REGIONAL-model to reproduce the major features of the NW Mediterranean Sea hydrography and general (large-scale) circulation.

3.2. Model set-up

The REGIONAL-model domain extends from 39°00'-44°35'N to 00°30'W-09°00'E. A horizontal curvilinear grid was used with ~4km horizontal resolution and 32 terrain-following vertical levels with higher resolution near the surface and the bottom (θ_s=6, θ_b=1, and h_c=10m). The bottom topography was based on ETOPO2 global dataset (Smith and Sandwell, 1997) mapped onto the domain using bilinear interpolation. Although the error associated with the computation of the horizontal pressure-gradient force in terrain-following coordinates is reduced by using a density Jacobian algorithm with spline reconstruction of the vertical profiles (see further details in subsection 2.3.4), some degree of smoothing topography was performed to ensure a stable and accurate simulation. The smoothing was carried out with a Shapiro filter passed on the topography (h) until r (= $\Delta h/2h$) was less than 0.2 (see Haidvogel and Beckmann, 2000). Initial and lateral open boundary conditions were based on the World Ocean Atlas (WOA01) monthly climatology with spatial resolution of 0.25 degrees (Boyer et al., 2005). Since this dataset and model have different horizontal resolutions, a bilinear interpolation was necessary. A correction was applied to the normal baroclinic and barotropic velocities at the lateral open boundaries to ensure volume conservation (e.g. Marchesiello et al., 2001; Mason et al., 2010). The lateral open boundary conditions were specified using Orlanski and Flather schemes (Marchesiello et al., 2001) for the baroclinic and barotropic modes, respectively. As pointed out in subsection 2.3.5, the third-order upstream-biased advection scheme is implicitly dissipative; therefore explicit lateral viscosity was set to zero everywhere in the model's domain except in a sponge layer (50km wide) near the lateral open boundaries where the viscosity (50

m^2/s) increases smoothly toward the boundary. In order to prevent spurious diapycnal mixing, a third-order upstream-biased advection scheme with the diffusion part rotated along isopycnal surfaces was used for tracers. The model was run using climatological atmospheric forcing. Wind stress, heat and freshwater (evaporation minus precipitation, E-P) fluxes at the air-sea interface were computed with a bulk formula (see Appendix) using QuikSCAT monthly climatology 2000-2007 with resolution of 0.25 degrees (Risien and Chelton, 2008) and Comprehensive Ocean Atmosphere Data Set (COADS) monthly climatology with resolution of 0.5 degrees (da Silva et al., 1994). Monthly mean freshwater discharges from the "Compagnie Nationale du Rhône" and the "Confederación Hidrográfica del Ebro" were prescribed at the mouths of the Rhône (~43°20'N, 4°51'E) and Ebro (~40°43'N, ~0°52'E) rivers, respectively. Since the NW Mediterranean is a region with micro-tidal regime (tidal range less than 20 cm; Arabelos et al., 2011), in our configuration there was no tidal forcing. A ten-year simulation with baroclinic and barotropic time-steps of 100 and 12 s was conducted to attain a nearly repeating annual cycle. Here we analyse model results from the last year of simulation.

3.3. Model results and validation

3.3.1. Sea surface temperature

The spatial pattern of sea surface temperature (SST) was examined through maps of SST in winter (January-March) and summer (July-September) from Terra-MODIS monthly climatology 2000-2010 (9km) and REGIONAL-model results (Fig. 3.1). Both observed and simulated SST exhibit a winter surface thermal structure moderately homogeneous, particularly from the northern Catalan Sea to the northern Liguro-Provençal subbasin. In this region the SST does not exceed 13-14°C. In general, the lower sea surface temperatures (~13°C) are observed on the Gulf of Lions shelf and the higher (~14.5-16°C) on the southern parts of the Catalan Sea and the Liguro-Provençal subbasin. The SST clearly increases in summer. In this season, the lower sea surface temperatures (~20-22°C) are mainly observed over the Gulf of Lions shelf and open-sea, while the higher (>25°C) are observed on the whole Catalan Sea and the southernmost part of the Liguro-Provençal subbasin. Although, in general, both observed and simulated SST display a thermal structure with SST decreasing northward, there are some differences between them (see lower panels in Fig. 3.1). The higher deviations are observed on the Gulf of Lions shelf and open sea, as well as on the north-western part of the Liguro-Provençal subbasin.

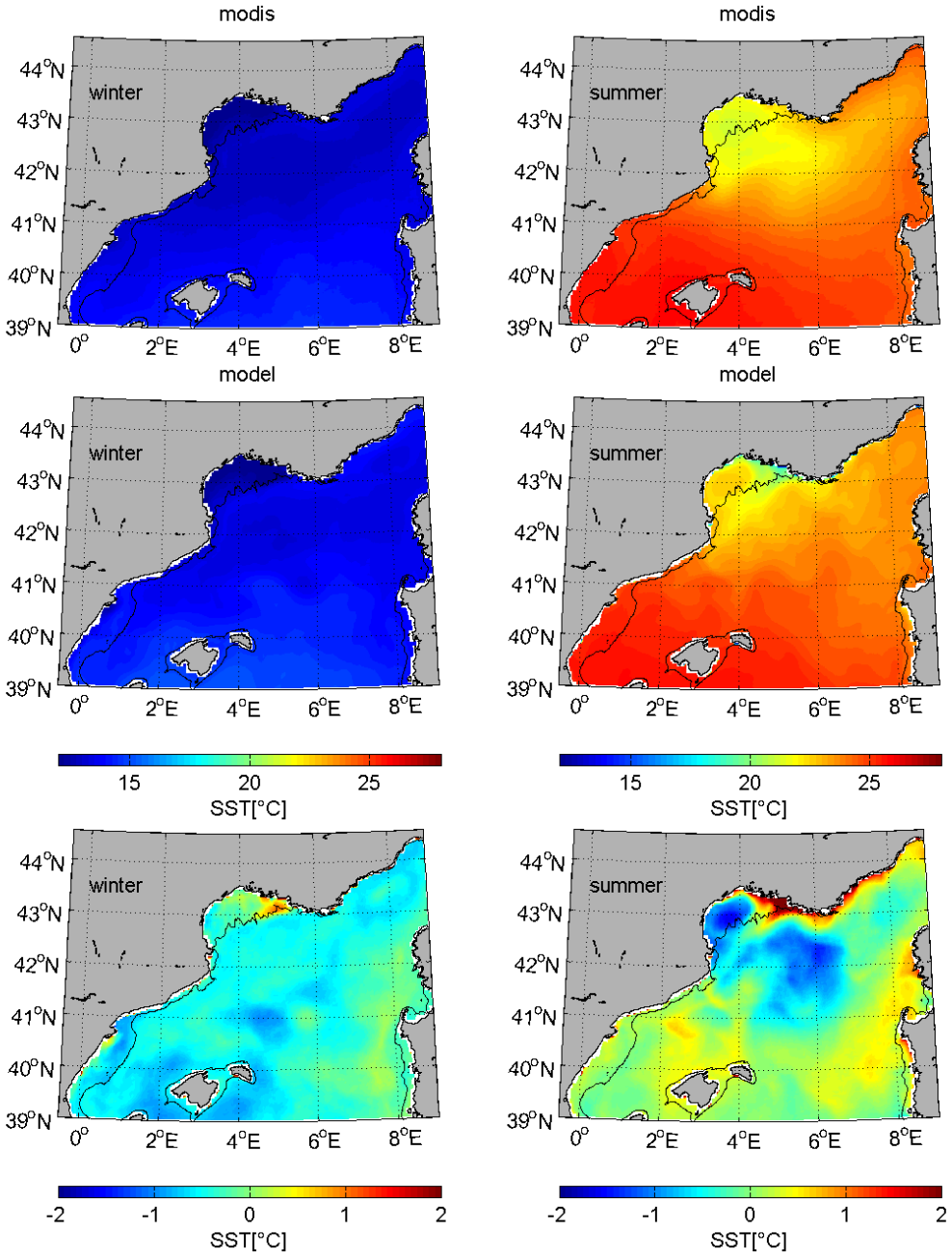

Figure 3.1 Comparison of sea surface temperature (SST) in winter (January-March) and summer (July-September) from Terra-MODIS monthly climatology 2000-2010 and REGIONAL-model results. The difference between SST fields (MODIS-SST minus MODEL-SST) is also given in the lower panels.

The ability of the REGIONAL-model to capture the seasonal cycle of SST was analyzed by means of time-series of area-averaged SST from Terra-MODIS monthly climatology and model results (Fig. 3.2). The simulated SST is in the range defined by the interannual variability of the

observed SST. The correlation coefficient between the monthly-averaged SST fields was high ($R = 0.99$, $p < 0.01$) indicating that the seasonal cycle of SST was fairly well reproduced by the model.

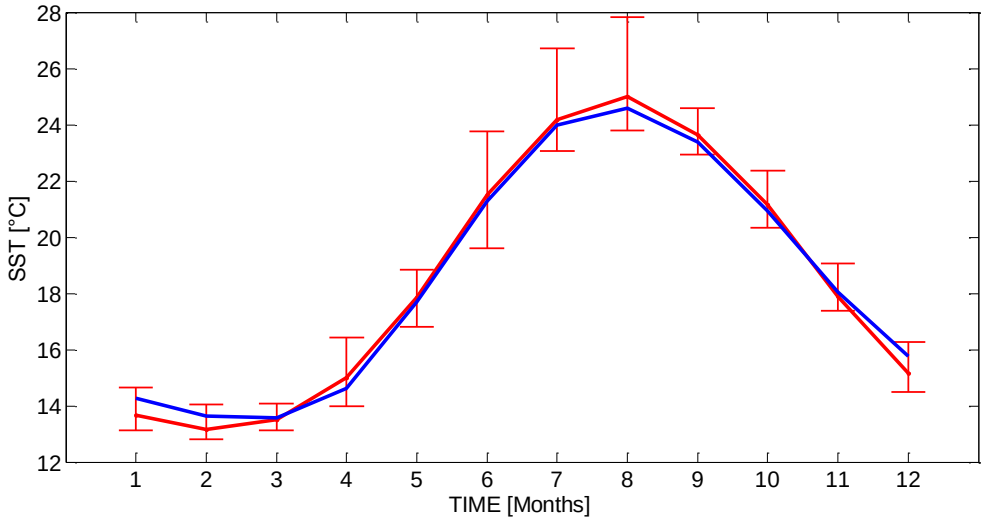

Figure 3.2 Monthly mean sea surface temperature (SST) averaged over the REGIONAL-model's domain from Terra-MODIS monthly climatology 2000-2010 (red line) and model results (blue line). Vertical bars represent the interannual variability of the Terra-MODIS climatology.

3.3.2. Vertical distribution of temperature and salinity

Vertical profiles of potential temperature and salinity averaged over the REGIONAL-model's domain from EU-MEDAR-MEDATLAS-II climatology (http://doga.ogs.trieste.it/medar/climatologies/) were used in order to analyse how well the REGIONAL-model fits the seasonal cycle of the water column stratification (Fig. 3.3). Although the simulated temperature tends to be slightly overestimated (less than 0.5°C) between ~50 and 150 m depth, the summer stratification and winter homogenization of the water column were fairly well reproduced by the model. Moreover, although there was also deviations in salinity (less than 0.2 near the surface and less than 0.1 between ~200 and 400 m depth), in general, the simulated salinity fell within the range defined by the spatial variability of the climatology. Thus, considering the magnitude and shape of the vertical profiles, the overall performance of the model was reasonably good.

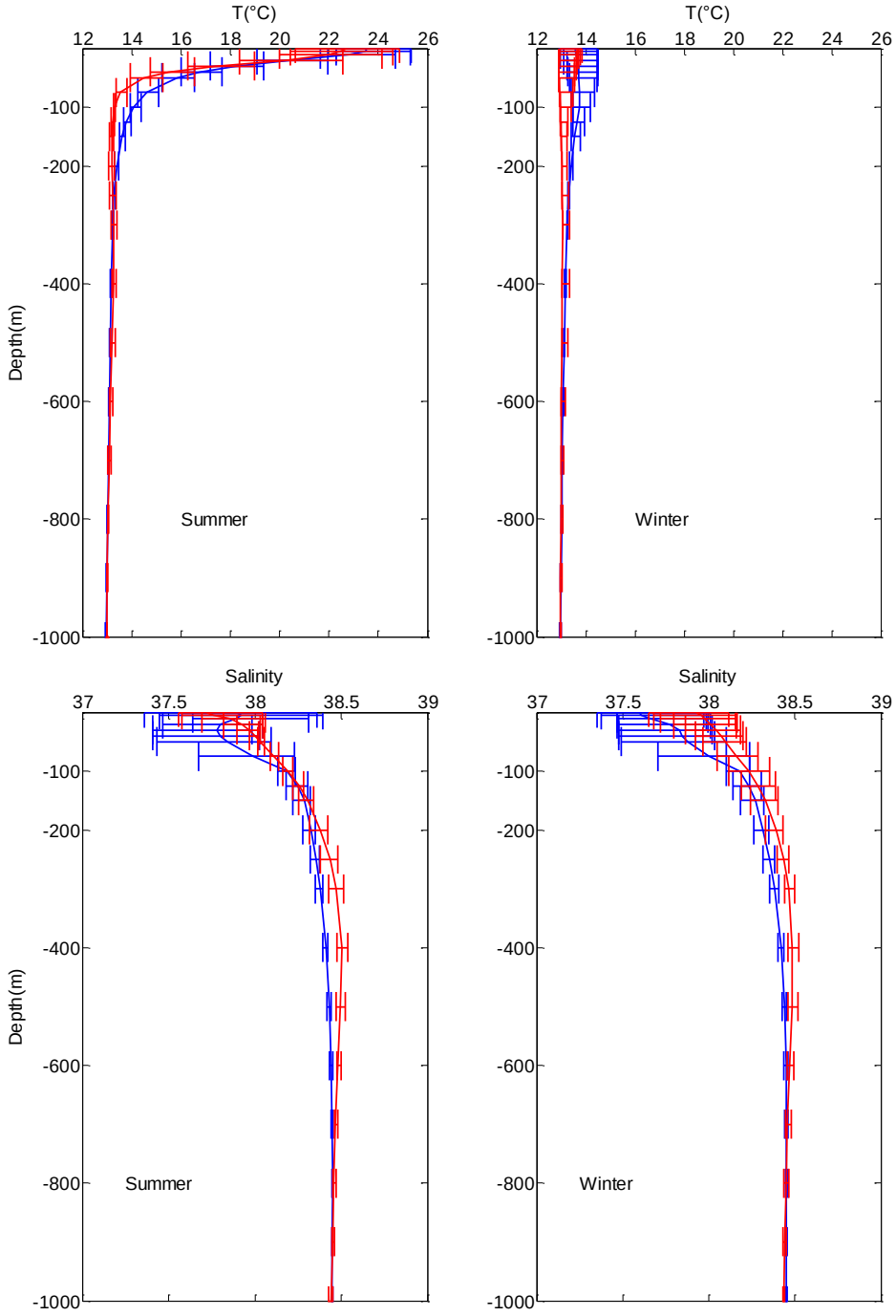

Figure 3.3 Mean winter and summer vertical profiles of potential temperature (upper panels) and salinity (lower panels) averaged over the REGIONAL-model's domain from EU-MEDAR-MEDATLAS-II climatology (red line) and model results (blue line). Horizontal bars represent the spatial variability.

3.3.3. Water masses

The NW Mediterranean Sea is essentially a system of three layers: 1) an upper layer between the surface and ~100/200 m; 2) an intermediate layer between ~200 and ~600/800 m; and 3) a deep layer down to the bottom. The upper layer is formed by water of Atlantic origin, which is modified along its path across the basin (e.g. Salat et al., 2002) and displays salinity and temperature values from ~36.5 to 38.2 and from ~13-14°C to 27°C, respectively. This water mass receives the name of Modified Atlantic Water (MAW). The intermediate layer is water of Levantine origin, which is formed during the wintertime (e.g. Brasseur et al., 1996; Lascaratos et al., 1999) and displays a salinity maximum ranging from ~38.5 to 38.7, as well as potential temperature from ~13°C to 14°C. This water mass is known by the name of Levantine Intermediate Water (LIW). The deepest layer is occupied by the Western Mediterranean Deep Water (WMDW), which is mainly formed in the Gulf of Lions shelf and open sea during the wintertime (e.g. MEDOC Group, 1970; Schott et al., 1996). The WMDW is characterized by salinity values ranging from ~38.4 to 38.5 and potential temperatures of about 12.5-12.9°C.

MAW enters into the NW Mediterranean Sea from the Algerian subbasin via the Balearic channels and through the opening between Menorca and Sardinia (i.e. along ~40°N), as well as from the Tyrrhenian Sea through the Corsican Channel. In the north-eastern Liguro-Provençal subbasin, MAW coming from the west of Corsica joins MAW coming from the Tyrrhenian Sea. LIW also enters into the north-eastern Liguro-Provençal subbasin via the Corsican Channel, but the main branch follows along the east side of Corsica and Sardinia and then emerging from the Sardinian Channel flows northward on the west side of the Islands before it reaches the north-eastern Liguro-Provençal subbasin. Here, MAW and LIW form a return south-westward flow (i.e. the Northern Current) along the continental shelf/slope of the northern Liguro-Provençal subbasin, the Gulf of Lions and the Catalan Sea. The WMDW spreading from the sites of formation also follows a cyclonic path around the deeper part of the NW Mediterranean Sea. See, for example, Millot (1999), Pinardi and Masetti (2000), and Pinardi et al. (2013) for a general view.

Latitudinal (along 39.5°N) and longitudinal (along 5.5°E) vertical cross-sections of mean winter and summer salinity have been chosen to show the presence of MAW, LIW and WMDW in the REGIONAL-model's results. From the latitudinal sections (Fig. 3.4A-B), it is possible to recognise the signature of MAW as a salinity minimum (~37.8-38.0) from the sea surface to ~100/200 m depth. It is also possible to identify the LIW core as a salinity maximum (≥ 38.50)

between ~400 and 600 m depth and the signature of WMDW as a range of salinity from ~38.42 to ~38.48 below ~800 m depth. From the longitudinal sections (Fig. 3.4C-D), it is possible to recognise MAW reaching the NW Mediterranean Sea from the Algerian subbasin and MAW flowing from the northern Liguro-Provençal subbasin. Below MAW, it is also possible to identify the LIW signature from the southernmost part of the REGIONAL-model's domain to the continental slope of the Gulf of Lions where it is observed up to ~1000/1500 m depth. The signature of the WMDW is also found in the deepest part of the basin. These results show that the REGIONAL-model is capable of reproducing the major water masses (i.e. MAW, LIW and WMDW) in the NW Mediterranean Sea.

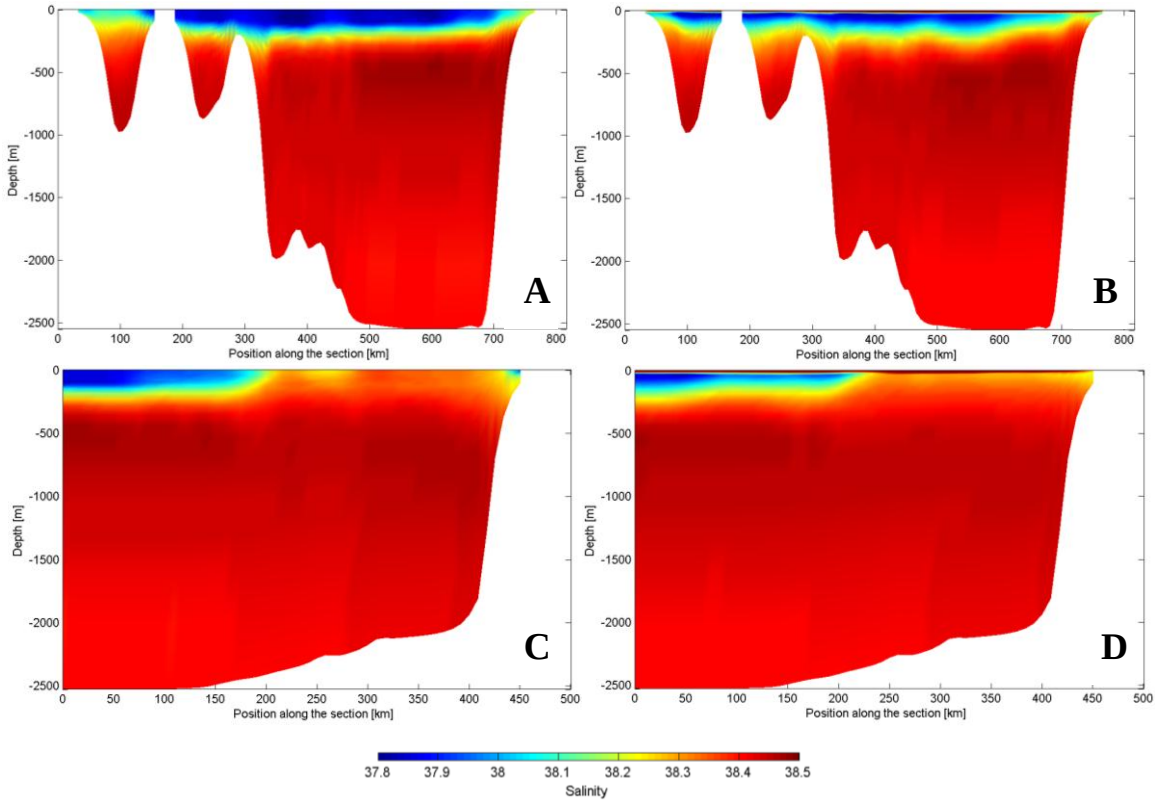

Figure 3.4 Vertical cross-sections of seasonal mean salinity along 39.5°N (A: winter, B: summer) and along 5.5°E (C: winter, D: summer) from REGIONAL-model results.

3.3.4. The general (large-scale) circulation

The NW Mediterranean Sea is characterized by a well-defined large-scale cyclonic circulation (see Fig. 1.1). The most significant feature is the Northern Current (NC) originated in the north-eastern part of the Liguro-Provençal subbasin where the Eastern Corsican Current (ECC) and Western Corsican Current (WCC) flowing northward on both sides of Corsica Island joins (e.g. Birol et al., 2010; Poulain et al., 2012; Pinardi et al., 2013). From the Ligurian Sea the NC flows along the continental shelf/slope as far as the southernmost part of the Catalan Sea where it splits into two branches: while the first one flows southward crossing the Ibiza Channel, the second one re-circulates north-eastward contributing to the formation of the Balearic Current on the northern side of the Balearic Islands (e.g. López-García et al., 1994; García-Ladona et al., 1996).

In order to examine how well the REGIONAL-model reproduces the time-mean cyclonic circulation and its major currents, we compare the simulated mean sea surface high (MSSS) and associated geostrophic flow with the mean dynamic topography (MDT) and geostrophic flow derived from altimetric data, in-situ measurements and an ocean general circulation model of the Mediterranean Sea for the period 1993-1999 (Rio et al., 2007) in Fig. 3.5. In both fields the time-mean cyclonic circulation is clearly evident; however, there are some differences. For example, the surface signature of the WCC is very clear in the MDT, but not in the model results. In contrast, the north-eastern section of the NC appears well-defined in the model results, but not in the MDT. On the other hand, the observed NC extension appears to track further south than the simulation indicates. It should be mentioned that the NC south-westwards extension is characterized by a weakened flow and increased variability linked with complex interactions with incoming MAW near the Balearic Channels (e.g. López-García et al., 1994; García-Ladona et al., 1996). In spite of the discrepancy, in both fields the BC pathway is well-defined on the northern side of the Balearic Islands. The time-mean cyclonic circulation is also evident in REGIONAL-model maps of annual mean velocities at depths of 30, 100, 200 and 400 m (Figs. 3.6 and 3.7). In particular the NC signature is very clear along the continental shelf/slope of the northern Liguro-Provençal subbasin, the Gulf of Lions and the Catalan Sea. The NC extends down to 400 m depth with speed of ~20-30 cm s^{-1}. The Balearic Current signature is also very clear and extends down to 200 m depth with speed of ~20 cm s^{-1}.

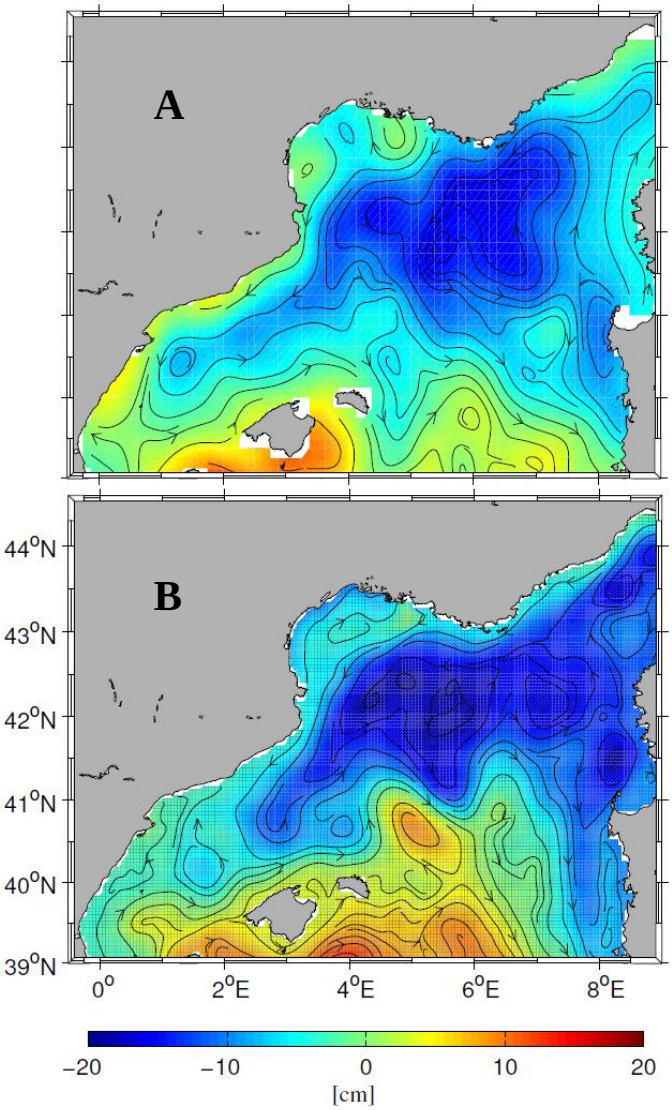

Figure 3.5 (**A**) Mean Dynamic Topography (MDT) derived from altimetric data, in-situ measurements and an ocean general circulation model of the Mediterranean Sea for the period 1993-1999 (Rio et al., 2007) and (**B**) Mean Sea Surface High (MSSH) from REGIONAL-model results: Streamlines are overplotted; the arrows indicate the direction of the flow.

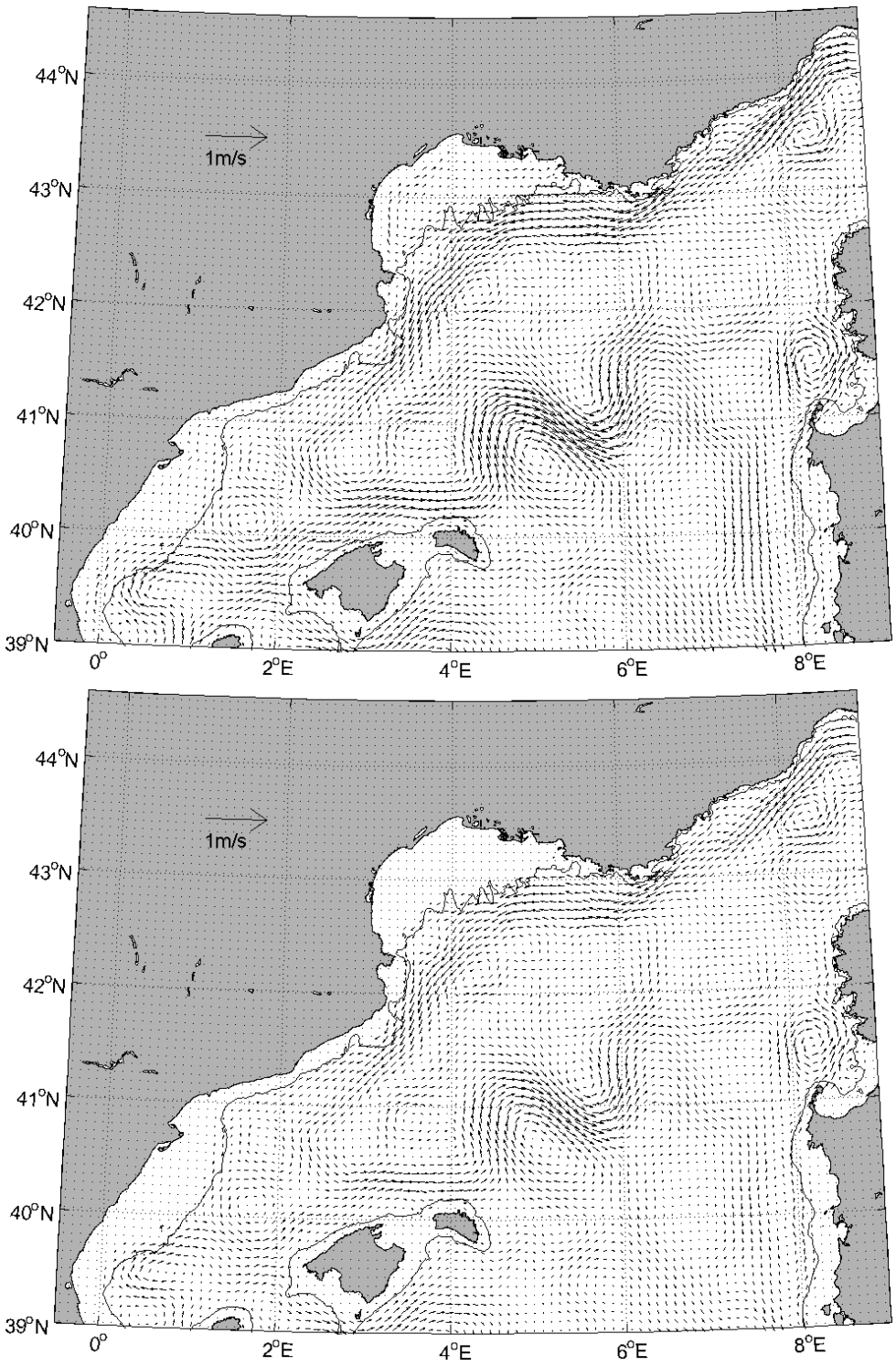

Figure 3.6 Annual mean currents at depths of 30 m (upper panel) and 100 m (lower panel) from REGIONAL-model results. Note the Northern Current signature along the shelf/slope from the Ligurian Sea to the Catalan Sea. (See nomenclature in Fig. 1.1).

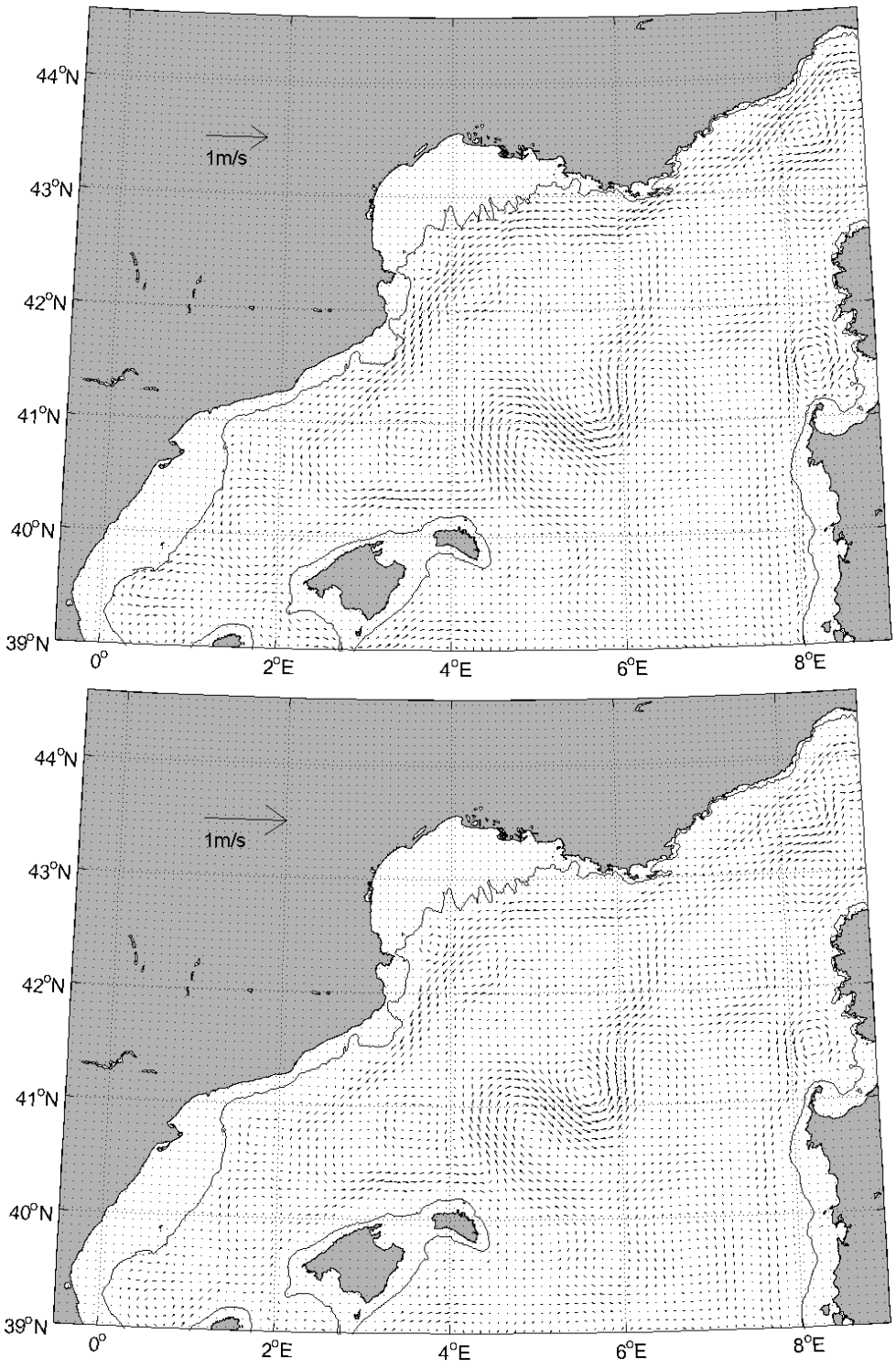

Figure 3.7 Annual mean currents at depths of 200 m (upper panel) and 400 m (lower panel) from REGIONAL-model results. Note the Northern Current signature along the shelf/slope from the Ligurian Sea to the Catalan Sea. (See nomenclature in Fig. 1.1).

3.4. Summary

The objective of this chapter was to assess the ability of a regional model based on the Regional Ocean Modeling System (ROMS) to reproduce the major features of the NW Mediterranean Sea hydrography and general (large-scale) circulation. To this purposes model results were validated by comparison with satellite data, in-situ observations and literature. We demonstrated that the regional model successfully reproduce the thermohaline characteristics of the principal water masses and their circulation. In particular, the model has satisfactorily reproduced the Northern Current. This validation exercise highlights that the regional model results can be used as open boundary conditions for a shelf circulation model with higher resolution.

Chapter 4

The Northern Current variability and its impact on the Blanes Canyon circulation

This chapter is an adapted version of a paper published in Progress in Oceanography (Ahumada-Sempoal et al., 2013).

4.1. Introduction

Continental margins of the world ocean are interrupted at irregular intervals by steep, narrow and abrupt submarine canyons (Hickey, 1995; Allen and Durrieu de Madron, 2009). Submarine canyons are hotspots of benthic biomass and productivity in the deep sea (e.g. Gili et al., 2000; Granata et al., 2004; Palanques et al., 2005; Sardà et al., 2009; De Leo et al., 2010; Ramirez-Llodra et al., 2010; Vetter et al., 2010). These topographic features are also of special interest because they play a significant role on the exchanges of energy and matter between the continental shelf and the open sea.

The NW Mediterranean Sea continental margin is one of the world's regions with high frequency of submarine canyons. In particular, the northern Catalan Sea continental margin has three large submarine canyons (from North to South: Cap de Creus Canyon, Palamós or La Fonera Canyon and Blanes Canyon) that deeply incise the continental shelf and slope (Amblas et al., 2006). These canyons act as barriers deflecting the regional flow. For example, Masó et al. (1990) observed topographic steering of the incoming current as it progress south-westward over the above mentioned canyons. According to observations (Alvarez et al., 1996) and numerical simulations (Jordi et al., 2005), the flow is more affected when the current crosses over canyons' head compared to when it crosses near the canyons' mouth. More recently, Flexas et al. (2008) observed that the regional flow is deflected along the Blanes Canyon upper walls, while Zuñiga et al. (2009) and Jordà et al. (2013) point out that intermediate and deep currents are strongly constrained by the bathymetry of the canyon.

The regional circulation in the NW Mediterranean Sea is dominated by the Northern Current (NC). The NC comes from the Ligurian Sea, flowing south-westward along the continental shelf/slope of the Gulf of Lions and the Catalan Sea. It is an energetic flow in quasi-geostrophic balance with a shelf/slope density front maintained by the salinity contrast between relatively fresh coastal waters and more saline waters offshore (Font et al., 1988; Astraldi et al., 1994; García-Ladona et al., 1996). The main flow is ~30 km wide and extends down to 300-400 m deep, characterized by speeds ranging from ~30-50 cm/s near the surface to 10-15 cm/s at the shelfbreak depth (García-Ladona et al., 1996; Flexas et al., 2002). The NC displays high spatial and temporal variability with mesoscale features such as filaments, meanders, and eddies (e.g. Wang et al., 1988; La Violette et al., 1990; Tintoré et al., 1990; Millot, 1991; Font et al., 1995; Sammari et al., 1995; Flexas et al., 2002; Rubio et al., 2005; Casella et al., 2011).

The interaction of the NC with local topographic barriers such as submarine canyons is relevant because it can cause significant vertical motions. Net upwelling/downwelling in submarine canyons has usually been associated with left/right-bounded flows (i.e. flows with the coastline on the left/right, looking downstream): However, most studies on the flow over submarine canyons focus on wind-forced flows (Allen and Durrieu de Madron (2009) and reference therein). Although the NC is an example of continuous along-slope density-driven right-bounded flow (i.e. a downwelling favourable flow), studies based on laboratory experiments and field observations have shown evidence of right-bounded flows causing local upwelling in submarine canyons. In particular, laboratory experiments indicate maximum upwelling at the shelfbreak decreasing in intensity with depth (Boyer et al., 2006). Field observations, on the other hand, show evidence of upwelling at the Blanes Canyon shelfbreak, from ~100 to 200 m depth (Flexas et al., 2008). Numerical simulations focused on Blanes Canyon also suggest upwelling (downwelling) during constant one-day northerly (easterly) wind burst (Ardhuin et al., 1999).

In this chapter the objective is to examine the Northern Current influence on the Blanes Canyon circulation; paying particular attention to upwelling/downwelling events and their seasonal variability. To this purpose, we used a high-resolution (~1.2km) 3D circulation model nested in one-way to a coarse-resolution (~4km) 3D regional model. Although it refers to a climatological simulation (i.e. no interannual variability), at this resolution, the Rossby radius of deformation for the Mediterranean Sea (5-12 km) is resolved. Therefore the model properly suites our purpose, since it adequately reproduces the NC mesoscale variability and its seasonality. Satisfactory validation of model results with remote sensing and in-situ observations supports the present findings.

4.2. Model set-up

We used a larger domain (REGIONAL-model) between 39°00'-44°35'N and 00°30'W-09°00'E (Fig. 4.1A) with ~4km horizontal resolution and 32 terrain-following vertical levels with higher resolution near the surface and the bottom (see further details in Chapter 3), and a smaller domain (afterwards CaSGoL-model) between 40°13'-43°56'N and 00°02'W-06°00'E (Fig. 4.1B) with ~1.2km horizontal resolution and 32 terrain-following vertical levels with higher resolution near the surface and the bottom (θ_s=6, θ_b=1, and h_c=10m). The CaSGoL-model was nested in one-way into the REGIONAL-model using the mesh refinement facilities of ROMS_AGRIF v3.0 (Penven et al., 2006; Debreu et al., 2012). The model grid, surface forcing,

initial and lateral open boundary conditions were built using the ROMSTOOLS v3.0 package (Penven et al., 2008). The bathymetry was based on ETOPO2 global dataset (Smith and Sandwell, 1997) mapped onto the domain using bilinear interpolation. Some degree of topographic smoothing was performed to ensure a stable and accurate simulation. To filter the topography only where it was necessary, we used a Shapiro filter which was passed on the topography until r was less than 0.2. To prevent depth mismatches between the CaSGoL-model and the REGIONAL-model (e.g. Mason et al., 2010), the following correction was applied to the bathymetry: $h_{fine} = \alpha \cdot h_{fine} + (1-\alpha)\ h_{coarse}$, where h_{fine} is the fine-grid bathymetry, h_{coarse} is the coarse-grid bathymetry interpolated to the fine grid and α is a parameter that ranges from zero at the open boundary to one over a distance of ten grid points inside the nested domain. Initial condition (IC) and lateral open boundary conditions (OBCs) for the CaSGoL-model were based on the REGIONAL-model daily-averaged outputs from the last year of simulation. Since the models have different horizontal resolutions, a bilinear interpolation was performed. A correction was applied to the normal baroclinic and barotropic velocities at the open boundaries to ensure volume conservation (Marchesiello et al., 2001; Mason et al., 2010). The OBCs were specified using a combination of an Orlanski scheme for the tracers and baroclinic velocities and a Flather scheme for the barotropic mode (Marchesiello et al., 2001). Explicit lateral viscosity was set to zero everywhere in the models' domain except in a sponge layer (30km wide) near the open boundaries where the viscosity (30 m^2/s) increases smoothly toward the boundary. For tracer a third-order upstream-biased advection scheme with the diffusion part rotated along isopycnal surfaces was used. The model was run with momentum, heat, and freshwater fluxes computed with a bulk formula (see Appendix) using QuikSCAT monthly climatology 2000-2007 with resolution of 0.25 degrees (Risien and Chelton, 2008) and COADS monthly climatology with a resolution of 0.5 degrees (da Silva et al., 1994). Monthly mean freshwater discharges were prescribed at the mouths of the Rhône and Ebro rivers, respectively. There was no tidal forcing. A ten-year simulation with baroclinic and barotropic time-steps of 33 and 4 s was conducted to attain a nearly repeating annual cycle. In this study we used the last year of simulation.

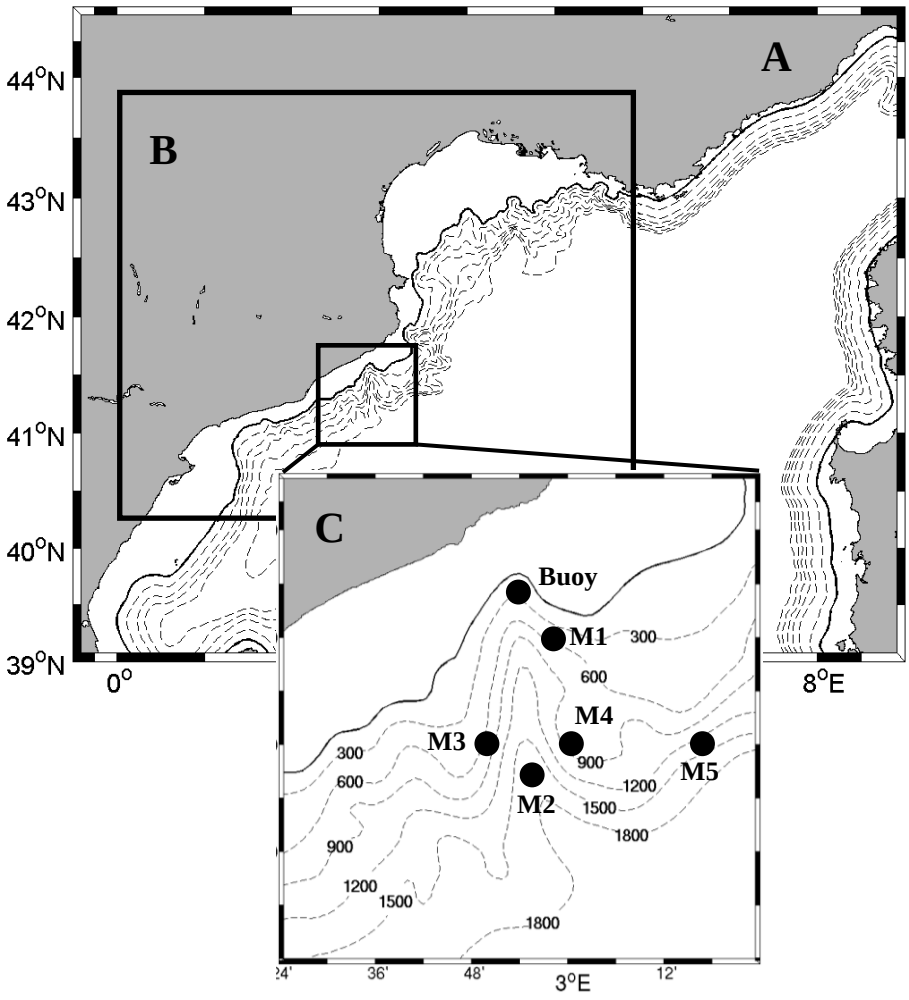

Figure 4.1 REGIONAL-model (A) and CaSGoL-model (B) domains with the Blanes Canyon subdomain (C) and locations of the OOCS sampling station (Buoy) and the RECS project's mooring lines (M1, M2, M3, M4 and M5). Further details are given in the text. The shelf break depth (that is, the 150m isobath) is showing with a solid line. The bottom topography is based on ETOPO2 (Smith and Sandwell, 1997).

Table 4.1

Topographic setting and several non-dimensional numbers

Parameter	CaSGoL model	Flexas et al., 2008; Zuñiga et al., 2009; and Jordà et al., 2013
H (axial bottom depth at the canyon mouth)	~950 m	~1100 m
h_m (depth of the canyon from its rim to the bottom)	~800 m	~950 m
W (canyon width)	~8 km	~8 km
h_m/H (fractional height)	0.84	0.86
H/L (aspect ratio, where $L=W/2$)	0.237	0.275
f (Coriolis parameter, $2\Omega\sin\varphi$, where $\Omega = 7.292 \times 10^{-5}$ rad·s^{-1} and φ=41.363°N)	9.7×10^{-5} s^{-1}	9.7×10^{-5} s^{-1}
N (buoyancy frequency, $[-g/\rho_0 (\partial\rho/\partial z)]^{-1/2}$)	1.6-2.8 $\times 10^{-3}$ s^{-1}	1.05-2.03 $\times 10^{-3}$ s^{-1}
R_d (internal radius of deformation, NH/f)	14.8-26 km	11.9-23 km
Mean thickness of the incident flow	~300-400 m	~500 m
S (stratification parameter, NH/fL)	3.7-6.6	2.9-5.6
T_r (vertical stratification scale, fL/N)	138-244	195-380
Ro (Rossby number, U/fL)	0.36-0.47	0.2-0.35

4.3. Results and discussion

The results analyzed here correspond to the sub-domain defining the Blanes submarine canyon (BC), between ~41°00'-41°46'N and ~2°24'-3°24'E (Fig. 4.1C). In order to compare topographic setting and relevant scale of motions with previous observational studies in the BC area, we estimated several topographic characteristics of the simulated canyon and non-dimensional numbers that represent the essential dynamics (e.g. Hickey, 1997; Allen and Hickey, 2010). Furthermore, to validate model outputs we used climatological (2000-2010) monthly sea surface temperature (SST) from the Terra-MODIS sensor averaged over the BC area, as well as in-situ currents from two sources: (1) the sampling station from the Operational Observatory of the Catalan Sea, OOCS (Bahamon et al., 2011) located at the canyon head (black circle marked as Buoy in Fig. 5.1C) provided near-surface currents measurements between 2009 and 2011; and (2) five moorings (see Fig. 4.1C) from the RECS project (Sardà et al., 2009) located near the canyon mouth (M1), in the canyon axis (M2), close to the west and east walls (M3 and M4, respectively), as well as upstream of the canyon (M5) provided intermediate and near-bottom current measurements between April 2003 and May 2004 (for details on moorings see Jordà et al., 2013). To compare simulated and observed currents from a climatological point of view, we estimated variance ellipses, as well as winter and summer mean and maximum current speeds from model results and observations.

Recent observational studies over the BC area have reported topographic setting and relevant scale of motions (e.g. Flexas et al., 2008; Zuñiga et al., 2009; Jordà et al., 2013). In spite of the necessary smoothing of the model bottom topography, the topographic features of the simulated canyon compare well with those reported in the above mentioned studies. For example, the width of the simulated canyon, as well as the fractional height and the aspect ratio compare fairly well with those from observations (see Table 4.1, column 2 and 3). The simulated BC is a narrow and deep canyon. According to model results, the buoyancy frequency (N) and the internal Rossby radius of deformation (R_d) range from 1.6 $x10^{-3}$ to 2.8 $x10^{-3}$ s^{-1} and from ~14 to 26 km in winter and in summer, respectively. These features compare fairly well with those reported by Flexas et al. (2008) who point out that N and R_d vary between 1.05 $x10^{-3}$ and 2.03 $x10^{-3}$ s^{-1} and between ~12 and 23 km in winter and in summer, respectively. Given that the R_d was about twice the width of the canyon and the depth of the canyon below its rim was roughly twice the depth of the incident flow (see Table 4.1, column 3), Flexas et al. (2008) suggest that the BC is a narrow and deep canyon. Other relevant non-dimensional numbers are given in Table 4.1.

4.3.1. Sea surface temperature

The seasonal cycles of the sea surface temperature (SST) from model and Terra-MODIS sensor averaged over the BC area were in good agreement (Fig. 4.2). The simulated monthly mean SST fell within the range defined by the interannual variability of the observed SST. The correlation coefficient between the two time series was high ($R=0.9915$, $p<0.01$) suggesting that the seasonal cycle of SST was well represented by the model.

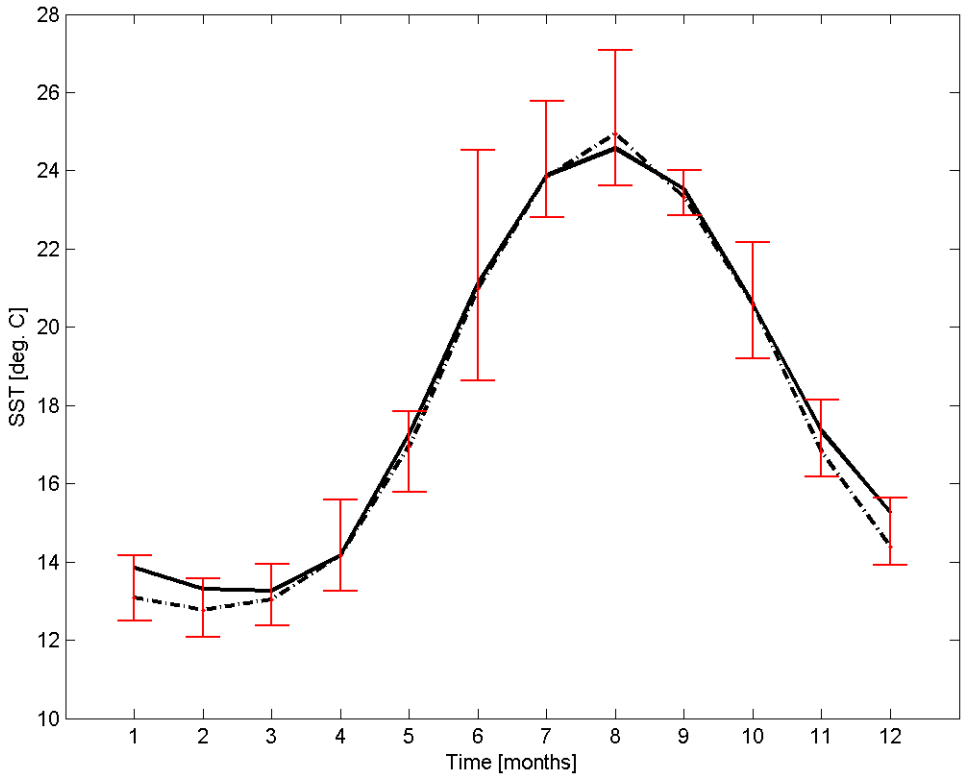

Figure 4.2 Monthly mean sea surface temperature averaged over the Blanes Canyon area from CaSGoL-model (solid line) and from Terra-MODIS sensor (dashdot line). The vertical bars represent the interannual variability of the observed sea surface temperature.

4.3.2. Mean currents

Variance ellipses (Fig. 4.3) showed that the preferential pathway of simulated and observed near-surface (at 50 m) currents over the BC head (Buoy in Fig. 4.3) was south-westward without appreciable constraint by the local topography. In contrast, the preferential pathway of simulated and observed intermediate (at 375 m and 600 m) and deep (at 900 m and 1700 m) currents (M1, M2, M3 and M4 in Fig. 4.3) was along the local isobaths showing thus the constraint of the BC bathymetry. Upstream of the BC (M5 in Fig. 4.3), the preferential pathway of simulated and observed currents was westward following also the orientation of the local isobaths. Regarding

current speeds (Table 4.2), the simulated winter and summer mean and maximum current speeds over the BC head were approximately 20 and 50% smaller than the correspondent values for observations (Buoy in Table 4.2). As depth increases, the simulated and observed current speeds were fairly similar. For example, from 375 m to 1700 m, the simulated current speeds were in general only 10% smaller than the observations. Current variability was, in general, lower in the model results (S.D. = 1-5 cm/s) than in the observations (S.D. = 1-8 cm/s; see standard deviation, S.D. in Table 5.2). Nevertheless, both simulated and observed current variability were higher in winter (simulated currents: S.D. = 2-5 cm/s; observed currents: S.D. = 2-8 cm/s) than in summer (simulated currents: S.D. = 1-2 cm/s; observed currents: S.D. = 1-4 cm/s). Furthermore, both simulated and observed current variability were higher in the upper layer (simulated currents: S.D. = 2-4 cm/s; observed currents: S.D. = 4-8 cm/s) than in deeper layers (simulated currents: S.D. = 1-4 cm/s; observed currents: S.D. = 1-4 cm/s).

The agreement between simulated and observed currents was satisfactory considering that several factors prevented an exact match: (i) the model results and observations do not correspond to the same period, so a direct comparison between simulated and observed currents was not possible; (ii) the temporal and spatial resolution of the model wind forcing (monthly climatology with resolution of ~25 km) prevented a detailed representation of the wind variability compromising the ability of the model to simulate the range of variability of the upper layer currents (e.g. Casella et al., 2011; Schaeffer et al., 2011a,b); (iii) the necessary smoothing of the BC bottom topography likely affected the representation of the current-topography interactions introducing error in the simulated intermediate and deep currents; and (iv) the horizontal resolution may still be insufficient for a representation of sub-mesoscale structures.

4.3.3. Seasonality of the Northern Current

Our results show that the Northern Current (NC) tends to be faster and deeper in winter than in summer. This seasonal evolution is illustrated by vertical sections of winter and summer mean velocity in the E-W direction taken upstream (at longitude 3°03’E) of the BC (Fig. 4.4). In winter, the core of the NC displays mean speeds of the order of 30 cm/s extending down to ~400 m depth while, in summer, it displays mean speeds smaller than 30 cm/s and does not reach deeper than 300 m. These values compare well with those obtained from observations, in which the NC displays speeds ranging from ~30-50 cm/s near the surface to 10-15 cm/s at the

shelfbreak and extending down to ~300-400 m (e.g. García-Ladona et al., 1996; Flexas et al., 2002).

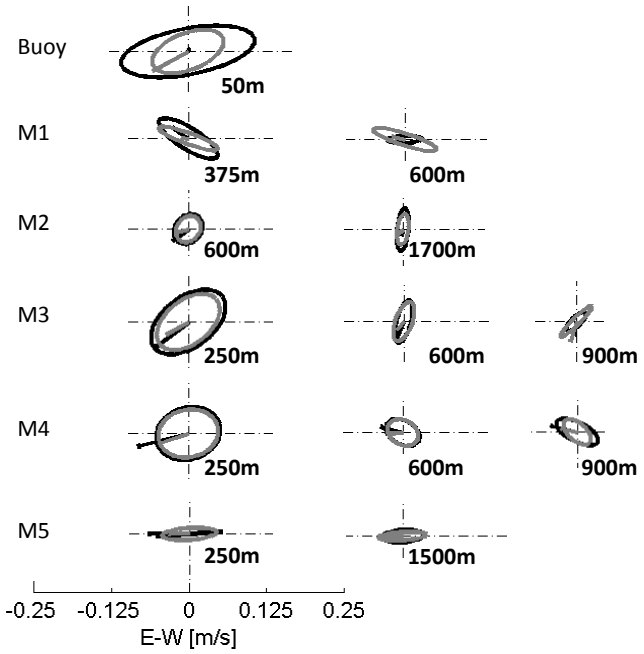

Figure 4.3 Variance ellipses from observed (black) and simulated (gray) currents at the OOCS's station (Buoy) and at the RECS project's mooring lines (M1, M2, M3, M4 and M5). Note that each semi-axis is equal to two standard deviations; therefore, 95% of the observed and simulated currents are within the ellipse.

Table 4.2

Statistic for observed and simulated current speeds at the OOCS station (Buoy) and RECS project moorings (M1, M2, M3, M4 and M5). S.D. = Standard Deviation, N/D = No Data

	Observed current speed (cm/s)				Simulated current speed (cm/s)			
	Winter		Summer		Winter		Summer	
Station	Mean ± S.D.	Max.	Mean ± S.D.	Max.	Mean ± S.D.	Max.	Mean ± S.D.	Max.
Buoy(50 m)	11 ± 4	61	10 ± 4	20	10 ± 5	23	5 ± 2	11
M1 (375 m)	6 ± 4	19	3 ± 2	10	6 ± 4	18	3 ± 2	10
M1 (600 m)	2 ± 3	19	N/D	N/D	6 ± 4	18	3 ± 2	10
M2 (600 m)	6 ± 3	14	3 ± 1	7	4 ± 2	9	2 ± 1	4
M2 (1700 m)	3 ± 3	17	2 ± 1	8	3 ± 2	12	2 ± 1	5
M3 (250 m)	9 ± 6	26	5 ± 3	15	9 ± 4	21	4 ± 2	16
M3 (600 m)	4 ± 3	17	3 ± 2	9	4 ± 2	9	3 ± 1	9
M3 (900 m)	N/D	N/D	3 ± 2	11	5 ± 3	14	4 ± 2	11
M4 (250 m)	12 ± 8	40	7 ± 2	12	9 ± 4	20	4 ± 2	9
M4 (600 m)	5 ± 2	9	3 ± 1	6	4 ± 2	11	2 ± 1	6
M4 (900 m)	N/D	N/D	4 ± 2	9	4 ± 2	12	3 ± 1	6
M5 (250 m)	10 ± 5	28	5 ± 1	8	8 ± 4	21	4 ± 2	10
M5 (1500 m)	4 ± 3	15	2 ± 1	4	6 ± 3	13	3 ± 2	8

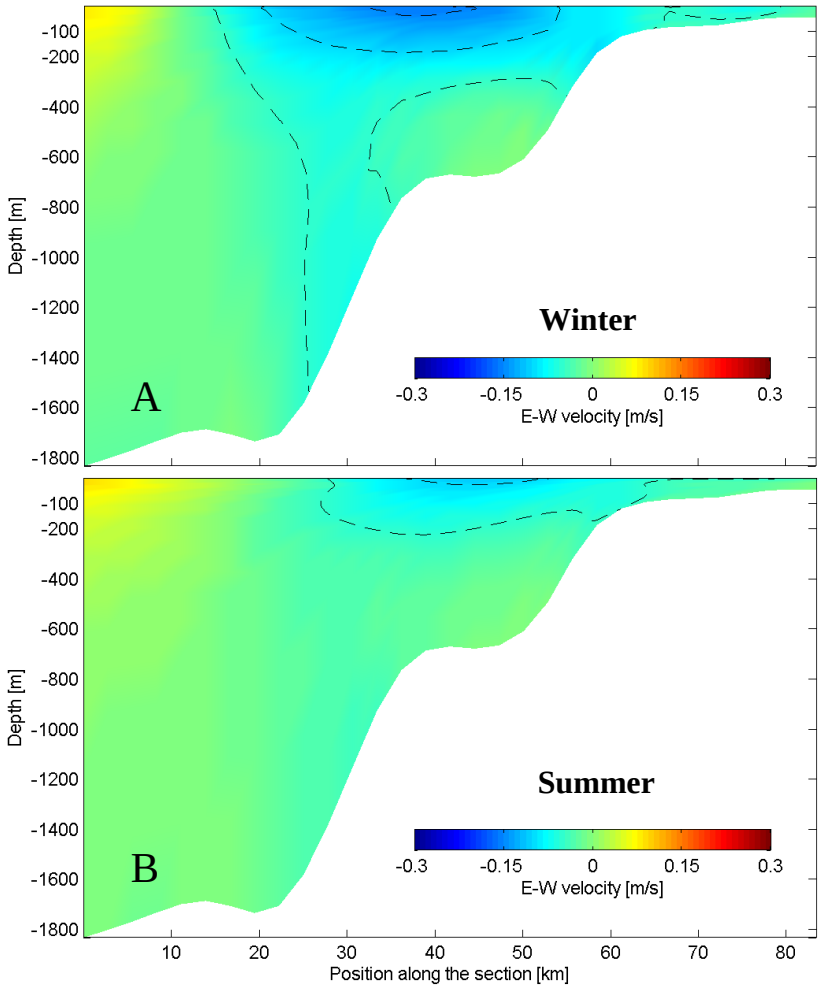

Figure 4.4 (A) winter (January-March) and (B) summer (July-September) mean velocity in the E-W direction taken upstream (at longitude 3°03'E) of the Blanes Canyon.

4.3.4. Meanders and eddies

The NC often develops meanders with a wide range of wavelengths, from a few tens of kilometres to ~100 km (e.g. Millot, 1991; Sammari et al., 1995; Flexas et al., 2002). Anticyclonic eddies propagating along the NC pathways are also frequent (Rubio et al., 2005). Numerical simulations have confirmed the frequent development of mesoscale eddies in the NW Mediterranean (e.g. Echevin et al., 2003; Ahumada and Cruzado, 2007; Rubio et al., 2009; Casella et al., 2011; Schaeffer et al., 2011b). According to our simulation, downstream-propagating meanders and anticyclonic eddies are recurrent in the BC area and produce highly fluctuating three-dimensional circulation patterns within the canyon. An example of these mesoscale features is given to show that NC meanders and anticyclonic eddies can affect the deeper part of the Blanes Canyon (Fig. 4.5). In this case, once the meander reaches the canyon, at the upper layer (Fig. 4.5A), the most onshore part of the current follows the curvature of the

upper canyon, while the main branch turns offshore close to the canyon axis. In spite of these circulation patterns, as a whole the current leaves the canyon through the west (downstream) wall. Although at the deeper layer (Fig. 4.5B), the current is weaker and narrower than at the upper layer, the circulation pattern is very similar. On the other hand, when the anticyclonic eddy is located over the canyon, at the upper layer (Fig. 4.5C), the circulation pattern becomes complex: over the upper canyon the current flows along the canyon walls, while over the lower canyon the current follows an anticyclonic pattern. At the deeper layer (Fig. 4.5D) the circulation pattern is fairly different: at these depths, an anticyclonic circulation dominates a large part of the canyon.

These results are in agreement with observations from oceanographic cruises in the Catalan Sea continental margin, satellite-tracked surface drifters and satellite thermal imagery. For example, Alvarez et al. (1996) observed that the NC over the Palamós Canyon is subjected to significant onshore-offshore displacements in short time-scales. These onshore-offshore displacements were studied numerically by Jordi et al. (2005). The authors point out that before the meander crosses the canyon, the current moves slightly offshore and becomes narrower over the canyon. In contrast, when the meander is located over the canyon, the current begins to move onshore. Associated with this onshore displacement, the current width grows until the meander has completely crossed the canyon. Anticyclonic eddies drifting along the Catalan Sea continental margin have also been reported. Rojas et al. (1995) observed an anticyclonic eddy over the BC shelf-slope. This eddy was associated with a relatively cold fresh water patch located above the seasonal thermocline, which was located at 40 m depth. More recently, Rubio et al. (2005) observed an anticyclonic eddy over the shelfbreak between the Blanes and Palamós canyons. This eddy, of about 45 km in diameter and 100 m depth, modified the local flow, involving advection and subduction of surrounding waters.

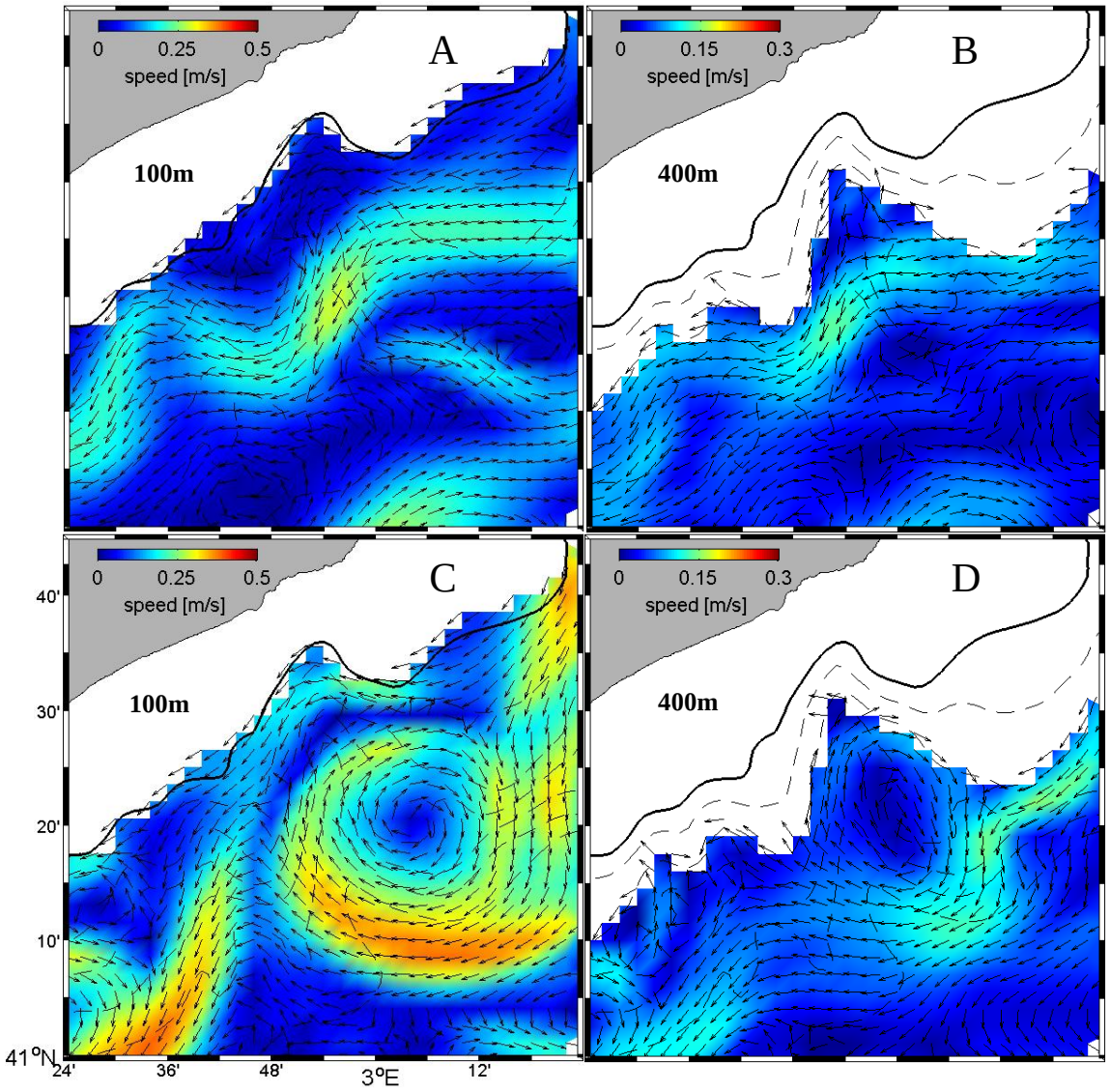

Figure 4.5 Northern Current meander; the fields are snapshots of horizontal velocity taken at 100m (A) and 400m (B) depth in April 27. Anticyclonic eddy propagating along the Northern Current pathways; the fields are snapshots of horizontal velocity taken at 100m (C) and 400m (D) depth in February 15. The arrows indicate the direction of flow. One of every two vectors is shown.

4.3.5. Upwelling/downwelling

Net upwelling/downwelling in submarine canyons has usually been associated with left- and right-bounded flows, respectively. In particular, early observational and numerical studies focused mainly on Astoria Canyon (U.S. West coast) suggest that along-shore wind-driven right-bounded flows produce downwelling inside the canyon, while left-bounded flows create upwelling at the head of the canyon (Hickey, 1995, 1997; Klinck, 1996; She and Klinck, 2000). In the NW Mediterranean Sea, studies focused on submarine canyons suggest that along-slope density-driven right-bounded flows induce downwelling inside the canyons (Blanes Canyon:

Ardhuin et al., 1999; Calvi Canyon: Skliris et al., 2001; and Palamós Canyon: Jordi et al., 2005, 2008). The first two studies also suggest wind-driven upwelling/downwelling depending on the wind direction. Although net downwelling has been recurrently associated with right-bounded flows, recent studies suggest that right-bounded flows can also produce net upwelling. In particular, laboratory experiments indicate upwelling at the shelfbreak decreasing in intensity with depth (Boyer et al., 2006) and field observations show evidence of upwelling at the Blanes Canyon shelfbreak, from about 100 to 200 m depth (Flexas et al., 2008). In spite of these discrepancies, a common result of all the above mentioned studies is that vertical motions (upward/downward) in submarine canyons show significant spatial variability with strong vertical velocities concentrated in small regions of the canyon.

Our simulations indicate that although the NC is a permanent right-bounded (downwelling favourable) flow, both net upwelling/downwelling events take place inside the BC. We found that the meandering of the NC plays a key role in producing these events. An example of the passage of a NC meander over the BC is shown in Fig. 4.6. When the meander reaches the canyon, the horizontal flow is intensified between the upstream wall and the axis of the canyon (Fig. 4.6a, left-upper panel) increasing its negative (anticyclonic) vorticity (Fig. 4.6a, left-lower panel) and leading to strong upward vertical velocities concentrated on the lower canyon (Fig. 4.6a, right-upper panel). Net upwelling is observed from the sea surface to 900 m depth, being maximum around the shelfbreak, that is, from about 150 to 300 m depth (Fig. 4.6a, right-lower panel). In contrast, when the meander is leaving the canyon, the horizontal flow is intensified over the downstream side of the canyon near the coast (Fig. 4.6b, left-upper panel) growing its positive (cyclonic) vorticity (Fig. 4.6b, left-lower panel) and leading to strong downward vertical velocities concentrated around the canyon mouth (Fig. 5.4b, right-upper panel). Net downwelling is observed from below the sea surface to about 750 m depth (Fig. 4.6b, right-lower panel). In this case, maximum downwelling is observed from about 100 to 600 m depth. These results suggest that NC meanders produce an oscillation of the vertical flow characterized by net upwelling when the meander is located over the upstream side of the canyon followed by net downwelling as the meander moves downstream. In absence of meanders and eddies, the general pattern reproduced by the model is downwelling/upwelling on the upstream/downstream upper canyon walls, respectively. However, net vertical fluxes are approximately two orders of magnitude higher (~$1x10^{12}$ $m^3 \cdot d^{-1}$) in presence of a meander than in its absence (~$1x10^{10}$ $m^3 \cdot d^{-1}$).

When considering the annual time series of total net vertical fluxes, larger values (i.e. larger net upwelling/downwelling) are observed in winter with respect to summer (Fig. 4.7a). Net

upwelling/downwelling events have periods ranging from about 4 to 20 days and they are mainly concentrated in winter (Fig. 4.7b). Since the mesoscale activity of the NC is highest in winter and has large vertical extent (e.g. Taupier-Letage and Millot, 1986; Sammari et al., 1995; Flexas et al., 2002), we expect vertical motions during this season to be stronger than during the summer. In our simulations, the stronger (weaker) wind forcing (Fig. 4.7c) in winter (summer) together with weaker (stronger) stratification (Fig. 4.7d) would explain larger (smaller) fluctuations of upwelling/downwelling fluxes inside the canyon.

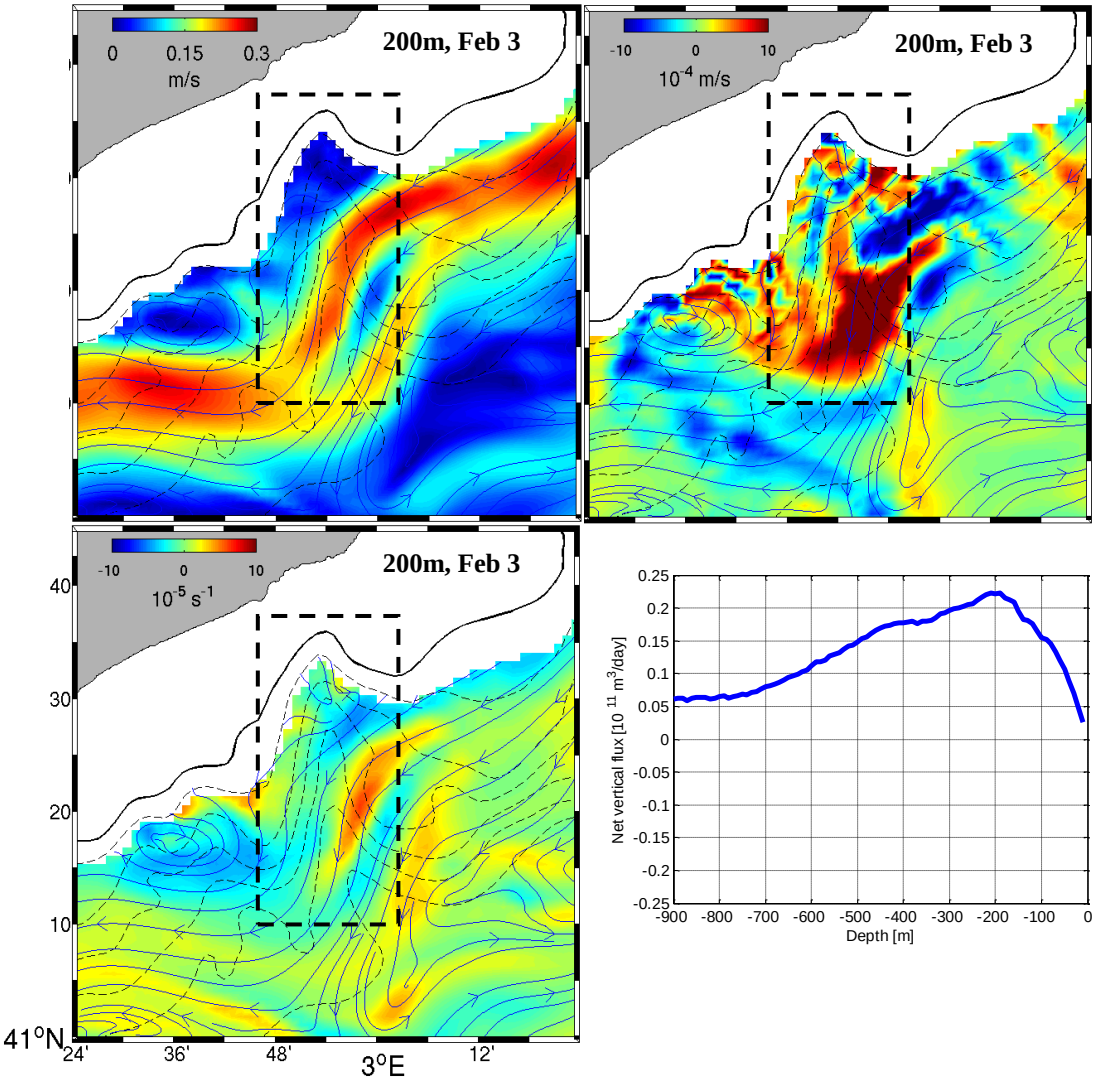

Figure 4.6a Horizontal current speed (left-upper panel), vertical velocity (right-upper panel) and relative vorticity (left-lower panel) at 200m depth with streamlines overplotted. The net vertical flux (right-lower panel) averaged over the rectangle shown in other panels of figure. The fields are snapshots for February 3.

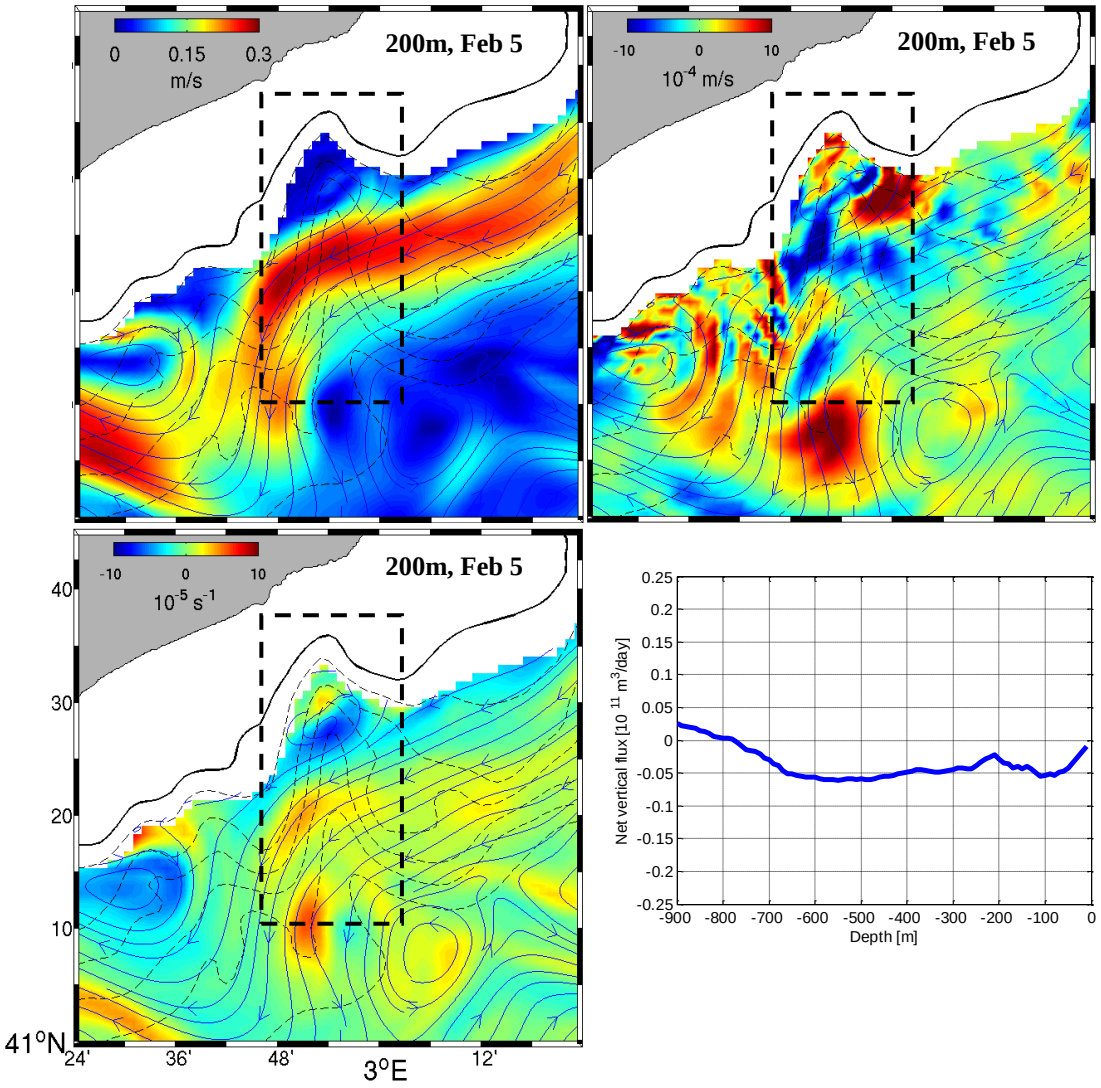

Figure 4.6b Horizontal current speed (left-upper panel), vertical velocity (right-upper panel) and relative vorticity (left-lower panel) at 200m depth with streamlines overplotted. The net vertical flux (right-lower panel) averaged over the rectangle shown in other panels of figure. The fields are snapshots for February 5.

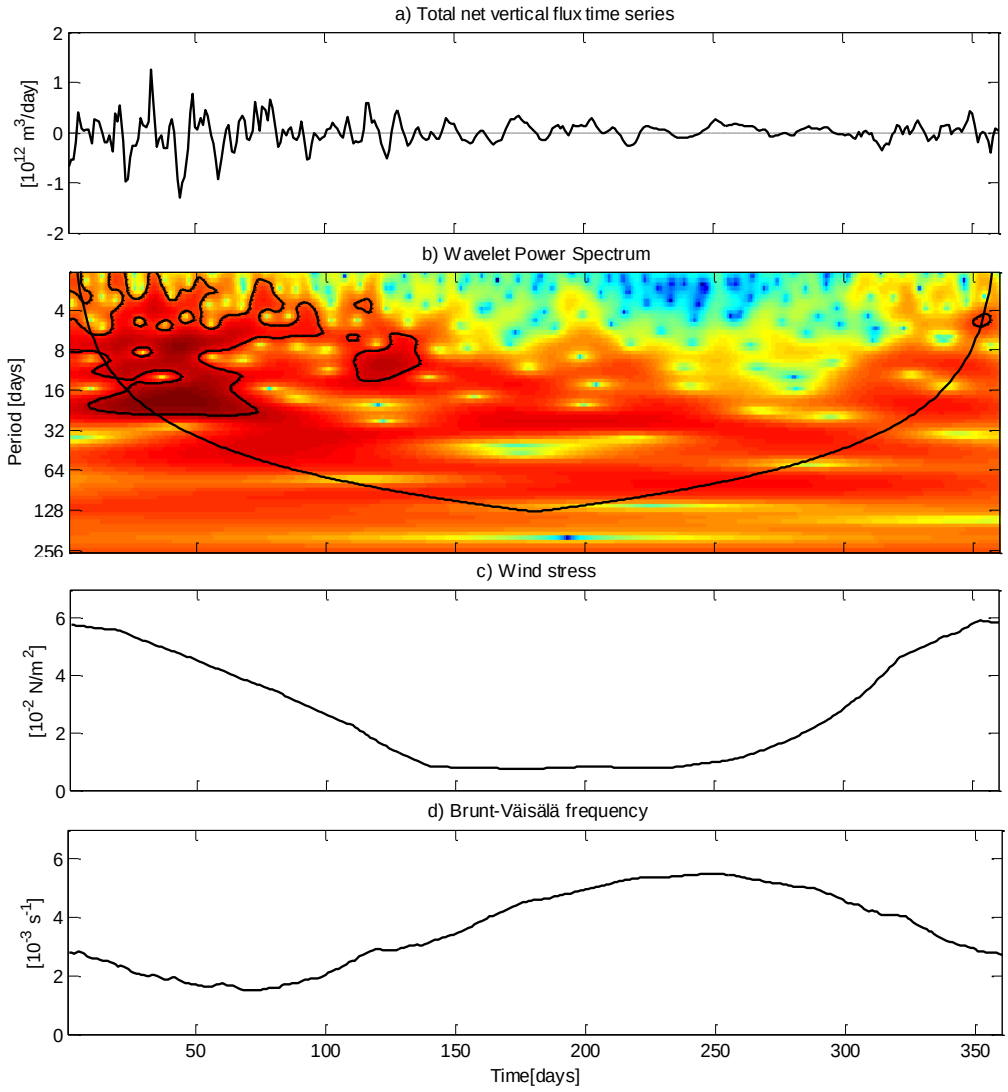

Figure 4.7 (a) Time series of total net vertical flux calculated inside the rectangle (from the sea surface to 900m depth) shown in figure 4.6. (b) Wavelet power spectrum. The shaded contours are at normalized variances of 1. The thick contour encloses regions of greater than 95% confidence for a red-noise process with a lag-1 coefficient of 0.72. The bold line indicates the "cone of influence" where edge effects become important. (c) Wind stress time series. (d) Brunt-Väisälä frequency time series.

4.4. Summary

A high-resolution (~1.2km) 3D circulation model nested in one-way mode to a coarse-resolution (~4km) 3D regional model was used to examine the interaction between the Northern Current (NC) and the Blanes submarine canyon (BC); paying particular attention to upwelling/downwelling events and their seasonal variability. Satisfactory validation of model results with remote sensing and in-situ observations supports the present findings. Model results show that the NC tends to be fast and deep in winter, and slow and shallow in summer. Mesoscale features such as meanders and eddies were recurrent in the BC area and produced

highly fluctuating three-dimensional circulation patterns. In particular, NC meanders and anticyclonic eddies tend to be deep and, consequently, their effects extend down to the deeper part of the canyon. Results also indicate that the meandering of the NC is fundamental in creating net upwelling/downwelling within the canyon. These net upwelling/downwelling events have periods ranging from about 4 to 20 days and they occur most frequently in winter. These findings provide further evidence that continuous downwelling favourable (right-bounded) flows can produce net upwelling inside submarine canyons by showing the importance of NC meanders in creating local net upwelling/downwelling events.

Chapter 5

Shelf-slope exchange in the Blanes submarine canyon

5.1. Introduction

Cross-shelf break exchange is constrained by the tendency of geostrophic flow to follow bathymetric contours. However, small scale topography changes, such as submarine canyons, are regions of enhanced cross-shelf break exchange primarily because they are places of increased Rossby numbers (Allen and Durrieu de Madron, 2009). Large Rossby numbers ($Ro=U/fL$ where U is a characteristic horizontal velocity scale, f is the Coriolis parameter and L is a characteristic horizontal length scale) mean the flow is no longer purely geostrophic and significant cross-isobath flow can occur. In this context, submarine canyons are preferential pathways for cross-shelf break water exchange and particle fluxes. In general, left/right-bounded currents (i.e. with the coastline on the left/right, looking downstream) flowing over submarine canyons induce favourable conditions for water transport and particles fluxes toward the shelf/slope. Left-bounded currents induce nutrient-rich deep-water transport onto the continental shelf and upper-slope contributing to enhanced local biological productivity (e.g. Freeland and Denman, 1982; Skliris and Djenidi, 2006; Kämpf, 2010; Connolly and Hickey, 2014). Right-bounded currents, on the other hand, enhance particle fluxes and upper-slope waters export from the adjacent shelf to the deep basin contributing to the generation of special habitat conditions suitable for the recruitment and maintenance of deep-sea organisms (e.g. Gili et al., 2000; Sardà et al., 2009; De Leo et al., 2010).

In this chapter the objective is to examine the role of the Northern Current and its seasonal variability on the cross-shelf break water exchange, dispersion of passive particles and residence time in the Blanes Canyon. To this purpose, we used the high-resolution (~1.2km) 3D circulation model results and a Lagrangian particle-tracking model.

5.2. Material and methods

5.2.1. Cross-shelf break water exchange

In order to quantify the volume of water exchanged between the continental shelf and slope in the Blanes Canyon (BC), horizontal volume transport was computed across an along-slope vertical section defined by the shelf break (i.e. the 150 m isobath) and its vertical projection to the sea surface. The horizontal limits of this section are the easternmost and westernmost points of the canyon mouth (see Fig. 5.1C). Total volume transport was estimated by integrating the

cross-shelf break velocity across this vertical section. The cross-shelf break velocity at each individual grid point was calculated as the dot product of the velocity vector and the bathymetry gradient (Dinniman et al., 2003):

$$U_{cross} = \overrightarrow{U} \cdot \left(\frac{\nabla H}{|\nabla H|}\right), \quad (5.1)$$

where $\overrightarrow{U}$ is the horizontal velocity vector and H is the bathymetry.

To investigate the relationship between cross-shelf break volume transport and the curvature of the shelf break, we computed the latter as the change along the shelf break of the unit gradient of the bathymetry (Dinniman et al., 2003):

$$\left|\frac{d}{ds}\left(\frac{\nabla H}{|\nabla H|}\right)\right|, \quad (5.2)$$

where s is the distance along the shelf break. The curvature is defined to be negative (positive) when, going from east to west, the shelf break rotates toward the coast (open sea). Since the regional flow is essentially from northeast to southwest, negative (positive) curvature rotates the bathymetry so that momentum advection would tend to drive the flow toward the slope (shelf).

5.2.2 Particle-tracking

To examine the dispersion of passive particles and residence time inside the BC, particle trajectories were calculated using ARIANE (Blanke and Raynaud, 1997), a Lagrangian particle-tracking algorithm that computes offline 3D streamlines from Eulerian circulation model outputs (further details can be found at http://www.univ-brest.fr/lpo/ariane). For the purposes of this study, particle trajectories were computed using the time-varying flow fields produced by the high-resolution (~1.2km) 3D circulation model (see Chapter 4). Between nine and twelve particles were released every day during winter (from January 1 to March 15) and summer (from July 1 to September 15) and tracked for a 15-day period. Particles were released upstream of the BC from the mid-shelf to the upper-slope at depths of 50, 100, 150, 200, 250 and 300 m to investigate how movements of particles vary with different release depths. The residence time defined as the total time spent by a particle within the upper canyon was also computed.

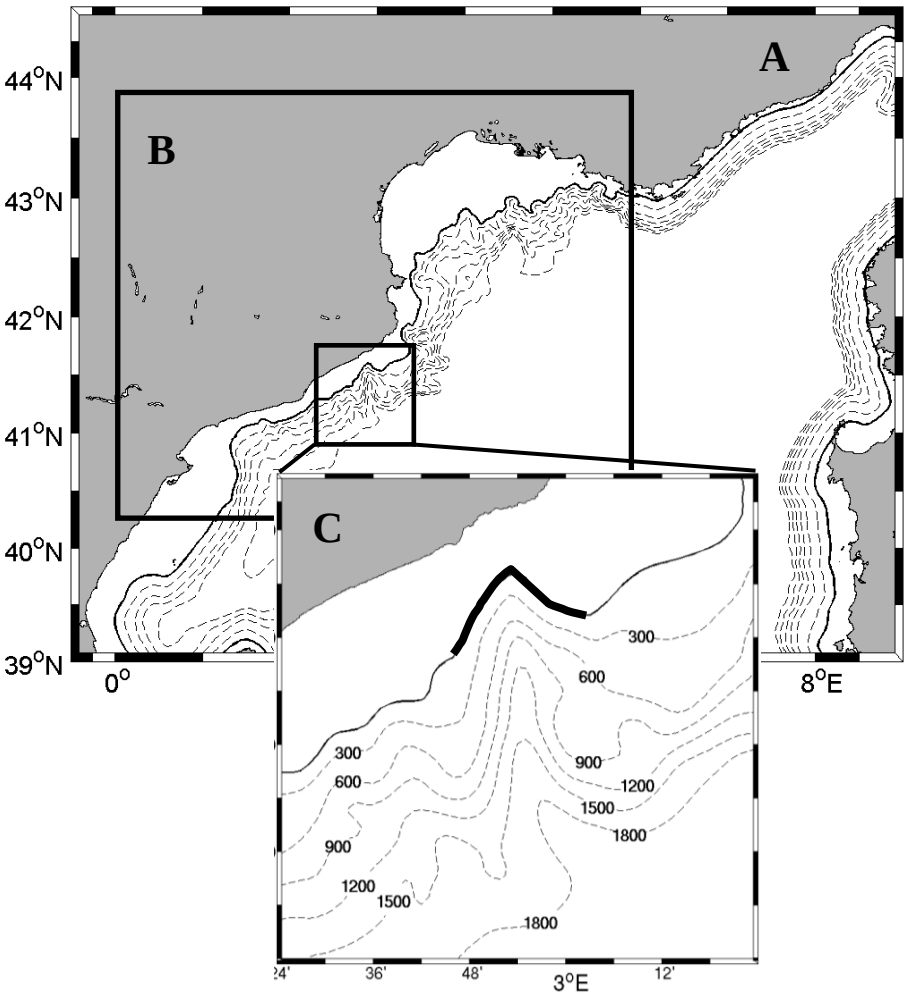

Figure 5.1 Coarse-resolution (~4km) 3D regional model (A) and high-resolution (~1.2km) 3D circulation model (B) domains with the Blanes Canyon subdomain (C). The shelf break from the easternmost point to the westernmost point of the canyon mouth is showing with a thick bold line (further details in the text).

5.3. Results and discussion

5.3.1 Shelf-slope exchange

The cross-shelf break volume transport indicates that water moves predominantly offshore at the eastern (upstream) and onshore at the western (downstream) upper canyon walls, with net volume transport towards the open sea (Fig. 5.2, Table 5.1). As can be seen from the Table 5.1, the amount of water moved across the shelf break at the upstream upper canyon wall represents ~61.6% of the total volume transport. It should be mentioned that the magnitude of the cross-shelf break volume transport is higher in winter (~9.7 Sv) than in summer (~6.9 Sv). It is evident that water exchange between the continental shelf and slope is regulated by flow modifications in the BC. The seasonal-mean depth-averaged horizontal flow (Fig. 5.3) tends to follow the

isobaths; however, as the current enters the canyon it tends to flow across the local isobaths. As a result, even though the onshore edge of the current veers north-westward and then south-westward describing a cyclonic pattern, it crosses the shelf break isobath and therefore water is pushed toward the slope and the shelf at the upstream and downstream upper canyon walls, respectively. Moreover, when the annual mean volume transport as function of position along the shelf break is compared to the curvature of the shelf break (Fig. 5.4), there is a significant correlation ($R=0.88$, $p<0.01$) between volume transport and curvature with the former directed toward the slope when the shelf break rotates toward the coast at the upstream side of the canyon axis and toward the shelf when it rotates toward the open sea at the downstream side.

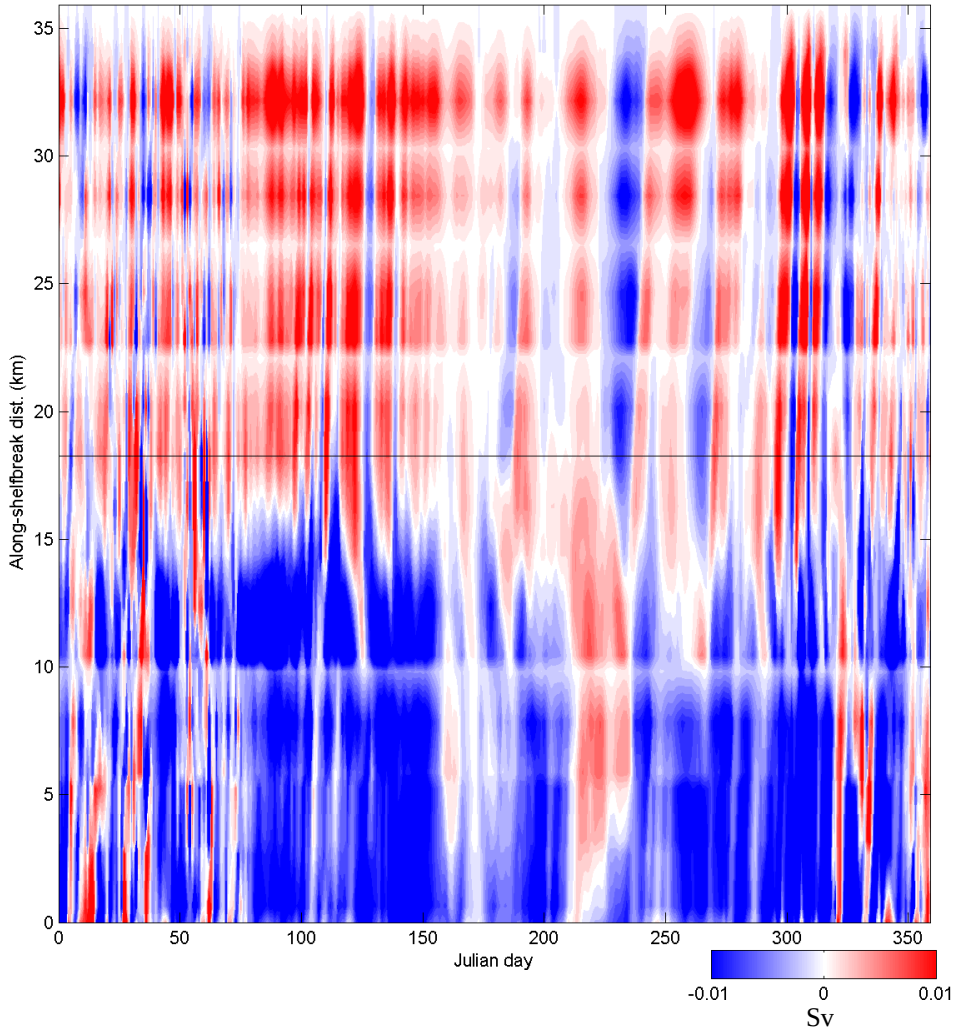

Figure 5.2 Hovmöller diagram of volume transport (in Sv) at each individual grid point along the shelf break. Negative (positive) values indicate volume transport toward the slope (shelf). The along-shelf break distance is the distance following the shelf break from the easternmost point (0km) to the westernmost point (36km) of the Blanes Canyon mouth. Horizontal black line indicates the position of the canyon axis. Below (above) this line is the upstream (downstream) side of the upper canyon walls. See text for further details.

Table 5.1
Volume transports (in Sv) along the shelf break of the Blanes Canyon. Negative (positive) values indicate volume transport toward the slope (shelf).

	Vol. Transp. toward the shelf	Vol. Transp. toward the slope	Net volume transport	Total volume transport
Blanes Canyon (BC)	12.97	-25.51	-12.53	38.49
Eastern (upstream) side of the BC axis	2.24	-21.47	-19.22	23.72
Western (downstream) side of the BC axis	10.73	-4.04	6.69	14.77

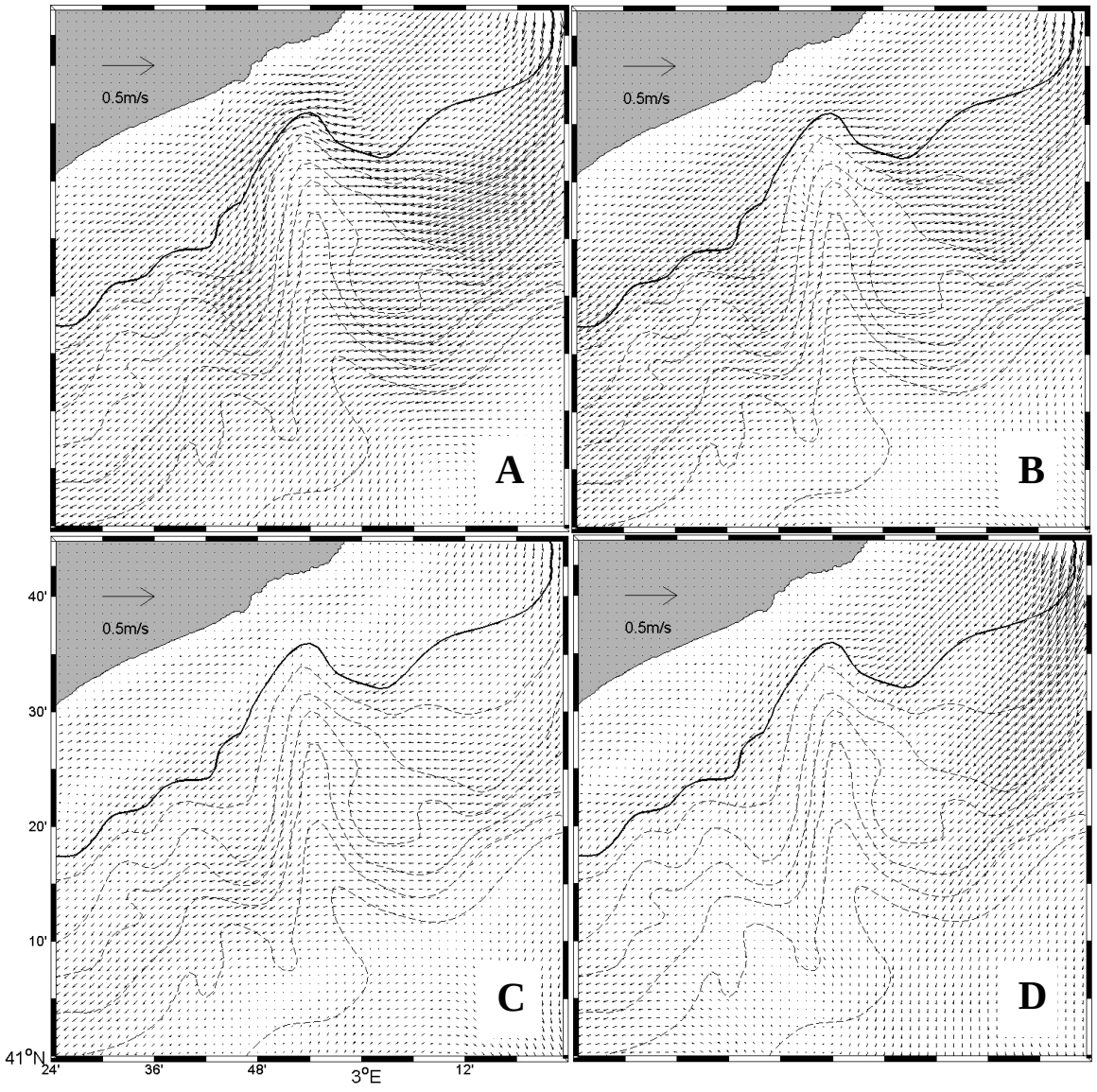

Figure 5.3 Seasonal-mean depth-averaged horizontal flow: (A) winter (January-March), (B) spring (April-June), (C) summer (July-September) and (D) autumn (October-December). The solid contour corresponds to the isobath of 150 m indicating the shelf edge, while the dashed contours correspond to the isobaths of 300, 600, 900, 1200, 1500 and 1800 m. Note that even though the onshore edge of the incident current veers north-westward and then south-westward describing a cyclonic pattern, it crosses the shelf break isobath.

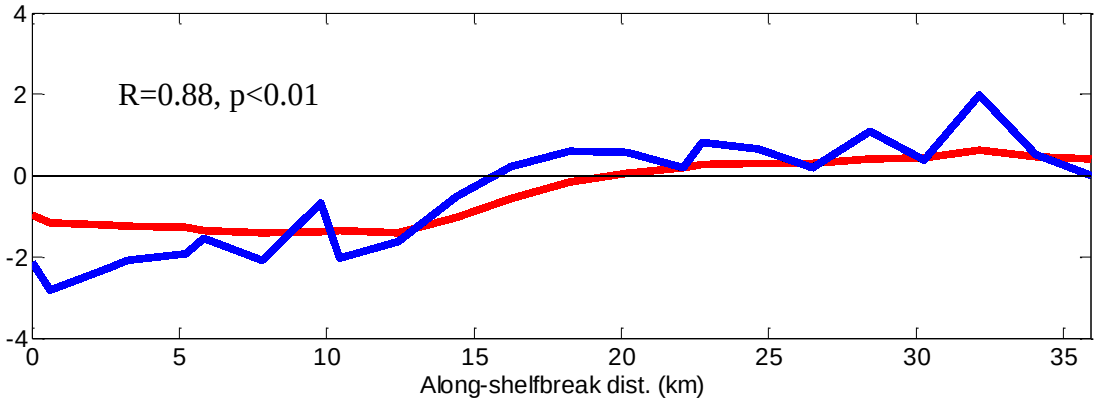

Figure 5.4 Annual mean volume transports (in Sv, blue line) as function of position along the shelf break of the Blanes Canyon. Negative (positive) values indicate volume transport toward the slope (shelf). The curvature of the shelf break (red line) is defined to be negative (positive) when, going from east to west, the shelf break rotates toward the coast (open sea). See text for further details.

5.3.2 Origin of the variability of shelf-slope exchange

According to previous studies, right-bounded currents flowing over submarine canyons are deflected onshore/offshore at the upstream/downstream sides and generally induce favourable conditions for water transport towards the slope (Allen and Durrieu de Madron (2009) and references therein). For example, numerical simulations performed by Klinck (1996) using a Gaussian-shaped canyon with straight isobaths upstream and downstream of the canyon indicate that the magnitude of the exchange in any direction (i.e. onshore/offshore) across the shelf break is about the same and that the increased stratification reduces water exchange by approximately 50%. In contrast, numerical simulations carried out by Skliris et al. (2002) using realistic bathymetry for Calvi Canyon (NW Corsica) show that cross-shelf break water exchange is higher (~27.3%) at the upstream side of the canyon axis. Concerning the role of the stratification, their results are consistent with those of Klinck (1996) showing cross-shelf break water exchange decreasing in strongly stratified conditions. More recently, numerical simulations performed by Jordi et al. (2005) using realistic bathymetry for the nearby Palamós Canyon show enhanced cross-shelf break water exchange, though no values for the upstream/downstream sides of the canyon are provided. Observational evidence from satellite images and seawater properties also suggests significant (though not quantified) cross-shelf break exchange (e.g. Masó et al., 1990; Alvarez et al., 1996; Flexas et al., 2008).

Although, our results, in good agreement with previous studies, show an onshore/offshore deflection of the incident regional flow at the upstream/downstream upper canyon walls, the onshore edge of the incoming current crosses the shelf break isobath and consequently water is

pushed toward the slope/shelf at the upstream/downstream upper canyon walls, respectively. Moreover, the amount of water moved across the shelf break of the upstream upper canyon wall is approximately two times larger than that moved across the shelf break downstream. This preferential zone for cross-shelf break water exchange seems to be related to the asymmetry of the shelf break geometry characterized by a sharp curvature at the upstream upper canyon wall. The high correlation ($R=0.88$, $p<0.01$) found between curvature of the shelf break and cross-shelf break water exchange is consistent with Dinniman et al. (2003) who found significant correlation between curvature of the shelf break and water exchange across the shelf break of the Ross Sea. In addition, a regional study performed by Jordi et al. (2006) shows enhanced cross-shelf break exchange near submarine canyons of the NW Mediterranean Sea. Our results are also in line with previous studies showing cross-shelf break water exchange higher (~30%) in weakly (e.g. winter) than in strongly (e.g. summer) stratified conditions.

5.3.3. Vertical motions

Associated with the location where the incoming current interacts with the shelf break, downwelling and upwelling pools occur at the upstream and downstream upper canyon walls, respectively (Fig. 5.5). Early studies based on numerical simulations predicted an antisymmetrical structure with downwelling/upwelling at the upstream/downstream sides of a Gaussian-shaped canyon in weakly and strongly stratified conditions (see Figs. 2a and 3 in Klinck, 1996). Although numerical simulations using realistic bathymetry for Calvi Canyon (NW Corsica) also show downwelling/upwelling at the upstream/downstream sides of the canyon, the spatial structure is rather different to that predicted by the Klinck's model (see Figs. 7 and 3b in Skliris et al., 2001; 2002, respectively). In contrast to earlier findings, numerical simulations using realistic bathymetry for the nearby Palamós Canyon (see Fig. 5 in Jordi et al., 2005) show more complicated downward/upward vertical flows with extreme downwelling/upwelling near the walls close to the canyon head when the incoming current is located onshore and close to the mouth when it is located further offshore. Observations of water properties over the Blanes Canyon (Flexas et al., 2008) also suggest downwelling/upwelling at the upstream/downstream upper canyon walls as found in the present study.

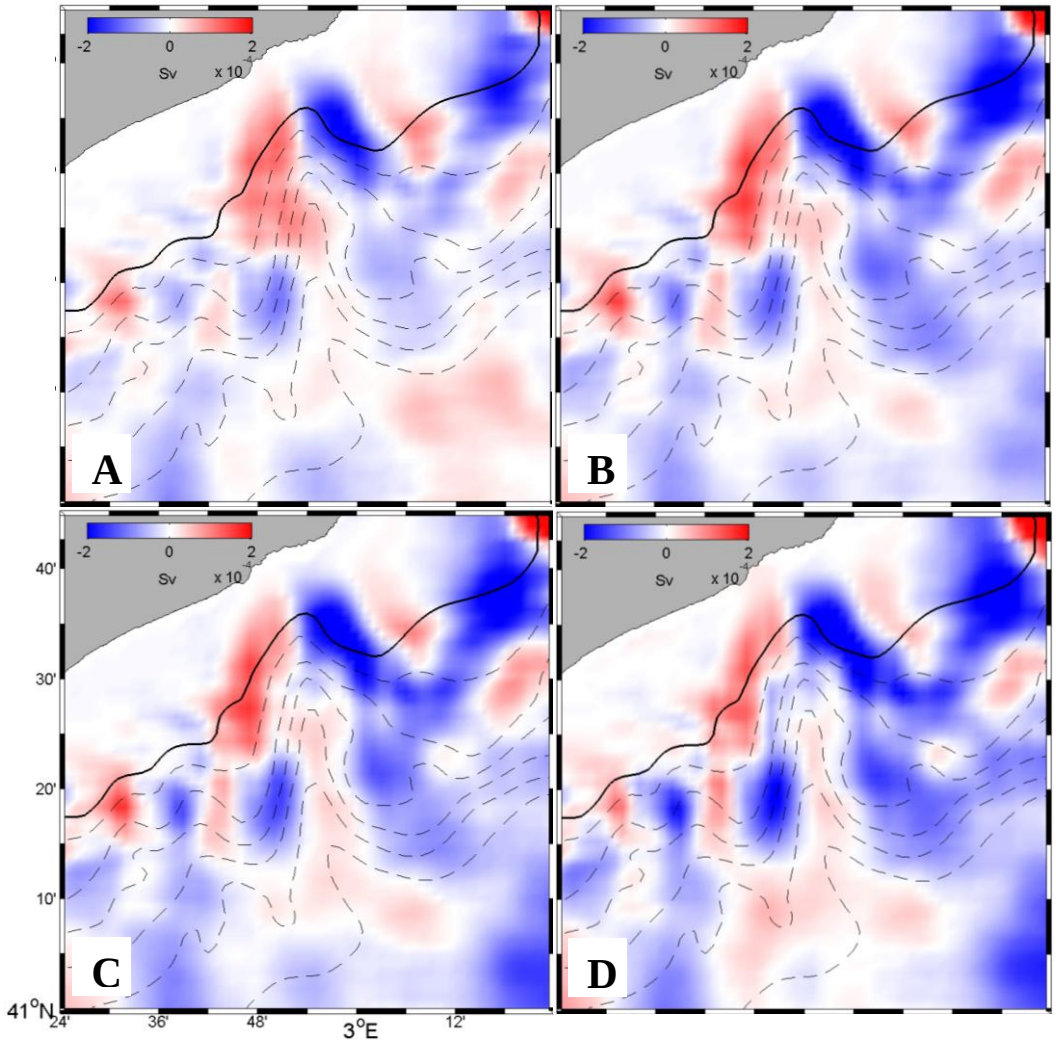

Figure 5.5 Seasonal-mean depth-averaged vertical flow: (A) winter (January-March), (B) spring (April-June), (C) summer (July-September) and (D) autumn (October-December). Positive (negative) values indicate upward (downward) flow. The solid contour corresponds to the isobath of 150 m indicating the shelf edge, while the dashed contours correspond to the isobaths of 300, 600, 900, 1200, 1500 and 1800 m.

5.3.4. Dispersion of passive particles and residence time

Figures 5.6, 5.7 and 5.8 show trajectories of passive particles released upstream BC at different depths. Though particles released at depths of 50 and 100 m (i.e. above the shelf break depth) show a high horizontal dispersion pattern, particles moving over BC tend to concentrate on the upper canyon with a high percentage (greater than 80%) of particles travelling between the sea surface and 200 m depth (Fig. 5.6, Table 5.2). The mean residence time for these particles ranges between ~3.7 and ~4.9 days in winter and summer, respectively (Table 5.3). On the other hand, particles released at the shelf break depth (i.e. at 150 m) and deeper (i.e. at 200, 250 and 300 m) have a notable tendency to concentrate near the shelf edge (Figs. 5.7 and 5.8). As can be seen

from the Figs. 5.7-5.8 and Table 2, particles moving over BC also tend to concentrate on the upper canyon and undergo a net downward movement from their initial release depth, with a depth change (i.e. vertical dispersion) greater in winter than in summer. It should be noted that a small percentage (less than 5%) of particles released below the shelf break reach the upper 100 m of the water column. The mean residence time for particles released at the shelf break depth and below ranges between ~4 and ~5.8 days in winter and summer, respectively (Table 5.3).

Particles fluxes to the deep continental margin and basin of the NW Mediterranean Sea are directly determined by margin's physiography, atmospheric conditions, the NC and event-driven oceanographic processes (i.e. dense shelf water cascading, offshore convection and eastern storms), and inputs of allochthonous and autochthonous materials, altogether forming the set of abiotic factors controlling the ecosystem (Canals et al., 2013).

Submarine canyons in the NW Mediterranean Sea are places where intense exchange between the continental shelf and deep environments occur. Observational studies reveal clear differences in the amount of settling particles in canyon and slope environments. For example, particle fluxes within BC are higher (almost one order of magnitude) than the fluxes recorded in the neighbouring open slope at the same depths (Zuñiga et al., 2009; Sanchez-Vidal et al., 2012; Lopez-Fernandez et al., 2013).

In agreement with these studies, our results show a net particle downward transport within the upper canyon. The BC appears to enhance particle export by funnelling to the slope particles that are carried within the upper canyon by the NC. The NW Mediterranean is considered a mesothropic area with an intense phytoplankton bloom occurring between late winter and early spring (cf. Bosc et al., 2004). During this period the NC and associated meanders and eddies carry large amounts of organic matter (both particulate and dissolved) that can undergo downward movement as a consequence of the interaction with the BC. Furthermore, the NW Mediterranean spring bloom often develops when the water column is still weakly stratified (Bernardello et al., 2012) which, according to our results, is the condition under which vertical particle dispersion within the canyon is highest.

On the other hand, studies focused on the distribution of fish eggs and larvae in the Catalan Sea have reported high larval concentrations over the shelf edge, which was linked with the presence of the shelf/slope front and its associated current (i.e. the NC) (Sabatés et al., 2007). The authors point out that this pattern is subject to significant spatio-temporal variability due to mesoscale variability, namely frontal oscillations (i.e. meanders) and anticyclonic eddies. Moreover, a

recent study of crustacean larvae carried out in the BC area show high larval concentrations following the shelf edge (N. Bahamon *com. pers.*). Accordingly, our Lagrangian particle-tracking experiments show that passive particles released from the mid-shelf to upper-slope drift along the shelf edge with higher dispersion in winter than in summer, which is likely associated with weakly stratified conditions but also with the recurrent passage of NC meanders and eddies (see Chapter 4). Our findings also indicate increasing particle residence time with depth. Particles travelling at depths greater than the canyon rim (i.e. below 100 m depth) have longer residence times within the canyon.

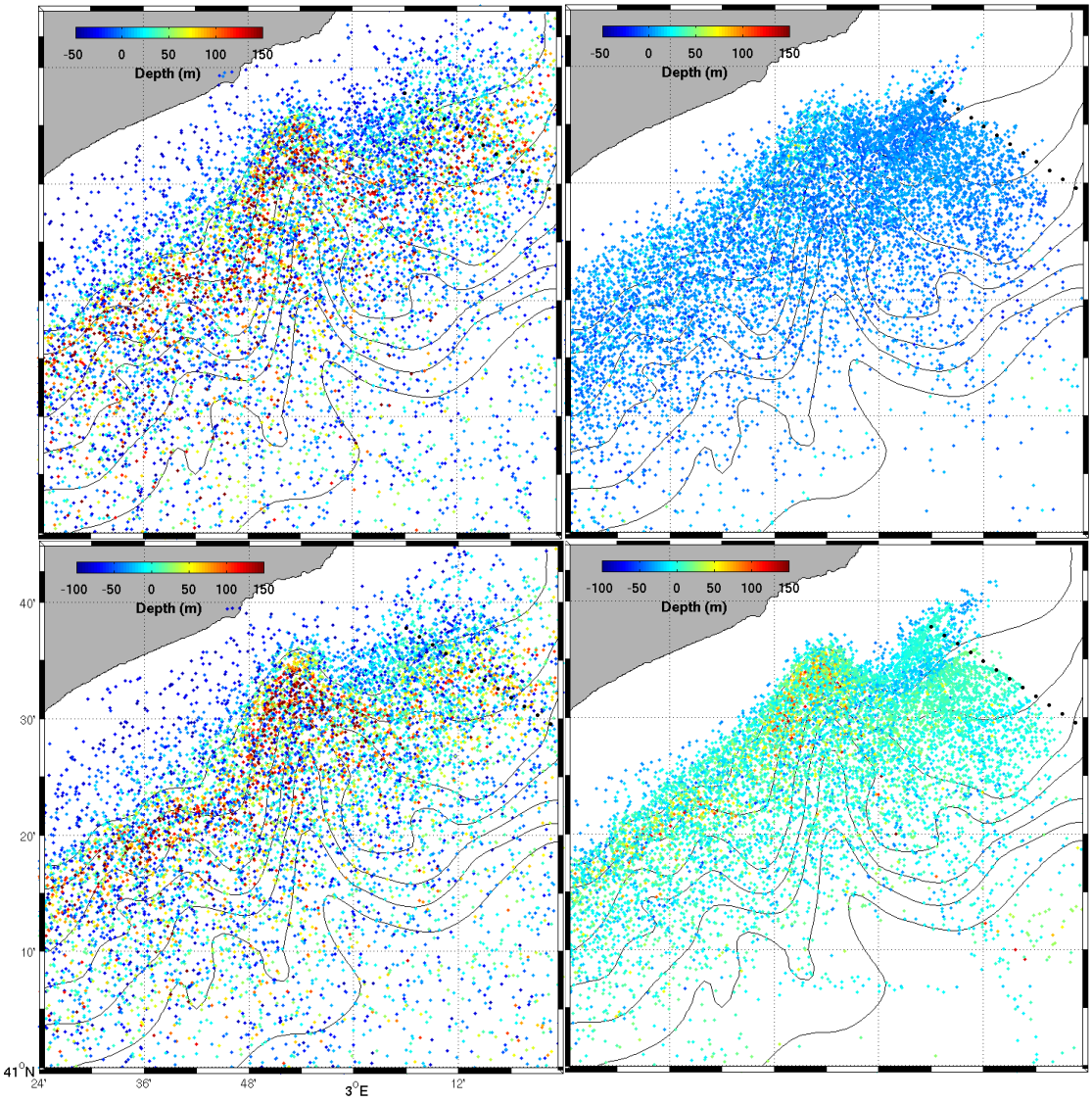

Figure 5.6 Distribution of passive particles released upstream Blanes Canyon at depths of 50 m (**winter**: left-upper panel, **summer**: right-upper panel) and 100 m (**winter**: left-lower panel, **summer**: right-lower panel). Particle initial positions are indicated by black circles. Color bar indicates depth change from the initial release depth. Contours correspond to the isobaths of 150 (shelfbreak depth), 300, 600, 900, 1200, 1500 and 1800 m.

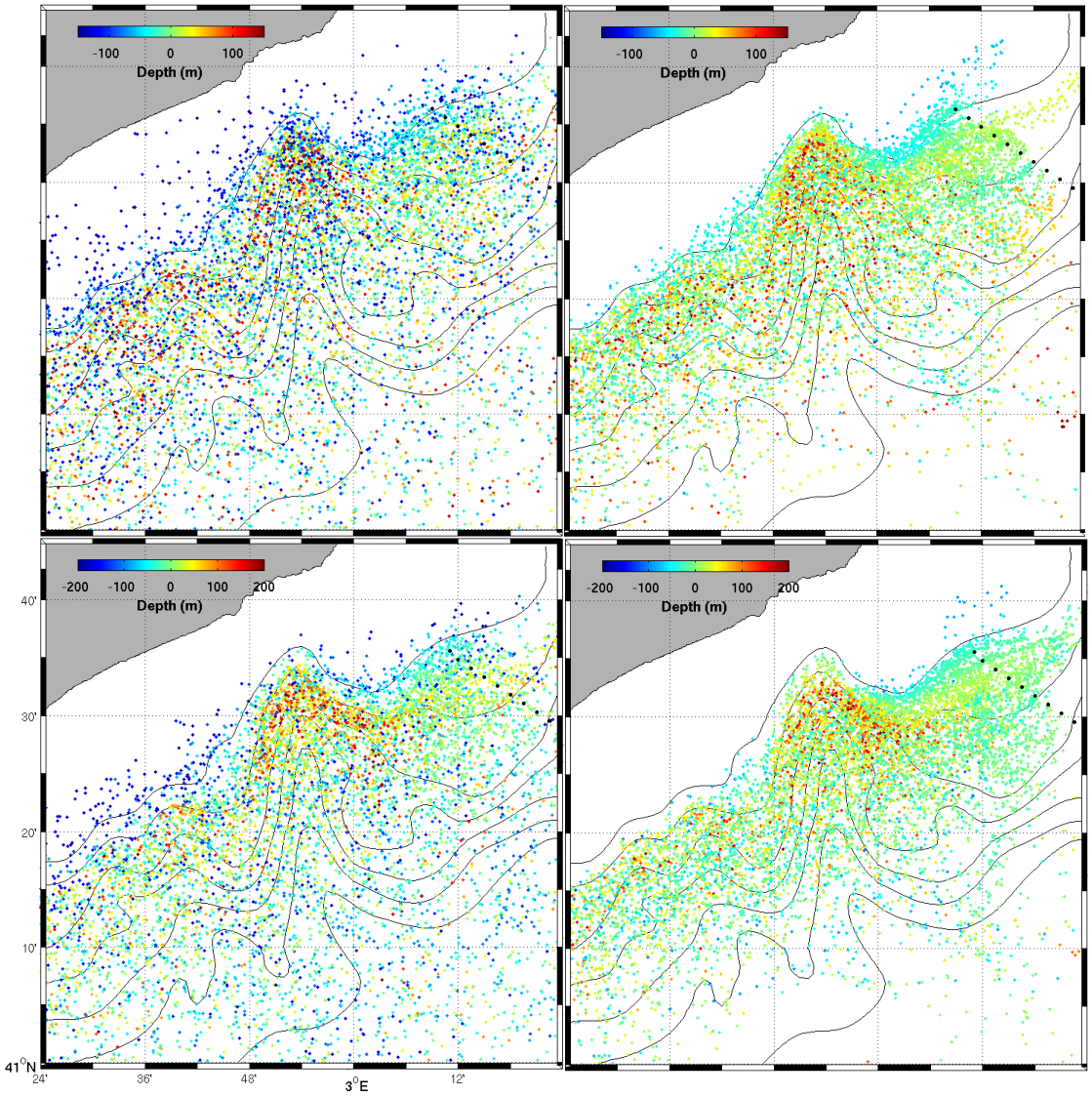

Figure 5.7 Distribution of passive particles released upstream Blanes Canyon at depths of 150 m (**winter**: left-upper panel, **summer**: right-upper panel) and 200 m (**winter**: left-lower panel, **summer**: right-lower panel). Particle initial positions are indicated by black circles. Color bar indicates depth change from the initial release depth. Contours correspond to the isobaths of 150 (shelfbreak depth), 300, 600, 900, 1200, 1500 and 1800 m.

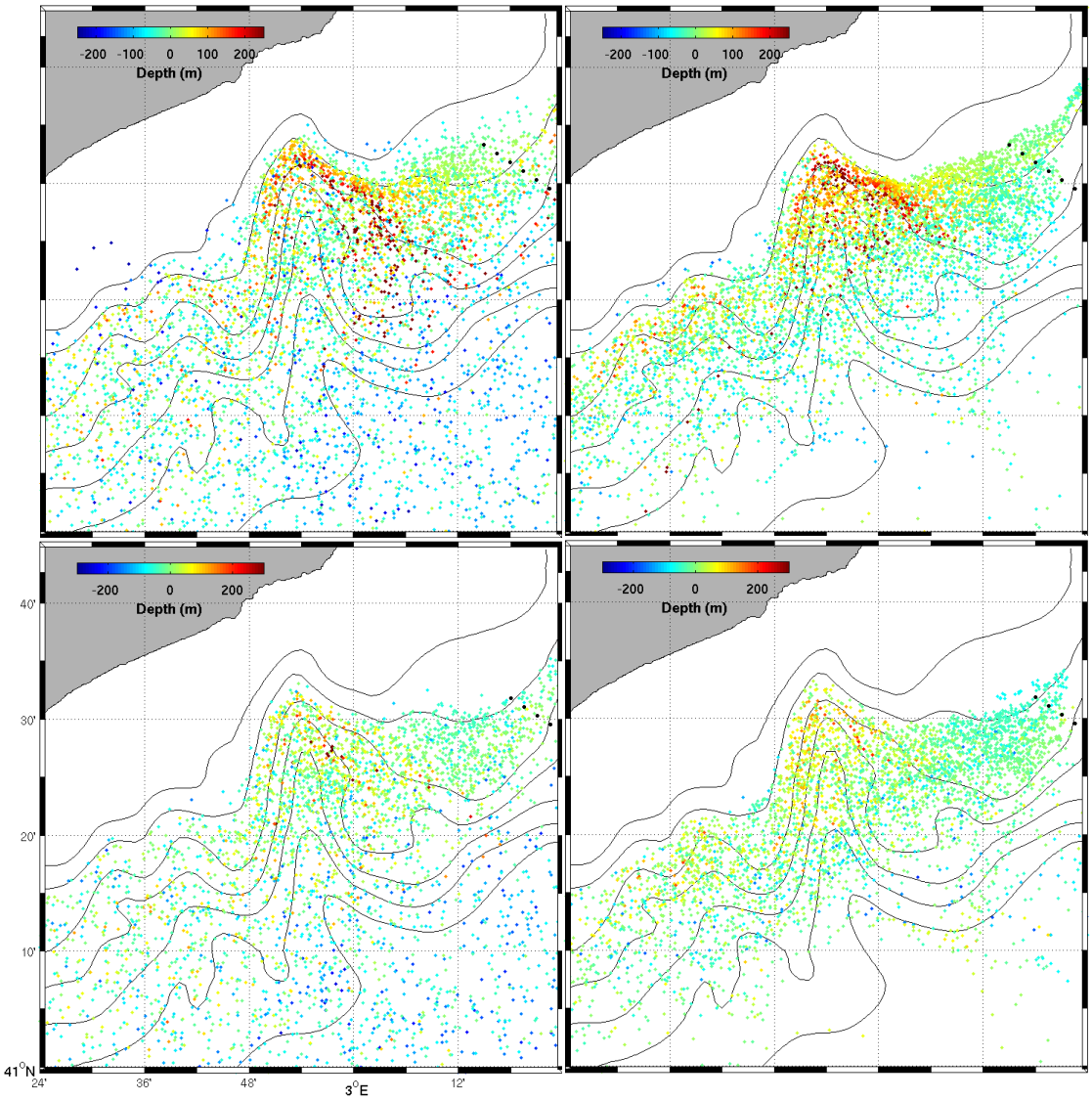

Figure 5.8 Distribution of passive particles released upstream Blanes Canyon at depths of 250 m (**winter**: left-upper panel, **summer**: right-upper panel) and 300 m (**winter**: left-lower panel, **summer**: right-lower panel). Particle initial positions are indicated by black circles. Color bar indicates depth change from the initial release depth. Contours correspond to the isobaths of 150 (shelfbreak depth), 300, 600, 900, 1200, 1500 and 1800 m.

Table 5.2
Percentage of passive particles at different depth ranges within the upper Blanes Canyon

Depth of origin	Season	Depth ranges (m)											
		0-50	50-100	100-150	150-200	200-250	250-300	300-350	350-400	400-450	450-500	500-550	550-600
50 m	Winter	**35.73**	**32.15**	**17.31**	**8.94**	3.05	1.52	1.0	0.26	0.0	0.0	0.0	0.0
	Summer	**49.54**	**49.57**	0.87	0.0	0.0	0.0	0.0	0.0	0.0	0.0	0.0	0.0
100 m	Winter	**22.65**	**28.85**	**23.40**	**11.94**	7.78	2.97	1.43	0.34	0.29	0.14	0.14	0.0
	Summer	0.43	**43.76**	**45.36**	**8.58**	1.26	0.46	0.12	0.0	0.0	0.0	0.0	0.0
150 m	Winter	**21.66**	**16.52**	**20.94**	**22.84**	**11.93**	4.03	1.34	0.71	0.0	0.0	0.0	0.0
	Summer	0.0	2.37	**33.72**	**39.45**	**17.67**	5.40	1.13	0.21	0.0	0.0	0.0	0.0
200 m	Winter	4.82	4.88	**9.97**	**21.36**	**24.98**	**21.16**	**8.10**	3.34	1.20	0.13	0.0	0.0
	Summer	0.0	0.49	5.01	**27.70**	**32.86**	**18.27**	**10.07**	3.97	1.29	0.29	0.0	0.0
250 m	Winter	0.81	0.58	2.67	**10.22**	**21.71**	**18.00**	**20.55**	**11.26**	6.73	2.67	1.62	1.27
	Summer	0.0	0.0	0.25	3.92	**12.69**	**21.72**	**23.05**	**18.37**	**8.85**	4.01	2.84	2.42
300 m	Winter	0.0	0.0	0.40	2.21	**11.26**	**26.76**	**33.19**	**14.88**	6.63	2.41	0.40	0.0
	Summer	0.0	0.0	0.0	0.75	2.07	**24.90**	**37.92**	**21.69**	**9.43**	2.64	0.56	0.0

Table 5.3
Mean residence time plus/minus the standard deviation (days) of passive particles within the upper Blanes Canyon

Depth of origin	Season	
	Winter	Summer
50 m	3.78 (±3.1)	4.36 (±2.8)
100 m	3.92 (±3.0)	4.97 (±2.7)
150 m	4.06 (±3.1)	5.12 (±3.0)
200 m	4.29 (±3.2)	5.56 (±3.0)
250 m	4.61 (±3.0)	5.78 (±2.9)
300 m	5.40 (±3.5)	5.80 (±2.8)

5.4. Summary

A high-resolution (~1.2km) 3D circulation model nested in one-way to a coarse-resolution (~4km) 3D regional model was used to examine the cross-shelf break water exchange in the Blanes Canyon. Dispersion of passive particles and residence time were also examined with a Lagrangian particle-tracking model coupled to the high-resolution 3D circulation model. Results show that the onshore edge of the Northern Current (NC) crosses the shelf break isobath and as a result water is pushed toward the slope and shelf at the upstream and downstream upper canyon walls, respectively. Importantly, the amount of water that crosses the shelf break at the upstream upper canyon wall is approximately twice as large as the amount of water moved downstream. Accordingly, associated with the location where the NC interacts with the shelf break,

downwelling and upwelling pools occur at the upstream and downstream upper canyon walls, respectively. A sharp curvature of the shelf break at the upstream upper canyon wall is related to this preferential pathway for cross-shelf break water exchange. In general, there is a significant correlation ($R=0.88$, $p<0.01$) between the curvature of the shelf break and water exchange across the shelf break of the canyon. Water transport is higher (~30%) in winter than in summer. In agreement with these findings, our Lagrangian particle-tracking experiment shows that passive particles released from the mid-shelf to the upper-slope drift along the shelf edge with a net downward movement within the upper canyon. Further results show that particle dispersion is higher in winter than in summer. Our results also point to a general increase of residence time with depth, with particles travelling below the canyon rim (i.e. below 100m) having longer residence times within the canyon.

Chapter 6

Conclusions and future research

A high-resolution (~1.2km) 3D circulation model nested in one-way to a coarse-resolution (~4km) 3D regional model was used to examine the Northern Current (NC) and its interaction with the Blanes submarine canyon (BC); paying particular attention to upwelling/downwelling events and cross-shelf break water exchange. Although it refers to a climatological simulation, at this resolution, the Rossby radius of deformation for the Mediterranean Sea (5-12 km) is resolved. Therefore the model properly suites our purpose, since it adequately reproduces the NC mesoscale variability and its seasonality. Satisfactory validation of model results with remote sensing and in-situ observations supports the present findings. A Lagrangian particle-tracking model coupled to the high-resolution 3D circulation model was also used to examine the role of the NC and its seasonal variability on the dispersion of passive particles and residence time within the canyon.

6.1. Conclusions

- The NC tends to be fast and deep in winter, and slow and shallow in summer.

- Mesoscale features such as meanders and eddies are recurrent in the BC area and produce highly fluctuating three-dimensional circulation patterns. NC meanders and anticyclonic eddies tend to be deep and, consequently, their effects extend down to the deeper part of the canyon.

- Upwelling/downwelling events occurring on timescales of 4 to 20 days are associated with NC meanders passing over the BC.

- NC meanders produce an oscillation of the vertical flow characterized by net upwelling when the meander is located over the upstream side of the canyon followed by net downwelling as the meander moves downstream.

- Net vertical fluxes are approximately two orders of magnitude higher in the presence of a meander than in its absence.

- Upwelling/downwelling events are also influenced by the NC seasonality. They are more predominant in winter than in summer.

- Associated with the location where the NC interacts with the shelf break, downwelling and upwelling pools occur at the upstream and downstream upper canyon walls, respectively.

- Cross-shelf break water exchange in the BC is predominantly towards the open sea.

- There is a significant correlation between water exchange and the curvature of the shelf break in the BC. The amount of water moved across the shelf break at the upstream upper canyon wall is approximately two times larger than the amount of water moved downstream.

- Cross-shelf break water exchange is higher in winter than in summer.

- Passive particles released from the mid-shelf to the upper-slope drift along the shelf edge with a net downward movement within the upper canyon.

- Particle dispersion is higher in winter than in summer.

- There is a general increase of particle residence time with depth. Particles travelling at depths greater than the BC rim have longer residence times within the canyon**.**

6.2. Future research

Results presented in this thesis show that the Northern Current-Blanes Canyon interaction induces significant vertical motions and water exchange in the shelf/slope region. However, a more complete understanding of these topics could be obtained by means of the use of bathymetric, oceanographic, and meteorological datasets with higher resolutions than those used here. Further research needs to be done to establish the impact of the interannual and long-term variability. More research is also needed to better understand energy conversion budgets (e.g. Marchesiello et al., 2003; Halo et al., 2014) from mean kinetic energy into eddy baroclinic and/or barotropic components. A future development would be the coupling of a biogeochemical model (e.g. Bernardello et al., 2012) to the high-resolution 3D circulation model to quantitatively evaluate the role of the Blanes Canyon as a hotspot for organic matter export to the deep sea. In

fact a realistic evaluation of the export needs to take into account the non-conservative nature of organic matter and would allow to better understand the marine ecosystem structure and functioning in this area. Coupling a Lagrangian particle-tracking model to the high-resolution 3D circulation model will allow assessing the larval connectivity patterns of a number of commercial (and non commercial) species such as red shrimp, among others. The impact of future climate scenarios on mesoscale circulation and the effects on species connectivity and population dynamics of fisheries could also be investigated by coupling the Lagrangian model.

Appendix

Bulk formulas

The surface boundary conditions are specified in order to appropriately reproduce the momentum, heat and mass fluxes between the atmosphere and the sea. Once the raw atmospheric data are interpolated to the resolution of the model, they become the input of the air-sea coupling scheme which is the set of classical bulk formulas used to represent the air-sea boundary processes. As a common feature in the parameterizations of momentum, heat and mass fluxes, the air-sea coupling scheme allows one-way feedback mechanisms to take place. This means that the atmospheric model is not influenced by the hydrodynamic model while the latter is let free to adjust some processes (i.e. turbulent heat fluxes) according to its own surface temperature. The way atmospheric variables are treated to reproduce momentum, heat and mass fluxes at the air-sea boundary is described below.

Momentum flux

The **vertical transfer of horizontal momentum** from the atmosphere to the ocean due to wind stress, τ (N/m^2), is given by:

$$\tau_x = \rho_a C_D |\vec{W}_{10}| W_x \qquad \text{(A.1a)}$$

$$\tau_y = \rho_a C_D |\vec{W}_{10}| W_y \qquad \text{(A.1b)}$$

where W_x and W_y are the wind speed components at 10 m above the sea surface, ρ_a is the density of the air, C_D is the drag coefficient which is calculated as a function of the wind speed and the air-sea temperature difference through a polynomial approximation (Hellerman and Rosenstein, 1983).

Heat fluxes

The **net heat flux** (Q_T) at the sea surface is computed using the following equation:

$$Q_T = Q_{SW} + Q_{LW} + Q_S + Q_L \qquad \text{(A.2)}$$

where Q_{SW} is the net shortwave radiation, Q_{LW} is the net longwave radiation, Q_S is the sensible heat flux, and Q_L is latent heat flux. All terms in Eq. A.2 are in W/m^2.

The **net short wave radiation** is the largest term of the heat budget of the ocean. The calculation of Q_{SW} at the sea surface is based on Reed formula (Reed, 1977):

$$Q_{SW} = Q_{ST}(1 - 0.62C + 0.0019\beta)(1 - \alpha) \qquad \text{(A.3)}$$

where Q_{ST} is the total solar radiation reaching the sea surface under clear sky, C is the total cloud cover (tenths), β is the solar noon altitude in degrees and α is the sea surface Albedo computed as a function of the sun zenith angle (Payne, 1972). Since this formula could overestimate Q_{SW} for low cloudiness values (Reed, 1977), the upper limit for Q_{SW} is imposed to be Q_{ST} (Castellari et al., 1998). The total solar radiation Q_{ST} is represented by its components Q_{dir} (direct solar radiation) and Q_{dif} (downward diffuse sky radiation) (Rosati and Miyakoda, 1988):

$$Q_{ST} = Q_{dir} + Q_{dif} = Q_0 \tau^{\sec(z)} + \frac{\left[(1 - A_0)Q_0 - Q_0 \tau^{\sec(z)}\right]}{2} \quad \text{(A.4)}$$

where the solar radiation at the top of the atmosphere Q_0 has been calculated as a function of latitude-longitude and time using astronomical parameters from the *Smithsonian Meteorological Tables*. The parameter τ (=0.7) represents the atmospheric transmission coefficient, A_0 is the water vapour plus ozone absorption (=0.09) and z is the zenith angle in degrees.

The **net longwave radiation** (Q_{LW}) is computed using the Bignami formula (Bignami et al., 1995). This formula has been obtained with a statistical regression method on experimental data obtained in the western Mediterranean during different seasons:

$$Q_{LW} = \varepsilon\sigma T^4 - \left[\sigma T_{air}^4 (0.653 + 0.00535 e_A)\right](1 + 0.1762 C^2) \quad \text{(A.5)}$$

where ε is the ocean emissivity (=0.97), σ is the Stefan-Boltzman constant (=5.67x10^{-8} kg·s^{-3}·K^{-4}), T is the sea surface temperature obtained from the model, e_A (mbar) is the atmospheric vapor pressure:

$$e_A = rh \cdot e_{sat}(T_{air}) \quad \text{(A.6)}$$

where rh (%) is the relative humidity, $e_{sat}(T_{air})$ (mbar) is the atmospheric saturation vapor pressure, computed through a polynomial approximation as a function of air temperature.

The saturation vapor pressure over liquid water, e_s, at temperature T (°C) is obtained from the Bolton formula (Bolton, 1980):

$$e_s(T) = 6.112 e^{\left(\frac{17.67T}{T+243.5}\right)} \quad \text{(A.7)}$$

The **sensible** (Q_S) and **latent** (Q_L) **heat** terms are computed using:

$$Q_S = \rho_A C_p C_H \left|\vec{W}_{10}\right|(T - T_{air}) \quad \text{(A.8)}$$

$$Q_L = \rho_A L_E C_E |\vec{W}_{10}| [e_{sat}(T) - rh \cdot e_{sat}(T_{air})] \frac{0.622}{P_{atm}} \quad \text{(A.9)}$$

where is the density of moist air calculated as a function of air temperature and relative humidity, C_p is the specific heat capacity of air (1005 $J \cdot kg^{-1} \cdot K^{-1}$), L_E ($J \cdot kg^{-1}$) is the latent heat of vaporization calculated as a function of sea surface temperature (see below). The turbulent exchange coefficients C_H and C_E are estimated in terms of air-sea temperature difference and the wind speed taking into account an atmospheric stability index (Kondo, 1975).

Mass fluxes

The freshwater mass flux, *WF* (m/s), and the associated salt flux, *SF* (kg/m^2s), at the sea surface are obtained from the difference between evaporation and precipitation (*E-P*):

$$WF = (E/\rho_{sw}) - P \quad \text{(A.10a)}$$

$$SF = (E - P) * (S_{inp} - S) \quad \text{(A.10b)}$$

where ρ_{sw} is the density of the seawater, *S* is the sea surface salinity from the model and S_{inp} is the salinity of water exchanged between the air and the sea (set to zero). The evaporation rate, *E* (kg/m^2s), is calculated from the latent heat flux, Q_L, and the latent heat of vaporization, L_E, using (Gill, 1982):

$$E = \frac{Q_L}{L_E} \quad \text{(A.11)}$$

References

Ahumada, M.A., Cruzado, A., 2007. Modeling of the circulation in the Northwestern Mediterranean Sea with the Princeton Ocean Model. *Ocean Science* 3, 77-89.

Allen, S.E., Durrieu de Madron, X., 2009. A review of the role of submarine canyons in deep-ocean exchange with the shelf. *Ocean Science* 5, 607-620.

Allen, S.E., Hickey, B.M., 2010. Dynamics of advection-driven upwelling over a shelf break submarine canyon. *Journal of Geophysical Research* 115, C08018.

Alvarez, A., Tintoré, J., Sabatés, A., 1996. Flow modification and shelf-slope exchange induced by a submarine canyon off the northeast Spanish coast. *Journal of Geophysical Research* 101(C5), 12043-12055.

Amblas, D., Canals, M., Urgeles, R., Lastras, G., Liquete, C., Hughes-Clarke, J.E., Casamor, J.L., Calafat, A.M., 2006. Morphogenetic mesoscale analysis of the northeastern Iberian margin, NW Mediterranean Basin. *Marine Geology* 234, 3-20.

Apel, J.R., 1987. Principles of Ocean Physics. International Geophysical Series, 38. Academic Press, London, 634 p.

Arabelos, D.N., Papazachariou, D.Z., Contadakis, M.E., Spatalas, S.D., 2011. A new tide model for the Mediterranean Sea based on altimetry and tide gauge assimilation. *Ocean Science* 7, 429-444.

Ardhuin, F., Pinot, J.M., Tintoré, J., 1999. Numerical study of the circulation in a steep canyon off the Catalan coast (western Mediterranean). *Journal of Geophysical Research* 104(C5), 11115-11135.

Astraldi, M., Gasparini, G.P., Sparnocchia, S., 1994. The seasonal and interannual variability in the Ligurian-Provencal Basin. *Coastal Estuarine Studies* 46, 93-113.

Bahamon, N., Aguzzi, J., Bernardello, R., Ahumada-Sempoal, M.A., Puigdefabregas, J., Cateura, J., Muñoz, E., Velásquez, Z., Cruzado, A., 2011. The new pelagic Operational Observatory of the Catalan Sea (OOCS) for the multisensor coordinated measurement of atmospheric and oceanographic conditions. *Sensors* 11, 11251-11272.

Barnier, B., Marchesiello, P., Pimenta De Miranda, A., Molines, J.-M., Coulibaly, M., 1998. A sigma-coordinate primitive equation model for studying the circulation in the South Atlantic. Part I: Model configuration with error estimates. *Deep-Sea Research I* 45, 543-572.

Beckers, J.-M., Burchard, H., Deleersnijder, E., Mathieu, P.P., 2000. Numerical discretization of rotated diffusion operators in ocean models. *Monthly Weather Review* 128(8), 2711-2733.

Bernardello, R., Cardoso, J.G., Bahamon, N., Donis, D., Marinov, I., Cruzado, A., 2012. Factors controlling interannual variability of vertical organic matter export and phytoplankton

bloom dynamics: a numerical case-study for the NW Mediterranean Sea, *Biogeosciences* 9, 4233-4245, doi 10.5194/bg-9-4233-2012.

Blanke, B., Raynaud, S., 1997. Kinematics of the Pacific Equatorial Undercurrent: An Eulerian and Lagrangian Approach from GCM Results. *Journal of Physical Oceanography* 27, 1038-1053.

Bosc, E., Bricaud, A., Antoine, D., 2004. Seasonal and interannual variability in algal biomass and primary production in the Mediterranean Sea, as derived from 4 years of SeaWiFS observations, *Global Biogeochemical Cycle* 18, GB1005, doi 10.1029/2003GB002034.

Boyer, T., Levitus, S., Garcia, H., Locarnini, R.A., Stephens, C., Antonov, J., 2005: Objective analyses of annual, seasonal, and monthly temperature and salinity for the world ocean on a 0.25° grid. *International Journal of Climatology* 25, 931-945.

Boyer, D.L., Sommeria, J., Mitrovic, A.S., Chaitanya Pakala, V.K., Smirnov, S.A., Etling D., 2006.The Effects of boundary turbulence on Canyon Flows forced by periodic Along-Shelf currents. *Journal of Physical Oceanography* 36, 813-823.

Brasseur, P., Beckers, J.M., Brankart, J.M., Schoenauen, R., 1996. Seasonal temperature and salinity fields in the Mediterranean Sea: Climatological analyses of a historical data set. *Deep-Sea Research I* 43(2), 159-192.

Canals, M., Company, J.B., Martín, D., Sànchez-Vidal, A., Ramírez-Llodrà, E., 2013. Integrated study of Mediterranean deep canyons: Novel results and future challenges. *Progress in Oceanography* 118, 1-27.

Casella, E., 2009. Numerical simulation of mesoscale processes in the Ligurian Sea. Ph.D. Dissertation. Università degli Studi della Basilicata. Potenza, Italy.

Casella, E., Molcard, A., Provenzale, A., 2011. Mesoscale vortices in the Ligurian Sea and their effect on coastal upwelling processes. *Journal of Marine Systems* 88, 12-19.

Connolly, T.P., Hickey, B.M., 2014. Regional impact of submarine canyons during seasonal upwelling. *Journal Geophysical Research, Oceans*, 119, 953-975, doi 10.1002/2013JC009452.

Cruzado, A., Velasquez, Z.R., 1990. Nutrients and phytoplankton in the Gulf of Lions, northwestern Mediterranean. *Continental Shelf Research* 10 (9-11), 931-942.

da Silva, A.M., Young-Molling, C.C., Levitus, S., 1994. Atlas of Surface Marine Data 1994, Vol. 1: Algorithms and procedures. NOAA Atlas NESDIS 6. U.S. Gov. Printing Office, Wash., D.C., 83 pp.

Debreu, L., Marchesiello, P., Penven, P., Cambon, G., 2012. Two-way nesting in split-explicit ocean models: algorithms, implementation and validation. *Ocean Modelling* 49-50, 1-21.

De Leo, F.C., Smith, C.R., Rowden, A.A., Bowden, D.A., Clark, M.R., 2010. Submarine canyons: hotspots of benthic biomass and productivity in the deep sea. *Proceedings of the Royal Society B* 277, 2783-2792.

Dinniman, M.S., Klinck, J.M., Smith, Jr., W.O. Jr., 2003. Cross-shelf exchanges in a model of the Ross Sea circulation and biogeochemistry. *Deep-Sea Research II* 50, 3103-3120.

Durski, S.M., Glenn, S.M., Haidvogel, D.B., 2004. Vertical mixing schemes in the coastal ocean: Comparison of the level 2.5. Mellor-Yamada scheme with an enhanced version of the K profile parameterization. *Journal of Geophysical Research* 109, C01015, doi:10.1029/2002JC001702.

Echevin, V., Crépon, M., Mortier, L., 2003. Simulation and analysis of the mesoscale circulation in the northwestern Mediterranean Sea. *Annales Geophysicae* 21, 281-297.

Estournel, C., Auclair, F., Lux, M., Nguyen, C., Marsaleix, P., 2009. "Scale oriented" embedded Modeling of the North-Western Mediterranean in the frame of MFSTEP. *Ocean Science* 5, 73-90.

Fennel, K., 2010. The role of continental shelves in nitrogen and carbon cycling: Northwestern North Atlantic case study. *Ocean Science* 6, 539-548.

Flexas, M.M., Durrieu de Madron, X., Garcia, M.A., Canals, M., Arnau, P., 2002. Flow variability in the Gulf of Lions during the MATER HFF experiment (March-May 1997). *Journal of Marine Systems* 33-34, 197-214.

Flexas, M.M., van Heijst, G.J.F., Trieling, R.R., 2005. The Behaviour of Jet Currents over a Continental Slope Topography with a possible application to the Northern Current. *Journal of Physical Oceanography* 35, 790-810.

Flexas, M.M., Boyer, D.L., Espino, M., Puigdefàbregas, J., Rubio, A., Company, J.B., 2008. Circulation over a submarine canyon in the NW Mediterranean. *Journal of Geophysical Research* 113, C12002.

Font, J., Salat, J., Tintoré, J., 1988. Permanent features of the circulation in the Catalan Sea. *Oceanologica Acta* 9, 51-57.

Font J, Garcia-Ladona, E., Gorriz, E., 1995. The seasonality of mesoscale motion in the Northern Current of the western Mediterranean: several years of evidence. *Oceanologica Acta* 18, 207-219.

Freeland, H.J., Denman, K.L., 1982. A topographically controlled upwelling centre off southern Vancouver Island. *Journal of Marine Research*, 40, 1069-1093.

Garcia-Ladona, E., Castellon, A., Font, J., Tintoré, J., 1996. The Balearic current and volume transport in the Balearic basin. *Oceanologica Acta* 19, 489-497.

Gili, J.M., Pagès, F., Bouillon, J., Palanques, A., Puig, P., Heussner, S., Calafat, A., Canals, M., Monaco, A., 2000. A multidisciplinary approach to the understanding of hydromedusan populations inhabiting Mediterranean submarine canyons. *Deep-Sea Research I* 47, 1513-1533.

Granata, T.C., Estrada, M., Zika, U., Merry, C., 2004. Evidence for enhanced primary production resulting from relative vorticity induced upwelling in the Catalan Current. *Scientia Marina* 68(Suppl. 1), 113-119.

Griffies, S.M., Pacanowski, R.C., Hallberg, R.W., 1999. Spurious diapycnal mixing associated with advection in a z-coordinate ocean model. *Monthly Weather Review* 128, 538-564.

Grilli, F., Pinardi, N., 1998. The computation of Rossby radii of deformation for the Mediterranean Sea, MTP News 6, 4.

Haidvogel, D.B., Beckmann, A., 2000. Numerical Ocean Circulation Modeling. 2th ed., Imperial College Press, London, 320 p.

Halo, I., Penven, P., Backeberg, B., Ansorge, I., Shillington, F., Roman, R., 2014. Mesoscale eddy variability in the southern extension of the East Madagascar Current: seasonal cycle, energy conversion terms, and eddy mean properties. *Journal of Geophysical Research Oceans*, doi 10.1002/2014JC0009820.

Haney, R.L., 1991. On the pressure force over steep topography in sigma coordinate Ocean models. *Journal of Physical Oceanography* 21, 610-619.

Hedström, K.S., 2009. Technical manual for a coupled sea-ice/ocean circulation model, version 3. U.S. Department of the Interior Minerals Management Service, Anchorage, Alaska, 151 p.

Hickey, B.M., 1995. Coastal submarine canyons, paper presented at "Aha Huliko" A workshop of flow topography interactions, Office of Naval Research, Honolulu. 17-20 January.

Hickey, B.M., 1997. The response of a steep-sided, narrow canyon to time-variable wind forcing. *Journal of Physical Oceanography* 27, 667-726.

Holt, J.T., Allen, J.I., Proctor, R., Gilbert, F., 2005. Error quantification of a high-resolution coupled hydrodynamic-ecosystem coastal-ocean model: Part 1 model overview and assessment of the hydrodynamics. *Journal of Marine Systems* 57(1-2), 167-188. ISSN 0924-7963.

Jackett, D.R., McDougall, T.J., 1995. Minimal adjustment of Hydrographic profiles to achieve static stability. *Journal of Atmospheric and Oceanic Technology* 12, 381-389.

Johnson, J., Chapman, P., 2011. Deep Ocean Exchange with the Shelf (DOES). *Ocean Science* 7, 101-109.

Jordà, G., Flexas, M.M., Espino, M., Calafat, A., 2013. Deep flow variability in a deeply incised Mediterranean submarine valley (Blanes canyon). *Progress in Oceanography* 118, 47-60.

Jordi, A., Orfila, A., Basterretxea G., Tintoré, J., 2005. Shelf-slope exchanges by frontal variability in a steep submarine canyon. *Progress in Oceanography* 66, 120-141.

Jordi, A., Basterretxea G., Orfila, A., Tintoré, J., 2006. Analysis of the circulation and shelf-slope exchanges in the continental margin of the northwestern Mediterranean. *Ocean Science* 2, 173-181.

Jordi, A., Klinck, J.M., Basterretxea, G., Orfila, A., Tintoré, J., 2008. Estimation of shelf-slope exchanges induced by frontal instability near submarine canyons. *Journal of Geophysical Research* 113, C05016.

Kämpf, J., 2010. On preconditioning of coastal upwelling in the eastern Great Australian Bight. *Journal of Geophysical Research*, 115, C12071, doi 10.1029210C006294.

Klinck, J.M., 1996. Circulation near submarine canyons: a modeling study. *Journal of Geophysical Research* 101(C1), 1211-1223.

Large, W.G., McWilliams, J.C., Doney, S.C. 1994. Oceanic vertical mixing: a review and a model with a nonlocal boundary layer parameterization. *Reviews of Geophysics* 32, 363-403.

Lascaratos, A., Roether, W., Nittis, K., Klein, B., 1999. Recent changes in deep water formation and spreading in the eastern Mediterranean Sea: a review. *Progress in Oceanography* 44, 5-36.

La Violette, P.E., Tintoré, J., Font, J., 1990. The surface circulation of the Balearic Sea. *Journal of Geophysical Research* 95(C2), 1559-1568.

Lemarié, F., Debreu, L., Shchepetkin, A.F., McWilliams, J.C., 2012. On the stability and accuracy of the harmonic and biharmonic isoneutral mixing operators in ocean models. *Ocean Modelling* 52-53, 9-35.

Lopez-Fernandez, P., Calafat, A., Sanchez-Vidal, A., Canals, M., Flexas, M.M., Cateura, J., Company, J.B., 2013. Multiple drivers of particle fluxes in the Blanes submarine canyon and southern open slope: Results of a year round experiment. *Progress in Oceanography* 118, 95-107.

López-García, M.J., Millot, C., Font, J., García-Ladona, E., 1994. Surface circulation variability in the Balearic Basin. *Journal of Geophysical Research* 99, C2, 3285-3296.

Ly, L.N., L., Jiang, 1999. Horizontal pressure gradient errors of the Monterey Bay sigma coordinate ocean model with various grids. *Journal of Oceanography* 55, 87-97.

Marchesiello, P., McWilliams, J.C., Shchepetkin, A., 2001. Open boundary conditions for long-term integration of regional oceanic models. *Ocean Modelling* 3, 1-20.

Marchesiello, P., McWilliams, J.C., Shchepetkin, A., 2003. Equilibrium structure and dynamics of the California Current System. *Journal of Physical Oceanography* 33, 753-783.

Marchesiello, P., Debreu, L., Couvelard, 2009. Spurious diapycnal mixing in terrain-following coordinate models. *Ocean Modelling* 26, 156-169.

Masó, M., La Violette, P.E., Tintoré, J., 1990. Coastal flow modification by submarine canyons along the NE Spanish coast. *Scientia Marina* 54(4), 343-348.

Mason, E., Molemaker, J., Shchepetkin, A. F., Colas, F., McWilliams, J.C., Sangrà, P., 2010. Procedures for offline grid nesting in regional ocean models. *Ocean Modelling* 35, 1-15.

MEDOC Group, 1970. Observation of Formation of Deep Water in the Mediterranean Sea, 1969. *Nature* 227, 1037-1040.

Mellor, G.L., Ezer, T., Oey, L.Y., 1994. The pressure gradient conundrum of sigma coordinate ocean models. *Journal of Atmospheric and Oceanic Technology* 11, 1126-1134.

Millot, C., 1991. Mesoscale and seasonal variability of the circulation in the western Mediterranean. *Dynamics of Atmospheres and Oceans* 15, 179-214.

Millot, C., 1999. Circulation in the Western Mediterranean Sea. *Journal of Marine Systems* 20, 423-442.

Palanques, A., García-Ladona, E., Gomis, D., Martín J., Marcos, M., Pascual, A., Puig P., Gili, J.-M., Emelianov, M., Monserrat, S., Guillén, J., Tintoré, J., Segura, M., Jordi, A., Ruiz, S., Basterretxea, G., Font, J., Blasco, D., Pagès, F., 2005. General patterns of circulation, sediment fluxes and ecology of the Palamós (La Fonera) submarine canyon, northwestern Mediterranean. *Progress in Oceanography* 66, 80-119.

Penven, P., Echevin, V., Pasapera, J., Colas, F., Tam, J., 2005. Average circulation, seasonal cycle, and mesoscale dynamics of the Peru Current System: A modeling approach. *Journal of Geophysical Research* 110, C10021.

Penven, P., Debreu, L., Marchesiello, P., McWilliams, J.C., 2006. Evaluation and application of the ROMS 1-way embedding procedure to the central California upwelling system. *Ocean Modelling* 12, 157-187.

Penven, P., Marchesiello, P., Debreu, L., Lefevre J., 2008. Software tools for pre- and post-processing of oceanic regional simulations. *Environmental Modelling & Software* 23, 660-662.

Phillips, N.A., 1957. A coordinate system having some special advantages for numerical forecasting. *Journal of Meteorology* 14, 184-185.

Pinardi, N., Masetti, E., 2000. Variability of the large-scale general circulation of the Mediterranean Sea from observations and modeling: a review. *Palaeogeography, Palaeoclimatology, Palaeoecology* 158, 153-173.

Pinardi, N. Zavatarelli, M., Adani, M., Coppini, G., Fratianni, C., Oddo, P., Simoncelli, S., Tonani, M., Lyubartsev, V., Dobricic, S., Bonaduce, A., 2013. Mediterranean Sea large-scale low-frequency ocean variability and water mass formation rates from 1987 to 2007. *Progress in Oceanography*, http://dx.doi.org/10.1016/j.pocean.2013.11.003

Pullen, J.D., 2000. Modeling studies of the coastal circulation off northern California. Ph.D. Dissertation, Oregon State University.

Ramirez-Llodra, E., Baptista Company, J., Sardà, F., Rotllant, G., 2010. Megabenthic diversity patterns and community structure of the Blanes submarine canyon and adjacent slope in the Northwestern Mediterranean: a human overprint? *Marine Ecology* 31, 167-182.

Risien, C.M., Chelton, D.B. 2008. A global climatology of surface wind and wind stress fields eight years of QuikSCAT Scatterometer Data. *Journal of Physical Oceanography* 38, 2379-2413.

Rio, M.-H., Poulain, P.-M., Pascual, A., Mauri, E., Larnicol, G., Santoleri, R., 2007. A mean dynamic topography for the Mediterranean Sea computed from altimetric data, in-situ measurements and a general circulation model. *Journal of Marine Systems* 65, 484-508.

Rojas, P., García, M.A., Sospedra, J., Figa, J., Puigdefàbregas, J., López, O., Espino, M., Ortiz, V., Sanchez-Arcilla, A., Manríquez, M., Shirasago, B. 1995. On the structure of the mean flow in the Blanes Canyon area (NW Mediterranea) during summer. *Oceanological Acta* 18(4), 443-454.

Rubio, A., Barnier, B., Jordà, G., Espino, M., Marsaleix, P., 2009. Origin and dynamics of mesoscale eddies in the Catalan Sea (NW Mediterranean): Insight from a numerical model study. *Journal of Geophysical Research* 114, C06009.

Sabatés, A., Olivar, M.P., Salat, J., Palomera, I., Alemany, F., 2007. Physical and biological processes controlling the distribution of fish larvae in the NW Mediterranean. *Progress in Oceanography* 74, 355-376.

Salat, J., Garcia, M.A., Cruzado, A., Palanques, A., Arín L., Gomis, D., Guillén, J., de León A., Puigdefàbregas, J., Sospedra, J., Velásquez, Z.R., 2002. Seasonal changes of water mass structure and shelf slope exchanges at the Ebro shelf (NW Mediterranean). *Continental Shelf Research* 22, 327-348

Sammari, C., Millot, C., Prieur, L., 1995. Aspects of the seasonal and mesoscale variability of the Northern Current in the western Mediterranean Sea inferred from the PROLIG-2 and PROS-6 experiments. *Deep-Sea Research I* 42, 893-917.

Sanchez-Vidal, A., Canals, M., Calafat, A.M., Lastras, G., Pedrosa-Pàimes, R., Menéndez M., Medina, R., Company, J.B., Hereu, B., Romero, J., Alcoverro, T., 2012. Impacts on the Deep-Sea Ecosystem by a Severe Coastal Storm. *PLoSONE* 7(1):e30395, doi 10.1371/journal.pone.0030395.

Sardà, F., Company, J.B., Bahamon, N., Rotllant, G., Flexas, M.M., Sánchez, J.D., Zúñiga, D., Coenjaerts, J., Orellana, D., Jordà, G., Puigdefábregas, J., Sánchez-Vidal, A., Calafat, A., Martín, D., Espino, M., 2009. Relationship between environment and the occurrence of the deep-water rose shrimp *Aristeus antennatus* (Risso, 1816) in the Blanes submarine canyon (NW Mediterranean). *Progress in Oceanography* 82(4), 227-238.

Schaefer, A., Garreau, P., Molcard, A., Frunié, P., Seity, Y., 2011. Influence of high-resolution wind forcing on hydrodynamic modelling of the Gulf of Lions. *Ocean Dynamics* 61:1823-1844.

Schott, F., Visbeck, M., Send, U., Fischer, J., Stramma, L., Desaubies, Y., 1996. Observations of Deep Convection in the Gulf of Lions, Northern Mediterranean, during the winter of 1991/92. *Journal of Physical Oceanography* 26, 505-524.

Shchepetkin, A.F., McWilliams, J.C., 1998. Quasi-monotone advection schemes based on explicit locally adaptative dissipation. *Monthly Weather Review* 126, 1541-1580.

Shchepetkin, A.F., McWilliams, J.C., 2003. A method for computing horizontal pressure-gradient force in an oceanic model with a nonaligned vertical coordinate. *Journal of Geophysical Research* 108, C33090.

Shchepetkin, A.F., McWilliams, J.C., 2005. The regional oceanic modelling system (ROMS): a split-explicit, free-surface, topography-following-coordinate oceanic model. *Ocean Modelling* 9, 347-404.

She, J., Klinck, J.M., 2000. Flow near submarine canyons driven by constant winds. *Journal of Geophysical Research* 105(C12): 28671-28694.

Skliris, N., Goffart, A., Hecq, J.H., Djenidi, S., 2001. Shelf-slope exchanges associated with a steep submarine canyon off Calvi (Corsica, NW Mediterranean Sea): A modeling approach. *Journal of Geophysical Research* 106(C9), 18,883-19,901.

Skliris, N., Hecq, J.H., Djenidi, S., 2002. Water fluxes at an ocean margin in the presence of a submarine canyon. *Journal of Marine Systems* 32, 239-251.

Skliris, N., Djenidi, S., 2006. Plankton dynamics controlled by hydrodynamics processes near a submarine canyon off NW Corsican coast: A numerical modelling study. *Continental Shelf Research* 26, 1336-1358.

Smith, W.H.F., Sandwell, D.T., 1997. Global seafloor topography from satellite altimetry and ship depth soundings. *Science* 277, 1957-1962.

Song, Y., 1998. A general pressure gradient formulation for ocean models. Part I: scheme design and diagnostic analysis. *Monthly Weather Review* 126, 3213-3230.

Song, Y., Haidvogel, D., 1994. A semi-implicit ocean circulation model using a generalized topography-following coordinate system. *Journal of Computation Physics* 115, 228-244.

Song, Y.T., Wright, D.G., 1998. A general pressure gradient formulation for ocean models. Part II: energy, momentum, and bottom torque consistency. *Monthly Weather Review* 126, 3231-3247.

Taupier-Letage, I., Millot, C., 1986. General hydrodynamical features in the Ligurian Sea inferred from the DYOME experiment. *Oceanologica Acta* 9(2), 119-131.

Tintoré, J., Wang, D.P., La Violette, P.E., 1990. Eddies and thermohaline intrusions of the shelf/slope front off the northeast Spanish coast. *Journal of Geophysical Research* 95(C2), 1627-1633.

Vetter, E.W., Smith, C.R., De Leo, F.C., 2010. Hawaiian hotspots: enhanced megafaunal abundance and diversity in submarine canyons on the oceanic islands of Hawaii. *Marine Ecology* 31, 183-199.

Wang, D.P., Vieira, M.E.C., Salat, J., Tintoré, J., La Violette, P.E., 1988. A shelf/slope frontal filament off the northeast Spanish Coast. *Journal of Marine Research* 46, 321-332.

Zuñiga, D., Flexas, M.M., Sanchez-Vidal, A., Coenjaerts, J., Calafat, A., Jordà, G., García-Orellana, J., Puigdefàbregas, J., Canals, M., Espino, M., Sardà, F., Company, J.B., 2009 Particle fluxes dynamics in Blanes submarine canyon (Northwestern Mediterranean). *Progress in Oceanography* 82, 239-251.